Advanced Optimization and Machine Learning Techniques for Efficient Wireless Communication Networks

by © Esraa Aziz Mokhtar Muhammad Makled

A dissertation submitted to the School of Graduate Studies in partial fulfilment of the

requirements for the degree of

Doctor of Philosophy

Faculty of Engineering and Applied Science

Memorial University of Newfoundland

May 2024

St. John's   Newfoundland

Abstract

Wireless communications have become indispensable in modern society, driven by the proliferation of mobile devices, Internet-of-Things applications, and data-intensive services. As the world moves towards sixth-generation (6G) wireless networks, optimizing limited bandwidth and power resources is crucial to meet growing data demands. Additionally, harnessing the complete capabilities of all available wireless media, including space, air, and water, is deemed essential to ensure the seamless communications promised by the 6G wireless and beyond networks. This thesis focuses on overcoming data rate and security issues in two communication media, namely underwater and terrestrial.

Acoustic is the most prominent wireless communication technology in underwater communication. In underwater acoustic networks, full-duplex (FD) and non-orthogonal multiple access (NOMA) techniques are explored to address challenges unique to the underwater environment. The goal is to enhance the data rates, reliability, and security of underwater communication systems. Power optimization is studied to maximize the sum rate or secrecy sum rate against cyber attacks. The proposed algorithms provide enhanced sum rates and security when FD and NOMA are applied with effective interference cancellation.

In terrestrial communications, accurate cellular signal identification is essential for resource optimization and wireless network security. Hence, in this thesis, I provide multiple methodologies to enhance the ability to identify over-the-air signals from various technologies: global systems for mobile communications, universal mobile telecommunication systems, and long-term evolution in real-time. Morphological analysis and machine learning algorithms are proposed to achieve accurate signal

detection and identification to enhance the security and efficiency of wireless communication systems.

By tackling both media, this thesis aims to provide unique solutions to improve the security and data rates for future networks.

To the soul of my father,

To my supportive mother,

To my double rainbow child,

To my impeccable mentors,

I hope this work makes you all proud.

Acknowledgements

In the name of Allah, the Most Merciful and Gracious, I am humbled by the support that Allah, the Most Knowledgeable and Wise, granted me, enabling the completion of this journey.

I am profoundly grateful to Prof. Octavia Dobre for her steadfast mentorship and unwavering support during this challenging journey. Amidst academic hurdles, personal trials, and the global upheaval of the COVID-19 pandemic, Prof. Dobre provided invaluable guidance and encouragement, enabling me to persevere and bring this work to fruition. Her dedication to my academic and personal growth has been an enduring source of inspiration.

I extend my deepest appreciation to Dr. Amany Maklad, my mother, whose belief in my aspirations and tireless support sustained me through every obstacle. Despite the challenges posed by the pandemic and the transatlantic moves, her selfless dedication ensured that I could focus wholeheartedly on my studies. Her boundless love and support have been the cornerstone of my success, and words cannot adequately convey my gratitude.

Without the support of Prof. Dobre and my devoted mother, this work would never have come to fruition. Both have exemplified the ideals of strong, accomplished women who balance professionalism and compassion.

I am indebted to the Research Chair in Subsea Communications at Memorial University, Equinor, the Natural Sciences and Engineering Research Council of Canada, and Allen-Vanguard for their generous financial support, which played a pivotal role in making this work possible.

I am grateful to Dr. Ibrahim Al-Nahhal for his invaluable guidance and meticulous attention to

Co-Authorship Statement

I, Esraa A. Makled, hold a principal author status for all the manuscript chapters (Chapters 2-7) presented in this dissertation. However, each manuscript is co-authored by my supervisors and co-researchers, whose contributions have facilitated the development of this work as described below.

- Paper 1 in Chapter 2: E. A. Makled, A. Yadav, O. A. Dobre, and R. D. Haynes, "Hierarchical full-duplex underwater acoustic network: A NOMA approach," in Proc. IEEE OCEANS, Charleston, SC, USA, 2018, pp. 1–6.

  I was the primary author, with authors 2-4 contributing to the idea, its formulation and development, and the refinement of the presentation.

- Paper 2 in Chapter 3: E. A. Makled and O.A. Dobre, "On the security of full-duplex relay-assisted underwater acoustic network with NOMA," IEEE Transactions on Vehicular Technology, vol. 71, no 6., pp. 6255-6265, Mar. 2022.
  I was the primary author, with author 2 contributing to the idea, its formulation and development, and the refinement of the presentation.

- Paper 3 in Chapter 4: E. A. Makled, A. A. Al-Habob, O. A. Dobre, and O. Üreten, "Detection and identification of mobile network signals," IEEE Transactions on Instrumentation and Measurements, vol. 70, pp. 1–4, Sep. 2021.
  I was the primary author, with authors 2-4 contributing to the idea, its formulation and development, and the refinement of the presentation.

- Paper 4 in Chapter 5: E. A. Makled, I. Al-Nahhal, O. A. Dobre, and O. Üreten, "Identification of cellular signal measurements using machine learning," IEEE Transactions on Instrumentation and Measurement, vol. 72, pp. 1–4, Jan. 2023.

  I was the primary author, with authors 2-4 contributing to the idea, its formulation and development, and the refinement of the presentation.

- Paper 5 in Chapter 6: E. A. Makled, I. Al-Nahhal, O. A. Dobre, O. Üreten, and H. Shin, "Identification of cellular measurements: A neural network approach," IEEE Transactions on Instrumentation and Measurement, vol. 73, pp. 1-12, Oct. 2023.

  I was the primary author, with authors 2-5 contributing to the idea, its formulation and development, and the refinement of the presentation.

- Paper 6 in Chapter 7: E. A. Makled, I. Al-Nahhal, O. A. Dobre, O. Üreten, and H. Shin, "Identification of cellular signal measurements using extreme learning machine," under review, IEEE Transactions on Instrumentation and Measurement, Feb. 2024.

  I was the primary author, with authors 2-5 contributing to the idea, its formulation and development, and the refinement of the presentation.

Esraa Makled

Esraa Makled

Date

May 20th, 2024

Table of Contents

List of Tables

List of Figures

List of Abbreviations

5G	Fifth-Generation
6G	Sixth-Generation
ACD	Automatic Channel Detection
AI	Artificial Intelligence
ASI	Automatic Signal Identification
B	Full-Duplex Buoy
BS	Base Station
CI	Channel Information
CNN	Convolutional Neural Network
DCA	Data Collection Approach
DCNN	Deep Convolutional Neural Network
DL	Deep Learning (Chapters 4-7)
DL	Downlink (Chapters 2 and 3)
DNN	Deep Neural Network

ECM	Electronic Countermeasure
ELM	Extreme Learning Machine
FA	False Alarm
FC-FF	Fully Connected Feed-Forward
FD	Full-Duplex
FD-B	Full-Duplex Buoy
FD-R	Full-Duplex Relay
FFT	Fast Fourier Transform
GSM	Global System for Mobile Communications
HCFNN	Hybrid Convolutional Feedforward Neural Network
HD	Half-Duplex
IB-PSD	In-Band Power Spectral Density
IF	Intermediate Frequency
INN	Identification Neural Network
IoT	Internet-of-Things
LTE	Long Term Evolution
MB-PSD	Multiple Band Power Spectral Density
MI	Magneto-Inductive
ML	Machine Learning

NN	Neural Network
NOMA	Non-Orthogonal Multiple Access
NR-aided FD-NOMA	Non-Relay Aided Full-Duplex NOMA
NR-FD-NOMA	Non-Relay Aided Full-Duplex Non-Orthogonal Multiple Access
OMA	Orthogonal Multiple Access
PR	Precision-Recall
PSD	Power Spectral Density
QoE	Quality of Experience
R	Full-Duplex Relay
R-FD-NOMA	Relay Aided Full-Duplex NOMA
R-HD-OMA	Relay Aided Half-Duplex Orthogonal Multiple Access
R&S®	Rhode and Schwartz
RA	Robotic Actuators
RS	Resizing
RSI	Residual Self-Interference
RVFL	Random Vector Functional Link
S	Sensor
SI	Self-Interference
SIC	Self-Interference Cancellation

SINR	Signal-to-Interference-plus-Noise Ratio
SNR	Signal-to-Noise Ratio
SR	Sum Rate
SSR	Secrecy Sum Rate
SuIC	Successive Interference Cancellation
UAV	Unmanned aerial vehicles
UL	Uplink
UMTS	Universal Mobile Telecommunications Service
UWA	Underwater Acoustic
UWC	Underwater Wireless Communications
VR	Virtual Reality
ZP	Zero-padding

Chapter 1

Introduction

1.1 Background

In the ever-evolving technological milieu, heightened anticipation surrounds the forthcoming genera-
tion of wireless communication networks. This fervor reflects the profound advancements expected in
the realm of future networks. Envisioned as the heir to the fifth-generation (5G) of wireless commu-
nication networks, future networks hold the potential to inaugurate a paradigm shift in connectivity,
promising unparalleled speed, reliability, and capabilities [1]–[4].

Fig. 1.1, generated based on data from [5], illustrates a projection indicating a nearly twofold in-
crease in the number of connected devices, including fixed phones, mobile phones, PC devices, short-
range and wide-area Internet of Things (IoT) devices, by the year 2029. Consequently, the projected
annual growth rate of global mobile data traffic from the year 2020 to 2030 is expected to be 55%, cul-
minating in a monthly data volume of 5,016 exabytes by 2030 [6]. This anticipated surge in data traffic
necessitates a departure from the constraints of 5G, reaching its saturation point by 2030, compelling
an exploration of innovative paradigms to overcome obstacles encountered in earlier generations of
mobile networks. Such innovation and evolution are illustrated in [7] as shown in Fig. 1.2.

The anticipated augmentation in data rates is poised to support an array of novel applications and

services hitherto inconceivable. This transformative landscape encompasses facets such as holographic presence, immersive virtual reality (VR) experiences, real-time remote surgery, unmanned aerial vehicles (UAV), extended reality, space, and deep-sea tourism [4]. In addition, recent advancements in communication have introduced several novel concepts, such as edge intelligence, communication spanning sub-6GHz to Terahertz, non-orthogonal multiple access (NOMA), large intelligent surfaces, swarm networks, and self-sustaining networks [4], [8], [9]. These concepts are rapidly evolving into fully-fledged technologies poised to support the next generations of communication networks. However, the demands of these applications, such as ultra-high data rates, real-time access to potent computing resources, extremely low latency, precision localization and sensing, and exceptionally high reliability and availability, surpass the network capabilities promised by 5G [4], [10], [11].

Hence, 5G is anticipated to reach its saturation point by 2030, necessitating the exploration of innovative paradigms to address the obstacles encountered in earlier generations of mobile networks. The emergence of the sixth-generation (6G) mobile network is poised to establish elevated practical benchmarks, catering to the performance demands of the Internet of Everything, VR, 3D applications, artificial intelligence (AI), machine-to-machine communication, enhanced mobile broadband, and related technological advancements [2], [12]. To meet the escalating traffic demands, 6G is anticipated to provide 100-fold more spectrum compared to 5G [2], [12].

In the following sections of this chapter, the author expounds upon the fundamental framework of 6G, serving as the cornerstone for future wireless networks. Additionally, the chapter will delve into the challenges confronting 6G networks, elucidating how this thesis addresses some of these formidable issues.
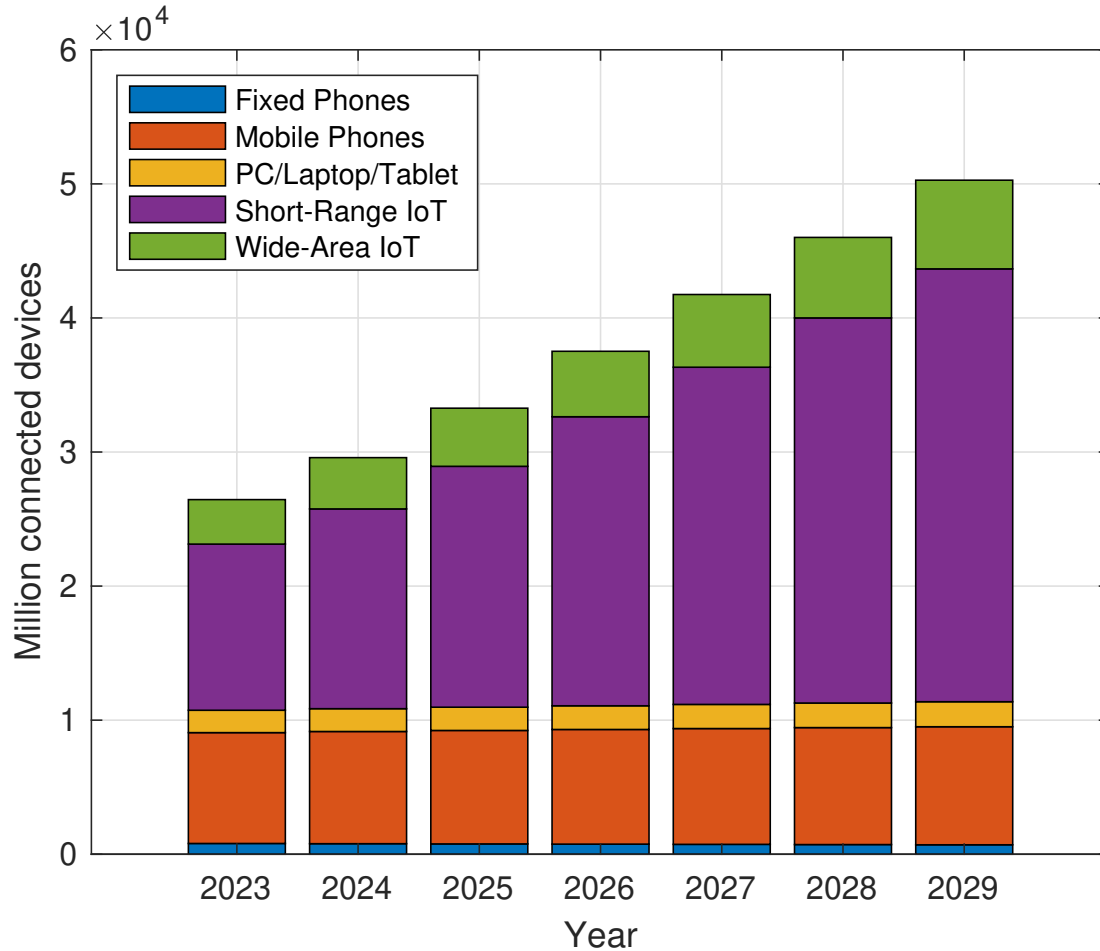
Figure 1.1: Forecast number of devices connected.

1.2 Future Wireless Networks

1.2.1 Features of Future Wireless Networks

The key features of future wireless networks encompass a spectrum of advancements poised to redefine the wireless communication landscape. Among these features is the pursuit of unprecedented speeds, with 6G targeting data rates far exceeding those of its predecessor, potentially reaching terabits per second. This significant leap in speed holds the promise of facilitating real-time applications, immersive experiences, and instantaneous connectivity. Complementing this speed is the defining characteristic of ultra-low latency, a crucial element for applications such as augmented reality, VR, and autonomous
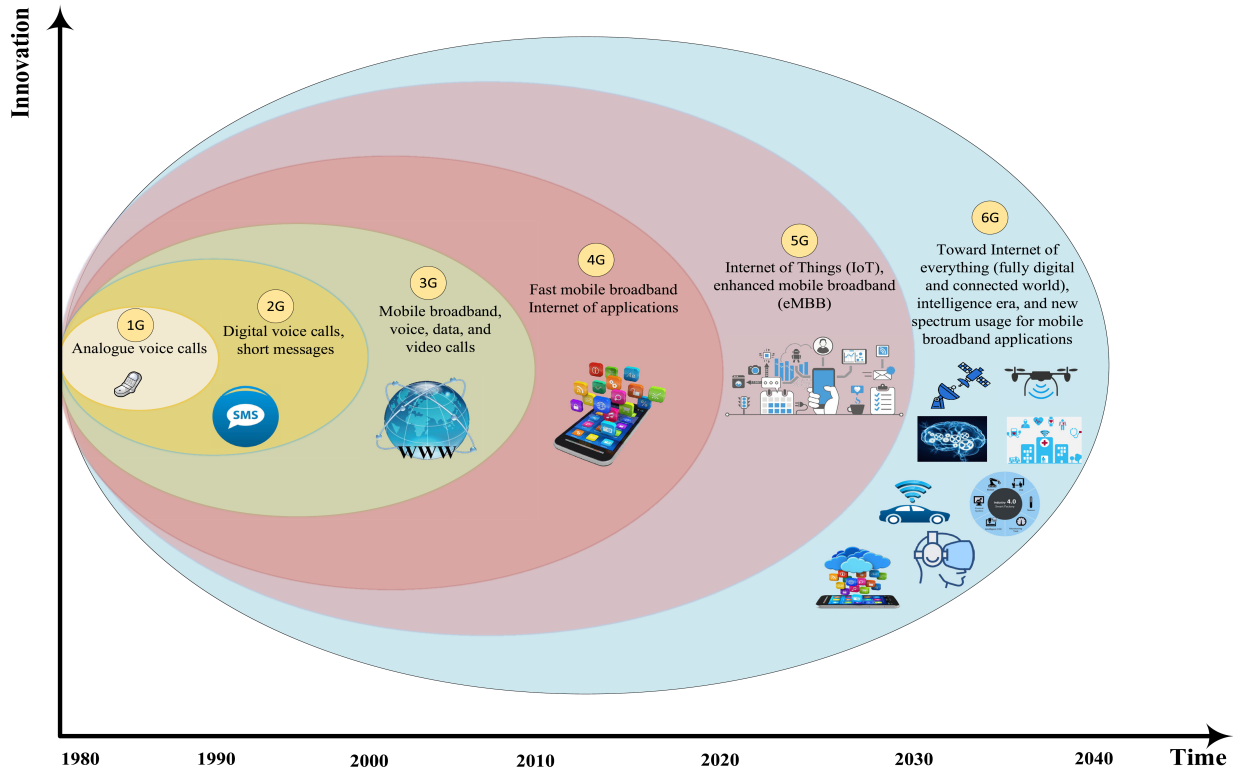
Figure 1.2: The evolution of mobile generation from 1G to 6G [7].

systems, where imperceptible communication delays are paramount. Another salient feature is the central role assigned to AI in future networks. From optimizing resource allocation to enabling intelligent network management, AI integration is positioned to enhance overall efficiency and responsiveness. Recognizing the environmental impact of network infrastructure, 6G places a premium on energy efficiency, with a commitment to implementing sustainable practices and technologies. Finally, the advent of 6G is expected to propel the development and deployment of autonomous systems, such as vehicles, drones, and robotics, by providing reliable and ultra-responsive connectivity. In concert, these key features herald a transformative era in wireless communication, underlining 6G's potential to reshape how people connect, communicate, and interact with technology. Furthermore, 6G envisions ubiquitous connectivity, aspiring to ensure seamless communication even in the most remote and challenging environments. This vision is set to materialize through a synergy of four main tiers: satellite communication, high-altitude platforms, advanced terrestrial networks, and underwater networks. Each tier will

4

present unique challenges and opportunities for optimizing resource utilization and ensuring secure communications.

1.2.2 Tiers of Future Wireless Networks
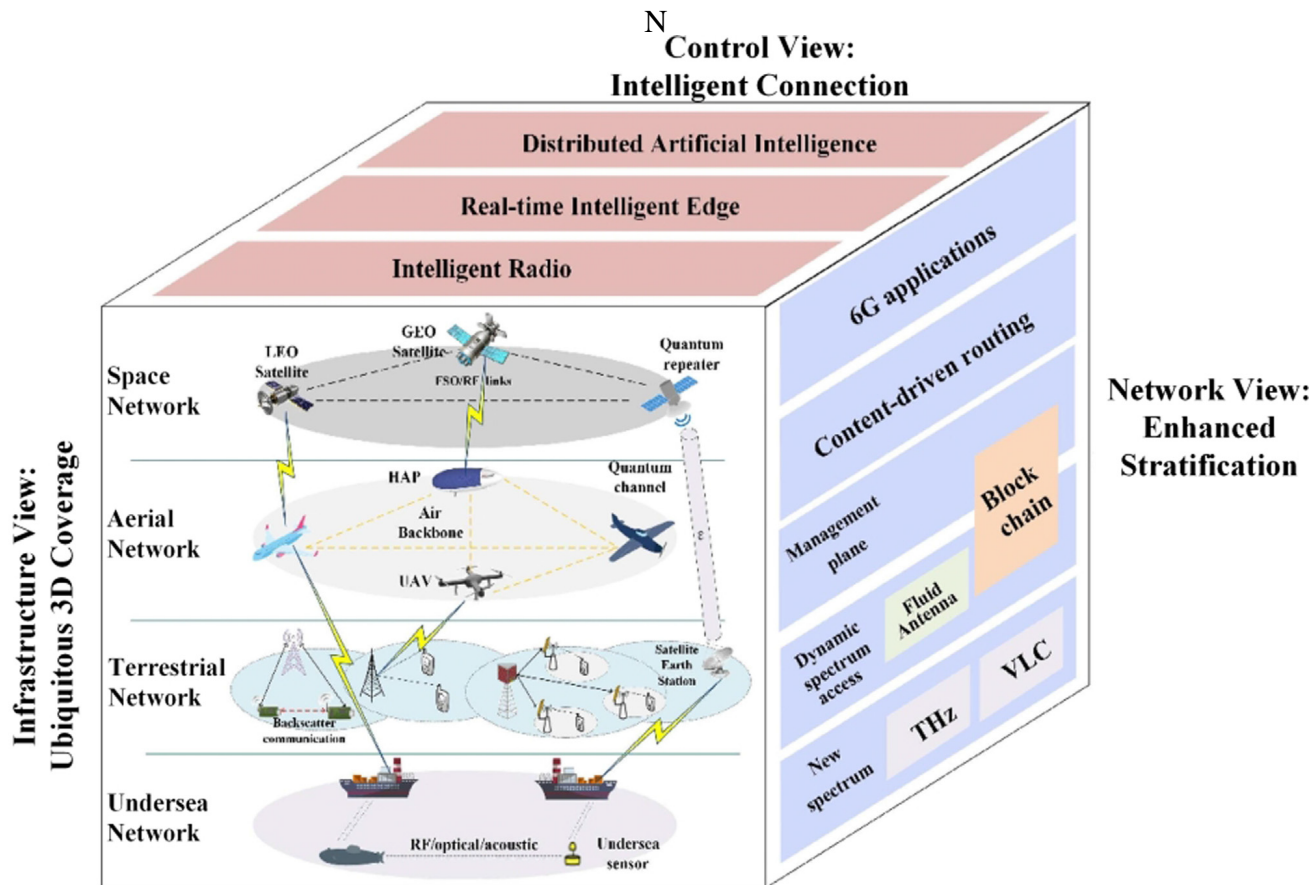
Figure 1.3: 6G wireless network tiers [2].

The existing terrestrial network infrastructure falls short of meeting the extensive coverage and pervasive connectivity demanded by the requirement of the omnipresence of 6G wireless networks. Consequently, there is a necessity for a comprehensive network encompassing both non-terrestrial and terrestrial elements to facilitate diverse applications like airborne travel, maritime navigation, and ground-based vehicles [13], [2]. In its structural design, 6G will manifest as a cell-free and four-tier large-dimensional network, partitioned into tiers for space, air, terrestrial, and underwater (or sea) net-

works. The structure is shown in Fig. 1.3. AI, intelligent radio, and edge computing are the tools used to control traffic over future networks.

Space-Network Tier

This tier will facilitate orbit or space Internet services, catering to applications such as space travel. It aims to provide wireless coverage by densely deploying low-Earth-orbit, medium-Earth-orbit, and geostationary-Earth-orbit satellites, especially in unserved and underserved areas not covered by terrestrial networks [13], [14]. For high-capacity satellite–ground transmission, satellites equipped with mm-wave communications will be deployed. Laser communications will be employed to achieve long-distance inter-satellite transmission in free space.

Air-Network Tier

This tier operates in the low-frequency, microwave, and mm-wave bands to offer more flexible and reliable connectivity. It addresses urgent events or remote mountain areas by densely deploying flying base stations (BS), including UAVs [14], and floating BSs like high-altitude platforms. The location features of floating BSs can facilitate the connection between space networks and reachable UAV BSs through the 6G-defined optical interface.

Terrestrial-Network Tier

This tier remains the primary solution for providing wireless coverage for most human activities. Besides, the THz band will be utilized to efficiently maximize the utilization of the current bands to meet the requirements for services with a Terabit per second (Tb/s) data rate, such as hologram and full-sense digital reality. Therefore, terrestrial networks, including low-frequency, microwave, mm-wave, and THz bands, will support the full band. Due to the high path loss associated with mm-wave and THz communications, more small BSs will be deployed, making 6G terrestrial networks an ultradense heterogeneous environment. This necessitates the deployment of ultrahigh-capacity x-haul. Optical fibre

will continue to play a crucial role for 6G, while THz wireless x-haul will be an attractive solution.

Underwater Tier
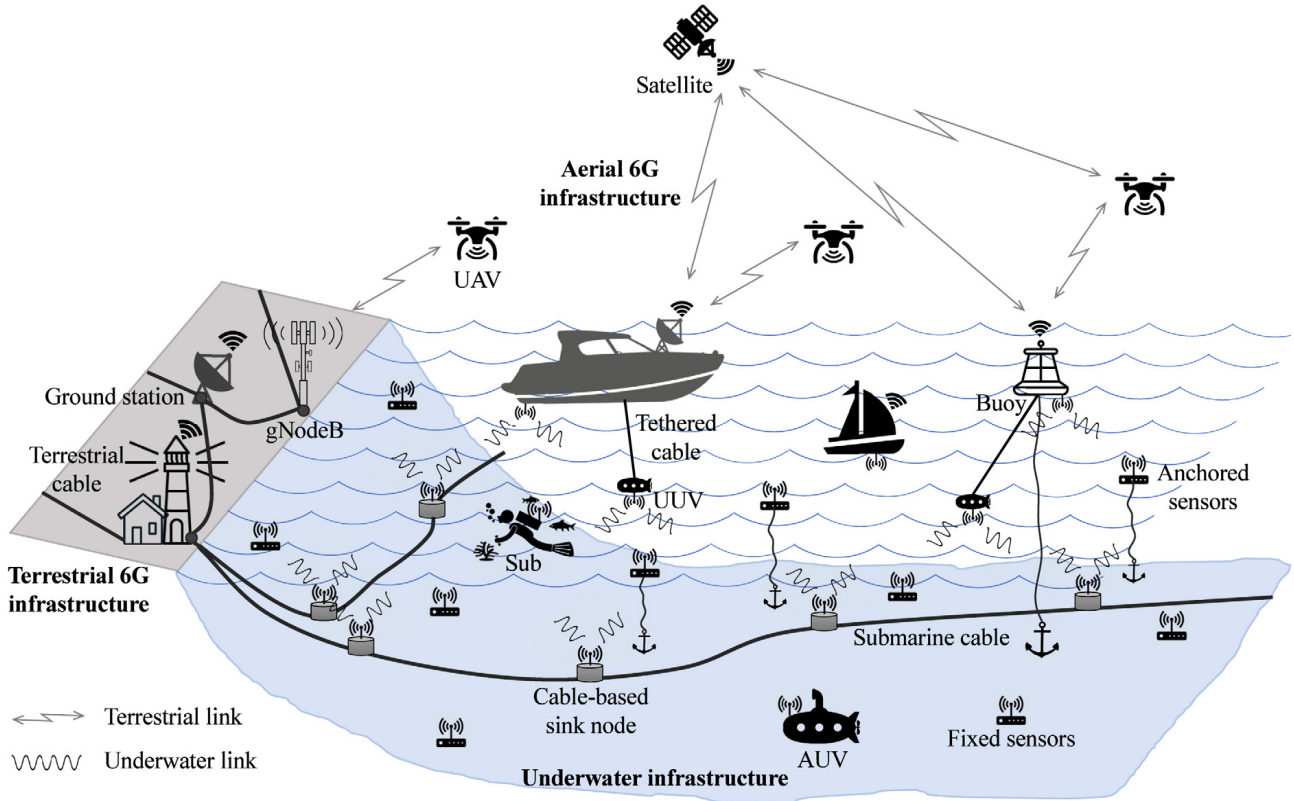
Figure 1.4: Underwater networks integrated within 6G networks [15].

This tier is designed to offer coverage and internet services for broad-sea and deep-sea activities, catering to both military and commercial applications [16], [17]. Due to the distinct propagation characteristics of water compared to land, acoustic and optical communications will be utilized to achieve high-speed data transmission for bi-directional underwater communications. Additionally, the deployment of more underwater hubs will be necessary to enhance the underwater network infrastructure. Underwater wireless communication (UWC) is one of the least studied frontiers of 6G, yet it holds immense potential for a wide range of applications, including oil and gas exploration, environmental monitoring, and defence.

There is a plethora of civil and military applications for UWC [16], [17]. The underwater IoT will enable the deployment of a vast network of underwater sensors and devices, enabling real-time monitoring of the marine environment. Underwater robotics is required for the development of more advanced and autonomous underwater robots capable of performing complex tasks such as inspection and maintenance. Besides, underwater exploration will require new underwater exploration tools, such as high-resolution underwater imaging and mapping systems [16], [17]. These applications require secure, fast, and high-bandwidth wireless communication technology underwater. Several types of underwater communications include acoustic, optical, radio frequency (RF), and magneto-inductive (MI) communications [18], [19]. The differences between these types of wireless underwater communication are summarized in Table 1.1 [18], [19].

The prominence of underwater acoustic communication as a primary choice among various methods stems from several key attributes. First and foremost, its efficiency in underwater environments is noteworthy, as sound waves travel adeptly through water, facilitating reliable communication over extended distances and through challenging underwater terrains. Additionally, acoustic signals exhibit lower attenuation rates in water compared to alternative communication methods, providing a foundation for robust and long-range communication. Notably, underwater acoustic communication systems are meticulously designed to operate within frequency ranges that minimize interference with marine life, underscoring their commitment to reducing potential impacts on aquatic ecosystems. Moreover, the proven reliability of acoustic communication is evident in its successful application across various underwater domains, including oceanographic research, environmental monitoring, and offshore industry operations. The compatibility of acoustic communication with underwater sensors further enhances its appeal, fostering seamless integration with existing underwater infrastructure. Finally, the adaptability of acoustic communication to different water conditions, encompassing variations in temperature and salinity levels, underscores its versatility and suitability for diverse underwater scenarios. In aggregate, these attributes position underwater acoustic communication as a standout choice, pivotal for the effective and sustainable advancement of underwater communication systems. However, several

Table 1.1: Advantages and disadvantages of different communication technologies.

Technology	Range	Data Rate	Latency	Power	Disadvantages	Advantages
Acoustic	~100km	kbps	667 ms/km	High	High latency, low bandwidth.	Long-range, maturity, and reliability, widely used.
Optical	~100m	Mbps	0.03 ms/km	Low	Line-of-sight, tight alignment.	High data rate, low latency, low energy consumption, direct cross-boundary communication.
RF/MI	~10m	Mbps	0.03 ms/km	Moderate	Large antenna, very short communication range.	Non-line-of-sight, direct cross-boundary communication.

challenges characterize underwater acoustic communication, each posing unique obstacles to the reliable transmission of signals. First, propagation loss is a formidable challenge, with underwater acoustic signals experiencing significant attenuation, particularly over long distances. The multipath effects further compound the complexities, introducing distortion and interference to the transmitted signals as they bounce off underwater surfaces. Additionally, the Doppler effect emerges as a concern, leading to frequency shifts in underwater acoustic signals and, consequently, complicating the demodulation process. Furthermore, the inherent noise in underwater acoustic channels adds another layer of difficulty, creating a scenario where distinguishing between desired signals and background noise becomes a formidable task. In navigating these challenges, advancements in underwater acoustic communication technologies are imperative to unlock the full potential of reliable and efficient communication beneath the water's surface.

Hence, exploring various advanced techniques to improve the spectral efficiency, reliability, and range of underwater acoustic (UWA) systems is essential for advancing future networks. However, this tier is one of the most under-researched tiers of future networks, especially regarding security and spectral efficiency [15].

1.2.3 Vision of Future Wireless Networks

Challenges of 6G Wireless Networks

Sustainability

The digital revolution is poised to be pivotal in transforming the economy and society to meet sustainable development goals [1], [2]. 6G should be an integral and critical component of this transformative journey. Notably, current 5G networks incorporate a design principle allowing sparse transmission of signals to conserve energy on the network side, potentially reducing carbon emissions from the information and communication technology industry. Nevertheless, achieving significant energy savings with wireless terminals under very sparse transmissions (e.g., on the order of 100 ms) remains a chal-
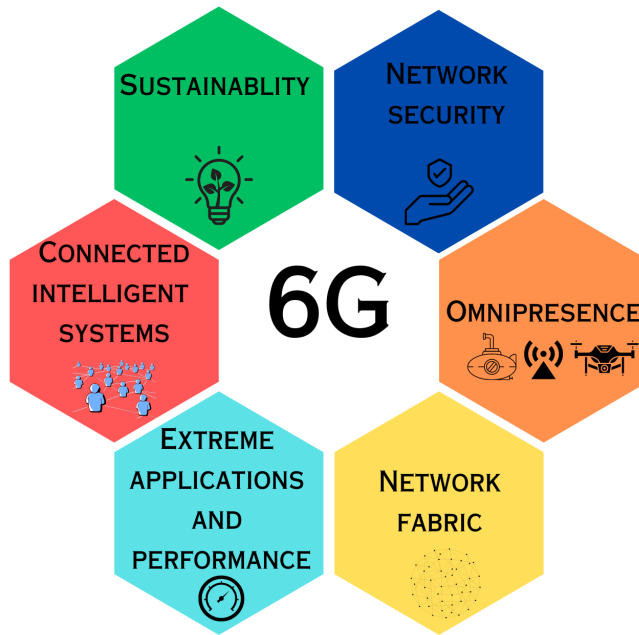
Figure 1.5: Challenges of 6G.

lenge requiring further study. Beyond reducing the carbon footprint of communication networks, 6G technologies should aspire to streamline other industry sectors and practices, significantly reducing carbon emissions. This transformational effect has the potential to yield a much higher positive impact on climate change than the climate footprint of the 6G network itself.

In addition to its positive climate impact, 6G aims to transform modern life by enhancing efficiency in agriculture, transportation, and environmental monitoring. It also seeks to enable reliable, inherently trustworthy, and high-capacity connectivity to support world-class education, transparent governance, and equitable and efficient law enforcement.

Security

While significant security advances have been achieved in 5G and are continually enhanced, future society is expected to impose increasing demands on wireless network security [1], [2]. Compliance with standards and regulations is crucial for the entire end-to-end communication chain. The operation of the wireless network should be highly predictable, with a robust level of resilience for the delivered

functionality. Personal security is of growing importance, and 6G should provide tools to protect end users. The wireless network must be capable of isolating and withstanding potential attacks, such as intrusion, tampering, and jamming, to establish wireless as a fully trustworthy solution.

Omnipresent Service Coverage

The move towards a fully digitalized world necessitates providing mobile services wherever needed. With 6G, the aim is to achieve coverage not only everywhere humans are, but also everywhere wireless devices are and can be. This includes coverage over land, sea, and air, encompassing large cells and focused capillary networks. Wireless services through 6G should be accessible to everyone and everything that can benefit from them. Achieving omnipresent 3D coverage involves connecting diverse links from land-based, air-based, and space-based nodes into one cohesive network.

Extreme Applications and Performance

As 5G technologies enable more use cases with better performance, 6G is expected to support novel applications beyond the capabilities of 5G. This includes supporting the future's vast information needs and full sensory communication, where extreme throughput is coupled with ultra-low latencies, extended range, and reduced power consumption. Novel use cases encompass extended reality applications, automated and remote control, distributed cognition, and their application in entertainment, e-health, industry, agriculture, transportation, governance, and law enforcement. Among the most challenging applications are fully immersive human-centric experiences, featuring perceived zero latency and non-limiting rates and mobility for enhanced interaction and natural meetings [1], [2].

Simultaneously, capacity needs are anticipated to increase, requiring more bandwidth, denser deployments, and increased spectral efficiency for 6G to accommodate higher traffic and bit rates, akin to the evolutionary trends seen in 5G and previous generations.

Connected Intelligent Systems

As machine learning (ML) tools and AI evolve, they are poised to become integral components of connected intelligent systems. Initially replacing heuristic, algorithmic, or brute force solutions to optimize specific localized tasks, these technologies are expected to mature and expand in their applications within integrated systems [1], [2]. Advancements in cognizant systems pave the way for real-time analysis and automated zero-touch operation and control. The 6G network is poised to serve as a fundamental cornerstone of such systems, relying on data streamed from wireless devices, particularly in applications that demand extreme bandwidth, such as real-time video monitoring, and low-latency requirements.

To fully harness these capabilities, the wireless network should also accommodate native AI agents, both centralized and distributed. These agents should be strategically placed and movable within the network based on specific requirements and needs. The wireless network must ensure the availability of timely data and analysis results where needed. Furthermore, mobile devices can play a role in performing additional ML and AI-related actions or predictions. The outcomes can be reported to assist network decisions, particularly in resource management aspects like mobility and multi-connectivity setup, making mobile devices an integral part of the infrastructure resource. 6G will be critical in addressing the evolving communication needs of distributed AI systems or agents operating in society, especially in applications like smart cities and intelligent traffic systems.

Network Fabric

The diverse use cases and applications anticipated in 6G present widely varying requirements, ranging from extreme throughput and imperceptible interruptions related to mobility handling to reliably ultra-low latencies and extreme battery longevity with cost-effective deployments and operations. Consequently, the network architecture must be flexible enough to support various deployments of network components and processing instances, tailored to the specific needs of each use case and leveraging its particular circumstances.

As part of adapting to different use cases, deploying applications at the network edge and new network-application interactions are expected to be crucial. This adaptation aims to enable optimized performance concerning quality of experience (QoE), particularly regarding latency and bandwidth requirements.

Technical Objectives of 6G Wireless Networks

To realize the potential frontiers of communications, 6G networks have to provide extended network capabilities beyond 5G networks. The key performance indicators for evaluating 6G wireless networks encompass spectrum and energy efficiencies, peak data rate, user-experienced data rate, area traffic capacity (or space traffic capacity), connectivity density, latency, and mobility [20]. The detailed technical objectives are presented in Fig. 1.6 and include the following:

- A peak data rate of at least 1 Tb/s, which is 100 times that of 5G. For specific scenarios, such as THz wireless backhaul and fronthaul (x-haul), the peak data rate is expected to reach up to 10 Tb/s [21].

- A user-experienced data rate of 1 Gb/s, which is 10 times that of 5G. It is also expected to provide a user-experienced data rate of up to 10 Gb/s for some scenarios, such as indoor hotspots [21].

- An over-the-air latency of 10–100 μs and high mobility ($\geq$ 1,000 km/h). This will ensure acceptable QoE for scenarios like hyper-high-speed rail and airline systems [13].

- Ten times the connectivity density of 5G, reaching up to 10^7 devices/km^2 and an area traffic capacity of up to 1 Gb/s/m^2 for scenarios like hotspots [13].

- An energy efficiency of 10–100 times and a spectrum efficiency of 5–10 times those of 5G [13].

Figure 1.6: Technical objectives of 6G vs. 5G and 4G wireless networks [4].

1.3 Thesis Motivation

Two major challenges facing future wireless networks are spectrum allocation and security. Also, as future networks are expected to be more sophisticated, energy consumption tends to increase, while at the same time, they need to be environmentally friendly. Hence, energy optimization is a crucial challenge. Also, future wireless networks are expected to be omnipresent. This thesis improves the resource utilization efficiency and security of the first two tiers of 6G communications: underwater and terrestrial communications. Underwater wireless communication is one of the least studied frontiers, and with the vast oceans and water bodies and the number of operations underwater for civil and military applications, including oil and gas, submarine communication, sea bed monitoring, and others, underwater wireless communications is expected to be handling more data in 6G networks. Hence, it is essential to ramp up research on this tier so it will not act as a bottleneck for the rest of the future of 6G

network. New technologies need to be explored for the challenging underwater environment, e.g., the application of the intelligent, reflective surface technology is studied in [22]. In this thesis, two of the major emerging technologies are applied, full-duplex (FD) and NOMA, to optimize spectral efficiency with respect to power utilization and enhance system security. Specifically, this part of the thesis will focus on:

- Developing and implementing advanced techniques, FD and NOMA, to improve underwater communication systems' spectral efficiency and power utilization.

- Improving spectral efficiency and security of two of the four tiers of future networks, namely underwater and terrestrial, utilizing advanced wireless communications techniques.

The other frontier is the terrestrial tier. Terrestrial is the most utilized wireless communication form, which is essential to attempt to improve its security and spectrum efficiency. As for terrestrial communication, the primary scarcity lies in the spectrum domain. Spectrum allocation and management constitute pivotal aspects of managing and securing terrestrial communication. Automatic signal identification (ASI) is instrumental in spectrum allocation and management. ASI is also indispensable for ensuring communication security. Consequently, the latter part of this research introduces innovative approaches, leveraging feature-based likelihood and ML techniques to proficiently identify cellular signals from power spectral density (PSD) readings. Specifically, this part of the thesis will focus on:

- Utilizing a feature-based approach to detect the noise floor of a PSD, the presence of signals, and identify the types of the detected signals.

- Improving spectral efficiency and security of two of the four tiers of future networks, namely underwater and terrestrial, utilizing advanced wireless communications techniques.

This multifaceted approach aims to address spectrum scarcity challenges while concurrently fortifying communication systems' security aspects.

1.4   Thesis Organization

In this thesis, innovative methodologies are employed to enhance the efficiency of utilizing limited resources and to fortify the security of future networks. Chapters 2 and 3 focus on UWC. Specifically, in Chapter 2, a system that applies FD and NOMA is proposed to improve the system sum rate of UWA communications. Chapter 3 evaluates the security robustness of the devised system, particularly in safeguarding against potential eavesdropping threats. In terrestrial communications, new technologies are employed to apply ASI to identify several cellular signals from PSD real measurements. Chapter 4 proposes a feature-based likelihood methodology to detect the noise floor of a PSD measurement and identify the number and types of signals on the measurement. Chapter 5 proposes a ML algorithm that uses a feedforward neural network to determine whether a signal belongs to a certain cellular technology. Chapter 6 proposes a ML algorithm that uses a convolutional neural network to identify a cellular signal type. Chapter 7 improves the identification accuracy of cellular signal types using an extreme learning machine (ELM) model. Finally, Chapter 8 concludes this work and provides future work directions.

1.5   Thesis Contribution

1. FD and NOMA are applied on UWA communications systems, and a convex optimization algorithm that efficiently allocates power to maximize the sum rate of the network is proposed. The outcomes of this investigation enhance both the spectral and power efficiency of the UWA network [23].

2. The resilience of the aforementioned algorithm against potential eavesdropper attacks is studied, considering scenarios with known and unknown eavesdropper locations. In this study, effective power allocation strategies are used to maximize the secrecy sum rate, thereby bolstering the security of the UWA communication network [24].

17

3. Morphological techniques are used to detect and identify cellular signals, contributing to the development of reliable and accurate identification methods in wireless communication networks [25].

4. ML techniques are applied to identify whether the measured signal belongs to a specific cellular technology, enhancing the precision and efficiency of identifying individual cellular signals [26].

5. ML techniques are utilized in cellular signal identification to identify the cellular technology of signal measurement, enabling the simultaneous identification of multiple types of cellular signals [27].

6. Innovative ML approaches are explored, ELM in particular, to classify cellular signals, simplify the training process, and improve identification accuracy [28].

References

[1] G. Wikström, J. Peisa, P. Rugeland, N. Johansson, S. Parkvall, M. Girnyk, G. Mildh, and I. L. Da Silva, "Challenges and technologies for 6G," in *Proc. 2nd 6G Wireless Summit (6G SUMMIT)*, 2020, pp. 1–5.

[2] M. Banafaa, I. Shayea, J. Din, M. H. Azmi, A. Alashbi, Y. I. Daradkeh, and A. Alhammadi, "6G mobile communication technology: Requirements, targets, applications, challenges, advantages, and opportunities," *Alexandria Engineering Journal*, vol. 64, pp. 245–274, Feb. 2023.

[3] K. David, J. Elmirghani, H. Haas, and X.-H. You, "Defining 6G: Challenges and opportunities [from the guest editors]," *IEEE Veh. Technol. Magazine*, vol. 14, no. 3, pp. 14–16, Aug. 2019.

[4] C. De Alwis, A. Kalla, Q.-V. Pham, P. Kumar, K. Dev, W.-J. Hwang, and M. Liyanage, "Survey on 6G frontiers: Trends, applications, requirements, technologies and future research," *IEEE Open J. of the Communs. Society*, vol. 2, pp. 836–886, Apr. 2021.

[5] Ericsson AB. Traffic exploration tool. Interactive online tool. Available at: http://www.ericsson.com/TET/trafficView/loadBasicEditor.ericsson.

[6] F. Tariq, M. R. Khandaker, K.-K. Wong, M. A. Imran, M. Bennis, and M. Debbah, "A speculative study on 6G," *IEEE Wireless Communs.*, vol. 27, no. 4, pp. 118–125, Aug. 2020.

[7] M. Alsabah, M. A. Naser, B. M. Mahmmod, S. H. Abdulhussain, M. R. Eissa, A. Al-Baidhani, N. K. Noordin, S. M. Sait, K. A. Al-Utaibi, and F. Hashim, "6G wireless communications networks: A comprehensive survey," *IEEE Access*, vol. 9, pp. 148 191–148 243, Nov. 2021.

[8] W. Saad, M. Bennis, and M. Chen, "A vision of 6G wireless systems: Applications, trends, technologies, and open research problems," *IEEE Netw.*, vol. 34, no. 3, pp. 134–142, Oct. 2019.

[9] F. Fang, Y. Xu, Q.-V. Pham, and Z. Ding, "Energy-efficient design of irs-noma networks," *IEEE Trans. on Veh. Technol.*, vol. 69, no. 11, pp. 14 088–14 092, Sep. 2020.

[10] Y. Lu and X. Zheng, "6G: A survey on technologies, scenarios, challenges, and the related issues," *Journal of Industrial Information Integration*, vol. 19, p. 100158, Feb. 2020.

[11] Y. Liu, X. Yuan, Z. Xiong, J. Kang, X. Wang, and D. Niyato, "Federated learning for 6G communications: Challenges, methods, and future directions," *China Communications*, vol. 17, no. 9, pp. 105–118, Sep. 2020.

[12] P. Yang, Y. Xiao, M. Xiao, and S. Li, "6G wireless communications: Vision and potential techniques," *IEEE Netw.*, vol. 33, no. 4, pp. 70–75, Jul. 2019.

[13] Z. Zhang, Y. Xiao, Z. Ma, M. Xiao, Z. Ding, X. Lei, G. K. Karagiannidis, and P. Fan, "6G wireless networks: Vision, requirements, architecture, and key technologies," *IEEE Veh. Technol. magazine*, vol. 14, no. 3, pp. 28–41, Sep. 2019.

[14] J. Liu, Y. Shi, Z. M. Fadlullah, and N. Kato, "Space-air-ground integrated network: A survey," *IEEE Communs. Surveys Tuts.*, vol. 20, no. 4, pp. 2714–2741, May 2018.

[15] N.-N. Dao, N. H. Tu, T. T. Thanh, V. N. Q. Bao, W. Na, and S. Cho, "Neglected infrastructures for 6G—underwater communications: How mature are they?" *Journal of Network and Computer Applications*, vol. 213, p. 103595, Apr. 2023.

[16] A. Gkikopouli, G. Nikolakopoulos, and S. Manesis, "A survey on underwater wireless sensor networks and applications," in *Proc. Mediterranean Conference on Control Automation*, Barcelona, Spain, 2012, pp. 1147–1154.

[17] C. Gussen, M. Campos, W. A. Martins, F. M. Costa, and J. N. Gois, "A survey of underwater wireless communication technologies," *J. Commun. Inf. Sys*, vol. 31, no. 1, pp. 242–255, Oct. 2016.

[18] M. Jouhari, K. Ibrahimi, H. Tembine, and J. Ben-Othman, "Underwater wireless sensor networks: A survey on enabling technologies, localization protocols, and internet of underwater things," *IEEE Access*, vol. 7, pp. 96 879–96 899, Jul. 2019.

[19] H. Luo, J. Wang, F. Bu, R. Ruby, K. Wu, and Z. Guo, "Recent progress of air/water cross-boundary communications for underwater sensor networks: A review," *IEEE Sensors J.*, vol. 22, no. 9, pp. 8360–8382, Mar. 2022.

[20] M. Series, "IMT vision–framework and overall objectives of the future development of IMT for 2020 and beyond," *Recommendation ITU*, vol. 2083, no. 0, Sep. 2015.

[21] A.-A. A. Boulogeorgos, A. Alexiou, T. Merkle, C. Schubert, R. Elschner, A. Katsiotis, P. Stavrianos, D. Kritharidis, P.-K. Chartsias, J. Kokkoniemi *et al.*, "Terahertz technologies to deliver optical network quality of experience in wireless systems beyond 5G," *IEEE Communs. Magazine*, vol. 56, no. 6, pp. 144–151, Jun. 2018.

[22] S. Kisseleff, S. Chatzinotas, and B. Ottersten, "Reconfigurable intelligent surfaces in challenging environments: Underwater, underground, industrial and disaster," *IEEE Access*, vol. 9, pp. 150 214–150 233, Nov. 2021.

[23] E. A. Makled, A. Yadav, O. A. Dobre, and R. D. Haynes, "Hierarchical full-duplex underwater acoustic network: A NOMA approach," in *Proc. IEEE OCEANS*, Charleston, SC, USA, 2018, pp. 1–6.

[24] E. A. Makled and O. A. Dobre, "On the security of full-duplex relay-assisted underwater acoustic network with NOMA," *IEEE Trans. on Veh. Technol.*, vol. 71, no. 6, pp. 6255–6265, Mar. 2022.

[25] E. A. Makled, A. A. Al-Habob, O. A. Dobre, and O. Üreten, "Detection and identification of mobile network signals," *IEEE Trans. Instrum. Meas.*, vol. 70, pp. 1–4, Sep. 2021.

[26] E. A. Makled, I. Al-Nahhal, O. A. Dobre, and O. Üreten, "Identification of cellular signal mea-surements using machine learning," *IEEE Trans. Insturm. Meas.*, vol. 72, pp. 1–4, Jan. 2023.

[27] E. A. Makled, I. Al-Nahhal, O. A. Dobre, O. Üreten, and H. Shin, "Identification of cellular measurements: A neural network approach," *IEEE Trans. Instrum. Meas.*, vol. 73, pp. 1–12, Oct. 2023.

[28] ——, "Identification of cellular signal measurements using extreme learning machine," *under review, IEEE Trans. Instrum. Meas.*, pp. 1–10, Feb. 2024.

Chapter 2

Hierarchical Full-Duplex Underwater Acoustic Network: A NOMA Approach

2.1 Abstract

The prevalent technology in underwater wireless is underwater acoustic communications. The sum rate in underwater acoustic channels is limited by the underwater environment properties. In this chapter, the author attempts to increase the sum rate of underwater channels without utilizing additional resources through adding a relay and employing full-duplex (FD) and non-orthogonal multiple access (NOMA) technologies. The adopted system model has two sensors and two robotic arms communicating with a buoy via a relay. Employing FD-NOMA allows multiple uplink and downlink transmissions to occur simultaneously, using the same time and frequency resources. The main challenge for this deployment is the interference between the transmissions. Interference cancellation techniques, successive interference cancellation, and self-interference cancellation are employed to mitigate the interference due to NOMA and FD, respectively. In order to maximize the sum rate, an optimization problem over the power is formulated and solved as a convex optimization problem. The performance of the system is benchmarked against the performance of non-relay (NR) aided FD-NOMA and relay-aided (R) half-duplex orthogonal multiple access (HD-NOMA). It is shown that R-FD-NOMA always has a higher

23

sum rate than NR-FD-NOMA, irrespective of the efficiency of interference cancellation. In addition, it is shown that at efficient interference cancellation, the sum rate of FD-NOMA is higher than HD-OMA.

2.2 Introduction

Oceanic applications, such as oil and gas exploration and pipeline monitoring, rely on underwater wireless communications [1]–[3]. The most common examples of underwater wireless communication technologies are acoustic, optical wireless and radio frequency communication. Long-range wireless communications is dominated by underwater acoustic (UWA) transmission [2]. UWA communication is challenging due to the complex underwater environment, where signals suffer from multiple reflections, severe dispersions and variations. Besides, the UWA channel is characterized by long propagation delay due to the slow acoustic wave speed [1]. These characteristics limit the sum rate of UWA channels.

In addition, underwater devices are power-limited. Hence, relays are used to increase power utilization efficiency, channel reliability and transmission distance. Incorporating relays supports communication systems by amplifying and forwarding, or decoding and forwarding the data, among other strategies [4]–[6].

Furthermore, technologies such as full-duplex (FD) and non-orthogonal multiple access (NOMA) are indispensable for enhancing the sum rate without additional radio resources. FD communications enhance the channel rate by allowing for simultaneous transmission and reception of signals on the same frequency. Owing to the self-interference (SI) caused by the FD operation, the rate enhancement is possible only if the SI is cancelled up to the noise level. Theoretically, FD can double the throughput of the system when compared to the conventional half-duplex [7]. On the other hand, NOMA allows the multiplexing of multiple users at the same time and frequency resource, and hence, improves the rate [8]. NOMA differentiates between users by assigning different power levels (power-domain NOMA) or different codes (code-domain NOMA). The power level assignment depends on the channel strength.

NOMA was shown to provide better spectral efficiency than orthogonal multiple access (OMA) systems in wireless communications [8].

Previously, FD and NOMA have been investigated independently in UWA communications [9], [10]. In this chapter, FD and NOMA are integrated with a relay-based UWA network with the goal of improving the network sum rate and reliability. The integration of FD and NOMA is not straightforward, especially in underwater channels and with the additional interference in uplink (UL) and downlink (DL) channels due to SI and interference from NOMA. A sum rate maximization problem is formulated for UWA channels under interference and transmission power constraints. The problem is solved by optimizing the transmission powers to provide the highest sum rate.

The rest of this chapter is organized as follows: Section 2.3 describes the system model, Section 2.4 formulates the sum rate maximization problem, and Section 2.5 presents the solution for the problem. The results are shown in Section 2.6, and Section 2.7 concludes the chapter.

2.3   System Model

Consider a hierarchical UWA communication system consisting of an FD-buoy (B), an FD-relay (R), two sensors (S_1 and S_2) and two robotic actuators (RA_1 and RA_2), as depicted in Fig. 2.1. The sensors send data to the buoy on the UL channel, while the buoy sends data to the two RAs on the DL channels. Both UL and DL channels use the relay node, which decodes-and-forwards the received data to the buoy and RAs, respectively.

The channels B→R, S_1→R and S_2→R form the UL-NOMA group, whereas R→B, R→RA_1 and R→RA_2 form the DL-NOMA group. In NOMA, the receiver performs successive interference cancellation (SuIC) on strong interfering signals in order to guarantee accurate signal detection. The SuIC efficiency is represented by $\theta \in [0, 1]$, where $\theta = 0$ denotes perfect SuIC.

The relay and buoy employ SI cancellation (SIC) techniques and are left with residual SI (RSI),
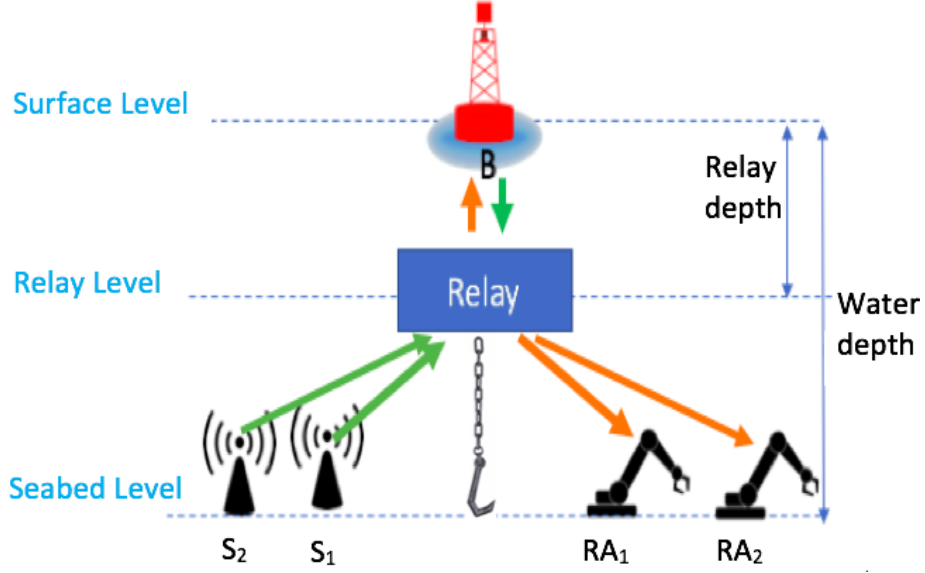
Figure 2.1: System model.

which is represented by I_A as:

$$I_A = \frac{p_A^{(1-\lambda)}}{\beta \mu^\lambda},$$

(2.1)

where $A \in \{R, B\}$, p_A denotes the transmission power of the relay or buoy, β is the interference suppression factor due to passive cancellation technique, and μ and λ are SIC cancellation factors [7], [11]. In order to study the impact of imperfect SIC on the system performance, λ is varied between 0 and 1 as per [11], where $\lambda = 0$ and 1 correspond to no and perfect SIC, respectively.

The UWA channel is usually characterized by slow propagation and the distinct reflections of the signal from the sea bottom and surface. Consequently, signals have different delays at the receiver. For the UWA channel gain, G, there is no standard statistical channel model available. The chosen model for this chapter includes large- and small-scale fading in [12], as

$$G = \mathbb{E}\left\{ \frac{1}{W} \int\limits_{f_0}^{f_0+W} |\bar{H}_0(f) \sum_\ell h_\ell \tilde{\gamma}_\ell(f,t) e^{-2\pi f_\ell \tau_\ell}|^2 df \right\},$$

(2.2)

where $\bar{H}_0$ represents the channel filtering effect, and h_ℓ and τ_ℓ are large-scale parameters on the ℓth path. The small-scale fading effect on the channel is represented by $\gamma_\ell(f,t)e^{2\pi a_\ell f t}$. γ_ℓ is the small-scale fading coefficient, while a_ℓ is the Doppler scaling factor on the ℓth path. W is the bandwidth and f_0 is

the minimum frequency of the channel.

Next, for each channel, the signal-to-interference-plus-noise ratios (SINRs) for the channels $S_1 \rightarrow R$, $S_2 \rightarrow R$, $B \rightarrow R$, $R \rightarrow RA_1$, $R \rightarrow RA_2$ and $R \rightarrow B$, are respectively defined as:

$$\gamma_1(\mathbf{p}) = \frac{p_{S_1} G_{S_1,R}}{p_{S_2} G_{S_2,R} + \theta p_B G_{B,R} + I_R + \sigma_N^2} \tag{2.3}$$

$$\gamma_2(\mathbf{p}) = \frac{p_{S_2} G_{S_2,R}}{\theta p_{S_1} G_{S_1,R} + \theta p_B G_{B,R} + I_R + \sigma_N^2}, \tag{2.4}$$

$$\gamma_3(\mathbf{p}) = \frac{p_B G_{B,R}}{p_{S_1} G_{S_1,R} + p_{S_2} G_{S_2,R} + I_R + \sigma_N^2}, \tag{2.5}$$

$$\gamma_4(\mathbf{p}) = \frac{p_{R_1} G_{R,RA_1}}{G_{R,RA_1} \sum\limits_{j=2,3} p_{R_j} \omega_j + \sum\limits_{k=1,2,B} p_{S_k} G_{S_k,RA_1} + \sigma_N^2}, \tag{2.6}$$

$$\gamma_5(\mathbf{p}) = \frac{p_{R_2} G_{R,RA_2}}{G_{R,RA_2} \sum\limits_{j=1,3} p_{R_j} + \sum\limits_{k=1,2,B} p_{S_k} G_{S_k,RA_2} + \sigma_N^2}, \tag{2.7}$$

$$\gamma_6(\mathbf{p}) = \frac{p_{R_3} G_{R,B}}{\theta G_{R,B} \sum\limits_{j=1,2} p_{R_j} + p_{S_2} G_{S_2,B} + p_{S_1} G_{S_1,B} + I_B + \sigma_N^2}, \tag{2.8}$$

where $G_{x,y}$ is the average channel gain on $x \rightarrow y$. p_{S_1}, p_{S_2} and p_B are the transmission powers of S_1, S_2, and B, respectively. p_{R_1}, p_{R_2}, and p_{R_3} are the transmission powers from R to RA_1, RA_2, and B, respectively. The vector $\mathbf{p}$ collects p_{S_1}, p_{S_2}, p_B, p_{R_1}, p_{R_2} and p_{R_3}. I_B and I_R are the RSIs at B and R, respectively. Distances are chosen so that UL channel gains are sorted as $G_{B,R} > G_{S_1,R} > G_{S_2,R}$, and the DL channel gains are sorted as $G_{R,B} > G_{R,RA_1} > G_{R,RA_2}$. ω_2 is equal to θ, while ω_3 is equal to 1.

The ambient noise power, σ_N^2, has four components: turbulence noise, shipping noise, wave noise, and thermal noise. The following empirical formulas give the individual power spectral densities (PSDs) of these noise components in dB re μ Pa per Hz as a function of frequency f in kHz [13]:

$$N_t(f) \quad = 17 - 30 \log f,$$

$$N_s(f) \quad = 40 + 20 \, (s - 0.5) + 26 \log f - 60 \log(f + 0.03),$$

$$N_w(f) \quad = 50 + 7.5 w^{1/2} + 20 \log f - 40 \log(f + 0.4),$$

$$N_{th}(f) \quad = -15 + 20 \log f. \tag{2.9}$$

The level of shipping activity is represented by $s \in [0,1]$. w denotes the wind speed in m/s. The overall acoustic PSD is calculated as [13]:

$$N_a(f) = 10^{N_t(f)/10} + 10^{N_s(f)/10} + 10^{N_w(f)/10} + 10^{N_{th}((f)/10}. \tag{2.10}$$

In order to convert the PSD from the acoustic to the electrical domain (W/Hz), the following formula is used [4]:

$$N(f) = \frac{10^{-17.2} N_a(f)}{\phi}, \tag{2.11}$$

where $N(f)$ is the equivalent electrical noise PSD and ϕ denotes the efficiency of the electric circuit in converting the acoustic power to electrical power.

2.4 Sum Rate Optimization

In this section, the sum rate maximization problem is formulated using equations (2.3)-(2.8), where the relationship between the rate (C) and the SINR (γ) of a channel is expressed as $C = \log_2(1+\gamma)$ in bps/Hz. The goal is to obtain the optimal transmit powers of the sensors, buoy, and relay nodes. The optimization problem is thus expressed as:

$$\max_{\mathbf{p}} \quad \sum_{i=1}^{6} \log_2(1 + \gamma_i(\mathbf{p})) \tag{2.12a}$$

$$\text{s.t.} \quad C_{\min} \le C_{\mathrm{S_1,R}}, C_{\min} \le C_{\mathrm{S_2,R}},$$

$$C_{\min} \le C_{\mathrm{RA_1,R}}, C_{\min} \le C_{\mathrm{RA_2,R}}, \tag{2.12b}$$

$$C_{\mathrm{RA_1,R}} + C_{\mathrm{RA_2,R}} \le C_{\mathrm{B,R}}, \tag{2.12c}$$

$$C_{\mathrm{S_1,R}} + C_{\mathrm{S_2,R}} \le C_{\mathrm{R,B}}, \tag{2.12d}$$

$$p_{\mathrm{R_1}} + p_{\mathrm{R_2}} + p_{\mathrm{R_3}} \le \bar{p}_{\mathrm{R}}, \tag{2.12e}$$

$$0 \le p_{\mathrm{S_1}} \le \bar{p}_{\mathrm{S_1}}, 0 \le p_{\mathrm{S_2}} \le \bar{p}_{\mathrm{S_2}}, 0 \le p_{\mathrm{B}} \le \bar{p}_{\mathrm{B}}, 0 \le p_{\mathrm{R_1}}, 0 \le p_{\mathrm{R_2}}, 0 \le p_{\mathrm{R_3}}, \tag{2.12f}$$

where $\bar{p}_{\mathrm{S_1}}$, $\bar{p}_{\mathrm{S_2}}$, $\bar{p}_{\mathrm{B}}$, and $\bar{p}_{\mathrm{R}}$ denote the maximum transmit powers of $\mathrm{S_1}$, $\mathrm{S_2}$, B, and R, respectively. $C_{\mathrm{x,y}}$ represents the rate of channel x→y. The constraints in (2.12b) guarantee that every channel gets a minimum rate of $C_{\min}$. Constraints (2.12c) and (2.12d) limit the sum rates of DL channels, $C_{\mathrm{R,RA_1}}$ and $C_{\mathrm{R,RA_2}}$, and the sum rates of UL channels $C_{\mathrm{S_1,R}}$ and $C_{\mathrm{S_2,R}}$ to the achievable capacities of channels, $C_{\mathrm{R,B}}$ and $C_{\mathrm{B,R}}$, respectively. Furthermore, constraints (2.12e) and (2.12f) limit the transmission power of the nodes.

2.5 Proposed Solution

It can be observed that (2.12) is non-convex in nature due to the non-convexity involved in the objective function (2.12a) and the constraints (2.12c) and (2.12d).

Equations (2.12a), (2.12c), and (2.12d) are non-convex because $\gamma_i(\mathbf{p})$ is a quotient of two functions in $\mathbf{p}$. Since the division does not conserve linearity, $\gamma_i(\mathbf{p})$ is not linear. As a result, $\log_2(1+\gamma_i(\mathbf{p}))$ is neither concave nor convex and solving this problem optimally is computationally challenging especially for UWA devices. To solve (2.12) more efficiently, (2.12) is transformed for tractability, approximates the resulting problem by a convex problem, and then proposes a rapidly converging iterative algorithm.

To transform the problem into an equivalent problem, two new slack variables are introduced x_i and z_i such that:

$$\gamma_i(\mathbf{p}) \triangleq \frac{g_i(\mathbf{p})}{h_i(\mathbf{p})} \geq x_i \, \forall i, \tag{2.13}$$

$$x_i z_i \leq g_i(\mathbf{p}) \, \forall i. \tag{2.14}$$

$$h_i(\mathbf{p}) \leq z_i \, \forall i, \tag{2.15}$$

After applying the transformation, (2.12) can be equivalently rewritten as:

$$\max_{\mathbf{p}, z_i, x_i} \quad \sum_{i=1}^{6} \log_2(1 + x_i) \tag{2.16a}$$

$$\text{s.t.} \quad x_i z_i \leq g_i(\mathbf{p}) \, \forall i, \tag{2.16b}$$

$$h_i(\mathbf{p}) \leq z_i \, \forall i, \tag{2.16c}$$

$$(2.12b) - (2.12f). \tag{2.16d}$$

The equivalence between (2.12) and (2.16) can be verified by the fact that the newly introduced constraints are active at optimality. It can be observed that (2.16) is still not convex because of constraints, (2.16b) and (2.16c), which are non-convex.

The constraint in equation (2.16b) is neither convex nor concave because it involves the multiplication of two variables, $x_i z_i$. The inequality in (2.16c) is not convex for all i. As observed, $h_i(\mathbf{p})$ in (2.3)-(2.5) and (2.8), have concave interference terms. Given that $h_i(\mathbf{p})$ is on the left hand side (lesser side) of the inequality, whenever $h_i(\mathbf{p})$ has interference terms, the constraint in (2.16c) is not convex. In the following, these constraints are approximated to become convex.

For constraint (2.16b), the upper bound approximation is used as in [14] as follows:

$$f(x_i, z_i) = x_i z_i \leq F(x_i, z_i, \xi_i) \triangleq \frac{1}{2\xi_i} x_i^2 + \frac{\xi_i}{2} z_i^2 \, \forall \xi_i > 0. \tag{2.17}$$

For $\hat{\xi}_i = x_i/z_i$, it can be easily observed that, $f(x_i, z_i) = \mathrm{F}(x_i, z_i, \hat{\xi}_i)$ and $\nabla f(x_i, z_i) = \nabla \mathrm{F}(x_i, z_i, \hat{\xi}_i)$, where ∇f denotes the gradient operator.

While, for constraint (2.16c) $p^{(1-\lambda)}$ is approximated, for $0 \le \lambda \le 1$, with a first-order Taylor series at $p(n)$ as follows [15]:

$$
\begin{aligned}
I_{\mathrm{R_L}}(n+1) &= \frac{(p_{\mathrm{R}}(n))^{(1-\lambda)}}{\beta\mu^\lambda} + (1-\lambda)\frac{(p_{\mathrm{R}}(n))^{(-\lambda)}}{\beta\mu^\lambda} \times (p_{\mathrm{R}} - p_{\mathrm{R}}(n)), \\
I_{\mathrm{B_L}}(n+1) &= \frac{(p_B(n))^{(1-\lambda)}}{\beta\mu^\lambda} + (1-\lambda)\frac{(p_{\mathrm{B}}(n))^{(-\lambda)}}{\beta\mu^\lambda} \times (p_{\mathrm{B}} - p_{\mathrm{B}}(n)),
\end{aligned}
\tag{2.18}
$$

where n is the iteration index for Algorithm 1 and $p_{\mathrm{R}}(n) = \sum_{j=1}^{3} p_{\mathrm{R}_j}(n)$.

Applying the above approximations, problem (2.12) can be solved by iteratively solving the convex problem (2.19), which is formulated for the nth iteration index as:

$$
\max_{\mathbf{p}, z_i, x_i} \quad \sum_{i=1}^{6} \log_2(1 + x_i) \tag{2.19a}
$$

$$
\text{s.t.} \quad p_{\mathrm{S}_2} G_{\mathrm{S}_2,\mathrm{R}} + \theta p_{\mathrm{B}} G_{\mathrm{B},\mathrm{R}} + I_{\mathrm{R_L}}(n) + \sigma_N^2 - z_1 \le 0, \tag{2.19b}
$$

$$
\theta p_{\mathrm{S}_1} G_{\mathrm{S}_1,\mathrm{R}} + \theta p_{\mathrm{B}} G_{\mathrm{B},\mathrm{R}} + I_{\mathrm{R_L}}(n) + \sigma_N^2 - z_2 \le 0, \tag{2.19c}
$$

$$
p_{\mathrm{S}_1} G_{\mathrm{S}_1,\mathrm{R}} + p_{\mathrm{S}_2} G_{\mathrm{S}_2,\mathrm{R}} + I_{\mathrm{R_L}}(n) + \sigma_N^2 - z_3 \le 0, \tag{2.19d}
$$

$$
\theta G_{\mathrm{R},\mathrm{B}} \sum_{j=1,2} p_{\mathrm{R}_j} + \sum_{k=1,2} p_{\mathrm{S}_k} G_{\mathrm{S}_k,\mathrm{B}} + I_{\mathrm{B}_L}(n) + \sigma_N^2 - z_6 \le 0, \tag{2.19e}
$$

$$
h_q(\mathbf{p}) - z_q \le 0 \quad \forall q = [4,5], \tag{2.19f}
$$

$$
\frac{1}{2\hat{\xi}_i(n)} x_i^2 + \frac{\hat{\xi}_i(n)}{2} z_i^2 - g_i(\mathbf{p}) \le 0 \,\forall i, \tag{2.19g}
$$

$$
(2.12b) - (2.12f). \tag{2.19h}
$$

Problem (2.19) needs to be solved iteratively and the pseudocode for the proposed sum rate optimization algorithm is summarized in Algorithm 1. C_{tot} is the total sum rate on all channels. G is a set that consists of all the channel gains, $G_{\mathrm{B},\mathrm{R}}$, $G_{\mathrm{S}_1,\mathrm{R}}$, $G_{\mathrm{S}_2,\mathrm{R}}$, $G_{\mathrm{R},\mathrm{B}}$, $G_{\mathrm{R},\mathrm{RA}_1}$, $G_{\mathrm{R},\mathrm{RA}_2}$. The problem at the

---

Algorithm 1 Iterative Sum Rate Maximization Algorithm

Input $\bar{p}_{S_1}$, $\bar{p}_{S_2}$, $\bar{p}_B$, $\bar{p}_R$, G, λ, θ, σ^2, $C_{\min}$, and tolerance (ϵ),

Output p and C_{tot},

Set $n := 0$ and initialize $\mathbf{p}(n)$, $z_i(n)$, $x_i(n)$, and $\hat{\xi}_i(n)$ by $\frac{x_i(n)}{z_i(n)}$,

1: **Repeat:**

2: Solve (19) for $\mathbf{p}^*$, z_i^*, x_i^* $\forall i$;

3: Set $n := n + 1$;

4: Update $x_i(n)$ by x_i^*, $z_i(n)$ by z_i^* and $\hat{\xi}_i(n)$ by $\frac{x_i^*}{z_i^*}\forall i$;

5: **Until** convergence of sum rate with tolerance ϵ.

---

nth iteration is convex and the optimal solution of this iteration is a feasible input point to the problem

at the $(n + 1)$th iteration. It can be shown that the algorithm generates non-decreasing objective func-

tion values at each iteration. Since the problem is bounded from above by the power constraints, the

algorithm converges to some local optimal solution.

2.6   Results and Discussion

In this section, the performance of the system is studied as obtained by using Algorithm 1. The opti-

mization problem is solved centrally at the buoy, which is assumed to have perfect knowledge of the

channel gains. $\bar{p}_{S_1}$ and $\bar{p}_{S_2}$ are set to 0 dBW, while $\bar{p}_B$ and $\bar{p}_R$ are set to 4.8 dBW [16], [17]. f_0 is 10 kHz

and W is 5.5 kHz [12]. β and μ are 38 dB and 18 dB, respectively [7], [11]. The noise is calculated

based on moderate wind speed of 10 m/s, a maximum shipping activity factor of 1 and perfect circuit

efficiency of 1 [13], [18]. The minimum sum rate for each channel ($C_{\min}$) is 2 kbps. The tolerance, ϵ, is

set to 10^{-4}. The algorithm is implemented using CVX with SDPT3 as the internal solver [19], [20].

Fig. 2.2 colour blueshows the convergence behaviour of Algorithm 1. For $\lambda = 0.8$ and $\theta = 0.1$,
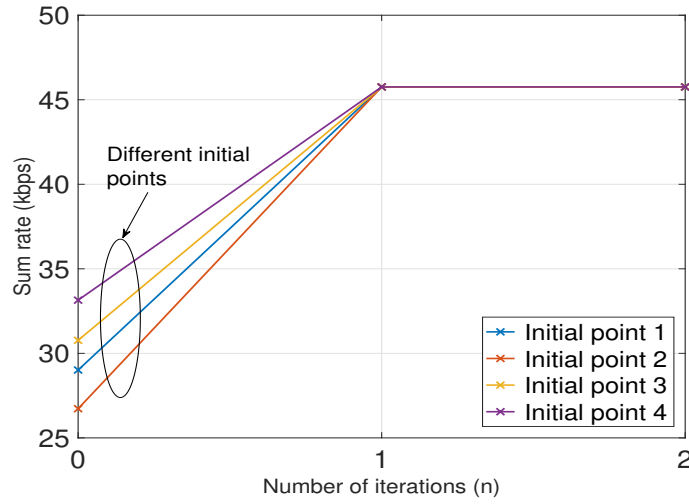
Figure 2.2: The number of iterations to converge for SIC efficiency $(\lambda) = 0.8$ at SuIC efficiency $(\theta) = 0.1$.
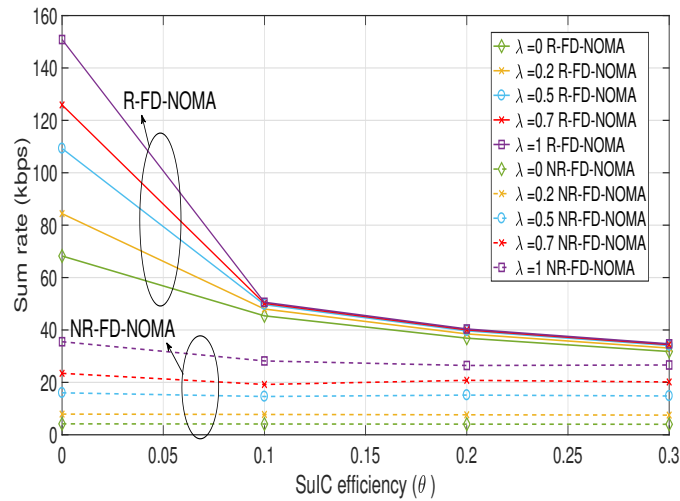
Figure 2.3: Sum rate vs. SuIC efficiency (θ) at different SIC efficiencies.

the algorithm was run for four different initial values. It can be observed that for all four initial values the algorithm converges within two iterations.

In order to benchmark the effect of adding the relay and employing FD and NOMA, the performance of relay-aided (R) FD-NOMA, non-relay (NR) aided FD-NOMA and relay-aided half-duplex orthogonal multiple access (R-HD-OMA) are compared. In NR-FD-NOMA, it is assumed that there is no relay and hence, the communication is direct between the buoy and the robotic arms or the sensors. The minimum guaranteed sum rate per channel is reduced to 0.8 kbps, due to the weak channels between the buoy and the seabed. The maximum power levels are kept the same. The other benchmark model is R-HD-OMA. In R-HD-OMA, it is assumed that each communication channel has a dedicated bandwidth. In addition, the bandwidth is divided equally among all concurrent transmissions. Only UL or DL communications can take place during one time slot. Consequently, for the UL and DL communications to take place, two time slots are needed. Each transmission utilizes different time or frequency resources and hence, there is no interference. The absence of interference between different transmissions means that the SIC and SuIC efficiencies will have no effect on the power or the sum rate of the system. The same constraints from (2.12) are applied to the transmission. For a fair comparison, the sum rate of two time slots will be considered. The channel conditions are assumed to be the same in both time slots. The results are depicted in Figs. 2.3-2.7.

Fig. 2.3 shows that as the efficiency of SuIC increases, represented as a decrease in θ, the sum rate increases. As the SuIC efficiency increases, the interference from other transmissions due to NOMA decreases, and consequently, the sum rate increases. It is assumed that if $\theta > 0.3$, the SuIC efficiency is not acceptable. Similarly, Fig. 2.3 shows that as the efficiency of SIC increases, represented as an increase in λ, the sum rate increases. This shows that as the isolation between the DL and UL signals increases, interference decreases, and hence, the sum rate increases. The maximum sum rate is achieved at $\lambda = 1$ and $\theta = 0$, where the minimal interference occurs.

Fig. 2.3 also compares R-FD-NOMA and the NR-FD-NOMA. R-FD-NOMA always supports a higher sum rate when compared to NR-FD-NOMA, irrespective of the SuIC and SIC efficiencies. It is

shown that R-FD-NOMA can (at $\theta = 0$ and $\lambda = 0.2$) octuple the sum rate of the system when compared to the NR-FD-NOMA.

Figs. 2.4-2.7 compare R-FD-NOMA with R-HD-OMA as per the total power consumed (shown on the right-hand side y-axis) and the sum rate (shown on the left hand side y-axis). Total power refers to the sum of the power required by all devices. Note that the letter "R" is omitted in the figures for simplicity.

In R-HD-OMA, the absence of interference between different transmissions means that the SIC and SuIC efficiencies will have no effect on the power or the sum rate of the system. This is shown in Figs. 2.4 and 2.5, where the sum rate for R-HD-OMA system is constant at 190 kbps and the total power consumed by all nodes is constant at 6 W for all θ and λ. For a single time slot in R-FD-NOMA, all UL and DL transmissions are performed consuming the full bandwidth.

As seen from Fig. 2.4, the SuIC has to be efficient for R-FD-NOMA to provide a higher sum rate than R-HD-OMA. The sum rate at a good SuIC can provide up to 30% increase in rate of R-FD-NOMA when compared to sum rate of R-HD-OMA. Also, the figure shows that as the efficiency increases (θ decreases) more capacity could be achieved and hence more power is needed. Fig. 2.5 shows that at θ =0, if the SIC efficiency (λ) is greater than 0.4, the sum rate of R-FD-NOMA is greater than can the sum rate of R-HD-OMA.

In order to further understand the behavior of the total power in Figs. 2.4 and 2.5, individual node powers are studied in Fig. 2.6. Given that the effect of the interference on each transmission is different, the transmission power on each channel is altered individually to cater for the highest possible total sum rate. In addition, the buoy has the highest possible power of all nodes. Thus, a sharp increase in p_B leads to an overall increase in the total power. In Fig. 2.5a, it is shown that the power increases once λ takes a non-zero value. Then, the power decreases slowly afterwards. From Fig. 2.6a, it can be seen that the main reason for the spike was an increase in the p_B. This increase is based on the nature of the RSI model in (3.1). At $\lambda = 0$, the SI is at its maximum as nearly no SIC mechanism is applied, and the term for RSI in (3.1) is reduced to $p\beta$. Hence, the effect of the power on the RSI increased. Once λ takes
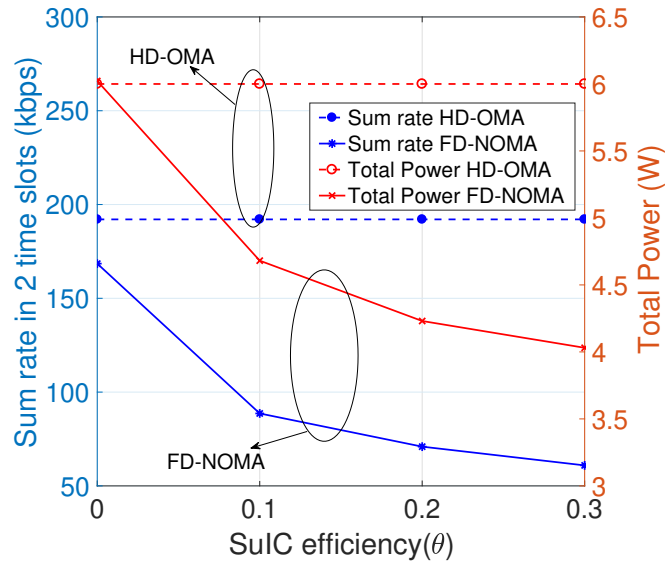
(a) SIC efficiency(λ) = 0.3.
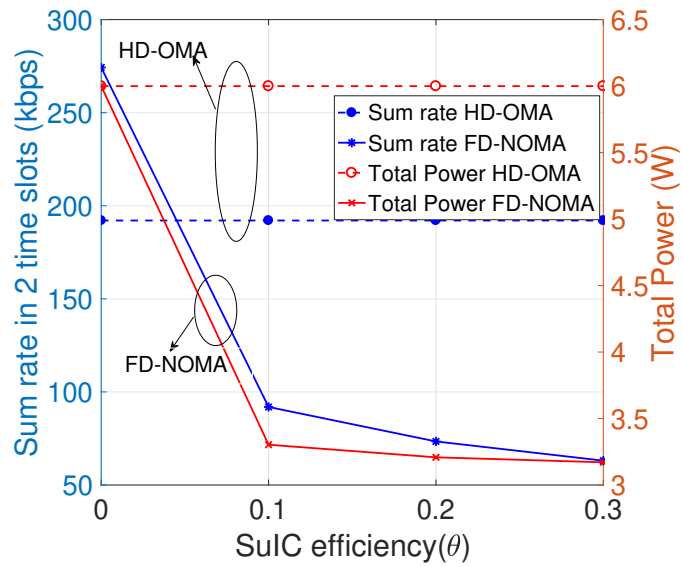
(b) SIC efficiency (λ) = 1.

Figure 2.4: Sum rate and total power vs. SuIC efficiency (θ) at different SIC efficiencies(λ).
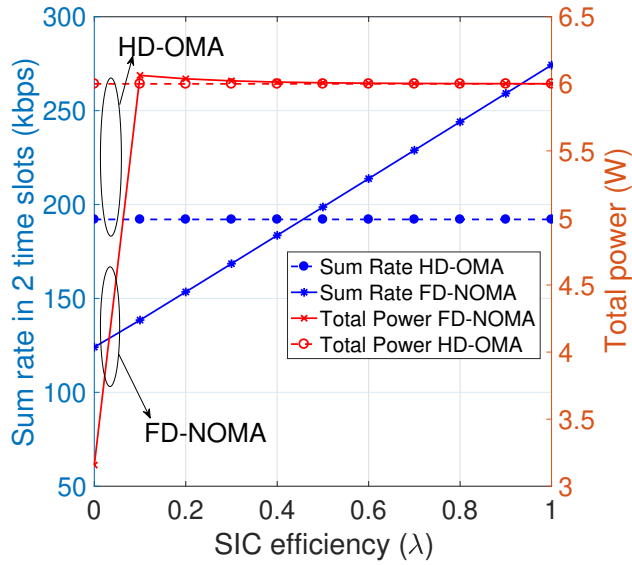
(a) SuIC efficiency $(\theta) = 0$.
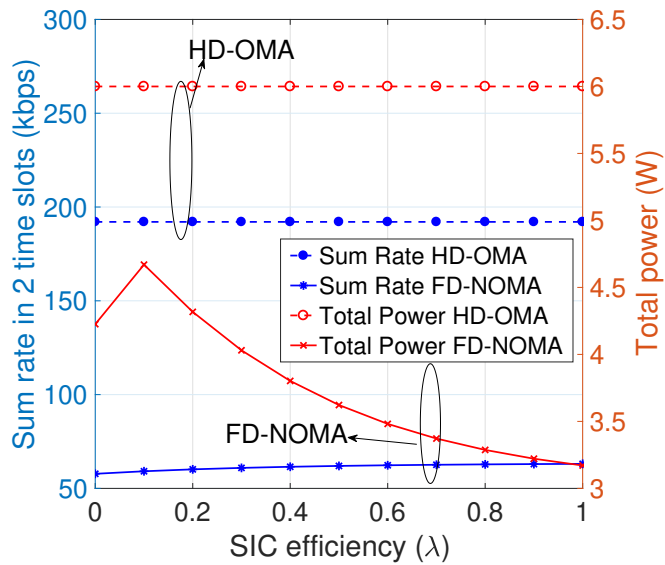
(b) SuIC efficiency $(\theta) = 0.3$.

Figure 2.5: Sum rate and total power vs. SIC efficiency (λ) at different SuIC efficiencies (θ).
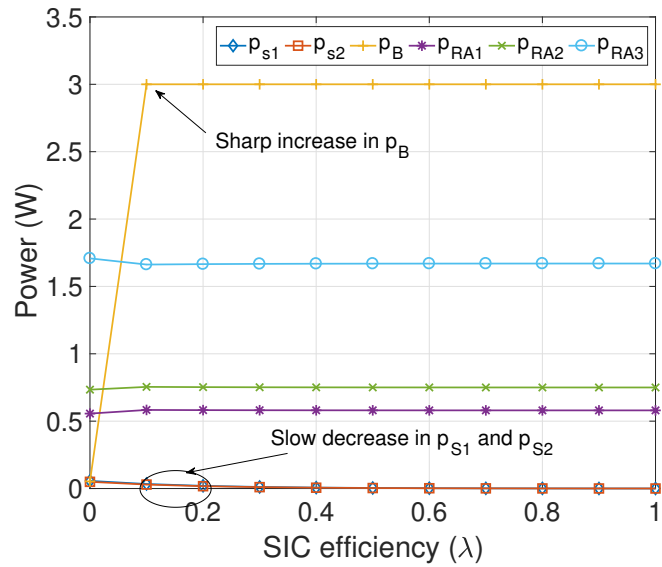
(a) SuIC efficiency (θ) =0.
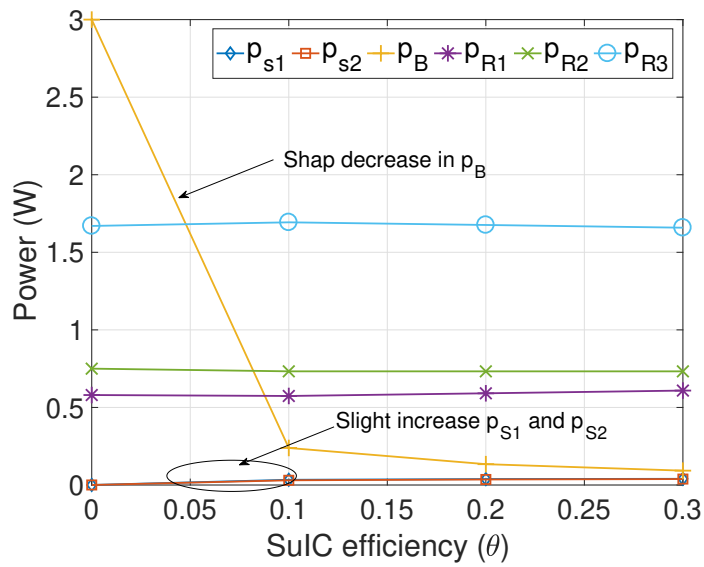
(b) SIC efficiency (λ) =1.

Figure 2.6: (a) Power vs. SIC efficiency (λ) at (θ) =0 (b) Power vs. SuIC efficiency (θ) at (λ)=1.

a non-zero value, the original term for the RSI is operational. Given that $\theta = 0$, the power increase at the bouy does not cause interference due to NOMA. Consequently, p_B goes to its maximum level; hence, the total power of the system increases. At the same time, as λ increases, the power needed by S_1 and S_2 to combat the interference decreases. This is not reflected in Fig. 2.5a for $0 \leq \lambda \leq 0.1$ due to the increase in p_B, but as p_B reaches its maximum, the effect of the decrease in p_{s_1} and p_{s_2} shows a slight decrease in the total power. The power at the relay exhibits similar performance as the buoy. Similarly, from Figs. 2.6b and 2.4b, when $\lambda = 1$, at $\theta = 0$, the buoy transmits at its maximum power. As θ increases, p_B decreases to avoid causing interference on other NOMA links. While, for the sensors, as the efficiency decreases, the power increases in an attempt to combat the effect of the interference. However, the effect from that slight increase is not reflected in Fig. 2.4b, because p_B continued to decrease at a higher rate than the increase in p_{S_1} and p_{S_2}.
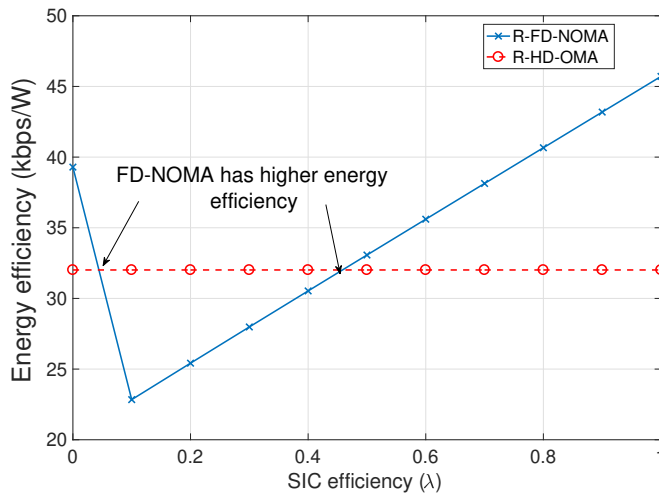
Figure 2.7: Energy efficiency vs. SIC efficiency (λ) at SuIC efficiency (θ) = 0.

In terms of power deficiency, at perfect SuIC with $\lambda = 0$, although the sum rate of R-FD-NOMA is lower than that of R-HD-OMA, R-FD-NOMA could be preferred because of higher energy efficiency as shown in Fig. 2.7.

2.7 Conclusion

In this chapter, R-FD-NOMA UWA was investigated in order to increase the sum rate of the UWA channel without utilizing additional radio resources. The proposed optimization problem varies the power level at the network devices to provide the highest possible sum rate. Expressions for the sum rate of the R-FD-NOMA UWA system were derived and the sum rate maximization problem was formulated. As the problem is non-convex, a low-complexity iterative algorithm was proposed to obtain a sub-optimal-solution. The problem was solved centrally at buoy. Numerical simulations showed a direct relation between the sum rate and the interference cancellation efficiency and advocates for relay- aided communications. The results showed that R-FD-NOMA performs better than R-HD-OMA at high SuIC efficiency. Given a perfect SuIC, an increase in the efficiency of the SIC provides a higher sum rate at a better energy efficiency when compared to R-HD-OMA as long as λ is greater than or equal to 0.4. For lower values of λ, R-HD-OMA provides better sum rate than R-FD-NOMA. However, R-FD-NOMA could be preferred at low SIC efficiency, where it may provide higher energy efficiency.

2.8 Acknowledgment

References

[1] S. Jiang, "On reliable data transfer in underwater acoustic networks: A survey from networking perspective," *IEEE Commun. Surveys Tuts.*, vol. 20, no. 2, pp. 1036–1055, Jan. 2018.

[2] C. GUSSEN, M. Campos, W. A. Martins, F. M. Costa, and J. N. Gois, "A survey of underwater wireless communication technologies," *J. Commun. Inf. Sys*, vol. 31, no. 1, pp. 242–255, Oct. 2016.

[3] A. Gkikopouli, G. Nikolakopoulos, and S. Manesis, "A survey on underwater wireless sensor networks and applications," in *Proc. Mediterranean Conference on Control Automation*, Barcelona, Spain, 2012, pp. 1147–1154.

[4] Y. Li, Y. Zhang, H. Zhou, and T. Jiang, "To relay or not to relay: Open distance and optimal deployment for linear underwater acoustic networks," *IEEE Trans. Commun.*, vol. 66, no. 9, pp. 3797–3808, Sep. 2018.

[5] A. Yadav and O. A. Dobre, "All technologies work together for good: A glance at future mobile networks," *IEEE Trans. Wireless Commun.*, vol. 25, no. 4, pp. 10–16, Aug. 2018.

[6] S. M. R. Islam, N. Avazov, O. A. Dobre, and K. Kwak, "Power-domain non-orthogonal multiple access (NOMA) in 5G systems: Potentials and challenges," *IEEE Commun. Surveys Tuts.*, vol. 19, no. 2, pp. 721–742, Oct. 2017.

[7] M. Duarte, C. Dick, and A. Sabharwal, "Experiment-driven characterization of full-duplex wireless systems," *IEEE Trans. Wireless Commun.*, vol. 11, no. 12, pp. 4296–4307, Dec. 2012.

[8] M. F. Kader, S. Y. Shin, and V. C. Leung, "Full-duplex non-orthogonal multiple access in cooperative relay sharing for 5G systems," *IEEE Transactions on Vehicular Technology*, vol. 67, no. 7, pp. 5831–5840, Jul. 2018.

[9] F. Qu, H. Yang, G. Yu, and L. Yang, "In-band full-duplex communications for underwater acoustic networks," *IEEE Netw.*, vol. 31, no. 5, pp. 59–65, Sept. 2017.

[10] J. Cheon and H. Cho, "Power allocation scheme for non-orthogonal multiple access in underwater acoustic communications," *Sensors*, vol. 17, no. 11, p. 2465, Oct. 2017.

[11] N. Shende, O. Gurbuz, and E. Erkip, "Half-duplex or full-duplex relaying: A capacity analysis under self-interference," in *Proc. Annual Conference on Information Sciences and Systems*, Baltimore, MD, USA, 2013, pp. 1–6.

[12] P. Qarabaqi and M. Stojanovic, "Statistical characterization and computationally efficient modeling of a class of underwater acoustic communication channels," *IEEE J. Ocean. Eng.*, vol. 38, no. 4, pp. 701–717, Oct. 2013.

[13] R. F. Coates, *Underwater Acoustic System*. MacMillan International Higher Education, 1990, ch. 6, pp. 90–100.

[14] A. Yadav, O. A. Dobre, and N. Ansari, "Energy and traffic aware full-duplex communications for 5G systems," *IEEE Access*, vol. 5, pp. 11 278–11 290, Jul. 2017.

[15] C. Canuto and A. Tabacco, *Taylor Expansions and Application*. Milano: Springer Milan, 2008, ch. 7, pp. 223–255.

[16] Evologics, "Underwater acoustic communication system s2cr 7/17d product information," Sep. 2016. [Online]. Available: https://goo.gl/2SW6Qn

[17] ——, "Usbl positioning and communication system s2cr 7/17 usbl product information," Jun. 2012. [Online]. Available: https://goo.gl/SMLFGE

[18] M. Stojanovic, "On the relationship between capacity and distance in an underwater acoustic communication channel," *ACM SIGMOBILE Mobile Computing and Communications Review*, vol. 11, no. 4, pp. 34–43, Oct. 2007.

[19] M. Grant and S. Boyd, "CVX: Matlab software for disciplined convex programming, version 2.1," http://cvxr.com/cvx, mar 2014.

[20] ——, "Graph implementations for nonsmooth convex programs," in *Recent Advances in Learning and Control*, ser. Lecture Notes in Control and Information Sciences, V. Blondel, S. Boyd, and H. Kimura, Eds. Springer-Verlag Limited, 2008, pp. 95–110.

Chapter 3

On the Security of Full-Duplex Relay-Assisted Underwater Acoustic Network with NOMA

3.1   Abstract

Wireless underwater acoustic (UWA) networks serve several civilian and military applications. The multiple reflections and dispersion, along with the long propagation delay limit the sum rate of UWA networks. Earlier works discussed adding full-duplex (FD), relay assistance, and non-orthogonal multiple access (NOMA) to enhance the system sum rate. Another challenge in UWA networks is the power limitation of devices. Hence, power optimization is crucial to maximize the energy efficiency. Furthermore, securing the UWA network against eavesdropping is essential to guaranteeing the confidentiality of communication. This work optimizes the power to maximize the secrecy sum rate (SSR) of a FD relay-assisted NOMA (FD-R-NOMA) underwater acoustic network subject to an eavesdropper (Eve) attack. The network is studied in two states: when the network has or has not the channel information (CI) of the threat. FD-R-NOMA UWA network shows to be more resilient to eavesdropping with higher secrecy energy efficiency when compared to the conventional half-duplex orthogonal multiple access network. Also, the results reveal that knowing the CI of Eve improves the SSR of the network.

Additionally, the results show the effect of factors like the location of Eve, interference cancellation efficiency, noise in the environment, and sensor distributions in the system.

3.2 Introduction

Reliable and secure underwater wireless communications are crucial for civilian applications, such as oil and gas exploration, pipeline monitoring, and environment monitoring, as well as for military applications [1]–[4]. Furthermore, underwater communication is essential to achieve the ubiquitous coverage targeted by 6G wireless [5]–[7]. Hence, there is an increased research interest to exploit its capabilities. Underwater communications have depended mostly on wired transmissions to maintain reliability and security [8]. However, the use of cables entails costly network deployment and difficulties in maintaining and repairing physical and chemical damages [8]. In recent years, there has been a shift towards wireless communications due to the ease of maintenance, flexibility and lower cost [8]. There are three wireless communications technologies used for underwater communications: radio frequency (RF), optical, and acoustic (UWA). While RF is the prevalent technology for terrestrial communications, it is not reliable for underwater communications due to the high absorption losses occurring in the underwater medium [2]. Optical communications requires line-of-sight, which is hard to guarantee in the underwater medium due to the presence of aquatic life, except for very short distances [2]. Acoustic communications is the most commonly used technology due to the long propagation range [2]. Still, there are several challenges in UWA communications, including multiple reflections, dispersion, and time-variations [1]. Besides, the UWA channel is characterized by long propagation delay due to the slow acoustic wave speed [1]. These characteristics limit the sum rate of UWA channels. Furthermore, underwater devices are power-limited, which deems energy efficiency as crucial [9], [10]. To increase the power utilization efficiency, channel reliability, and transmission distance, relay-assistance is used in UWA communications. Incorporating relays supports the communication systems by amplifying and forwarding or decoding and forwarding the data, among other strategies [9]–[12].

45

In terrestrial communications, full-duplex (FD) and non-orthogonal division multiple access (NOMA) have been proven to enhance the sum rate of the network without additional resources [13]–[15]. FD allows for simultaneous transmission and reception of signals on the same frequency. Theoretically, FD can double the sum rate of the channel compared to the conventional half duplex transmission mode. The self-interference (SI), caused by the FD operation, limits the rate enhancement [16], [17]. NOMA improves the sum rate by allowing the multiplexing of several users at the same time while using the same frequency resource [18], [19]. NOMA has shown the potential to augment spectral efficiency, balance user fairness, and increase the number of connections [11], [20]. There are two types of NOMA schemes, namely power domain and code domain [11], [20]. In the former, NOMA differentiates between users by assigning different power levels depending on the channel strength. In the latter, different codes are assigned to different users [11]. The network investigated in this chapter is power-domain NOMA. While NOMA enables multiple users to communicate using the same resource block, the interference from the other users needs to be canceled efficiently through successive interference cancellation (SuIC). The use of FD, NOMA, and relay-assisted communications in UWA has been investigated independently in [10], [20], [21]. For the first time in the literature, chapter 2 introduced an UWA network in which the FD relay-assisted NOMA (FD-R-NOMA) was applied to enhance the sum rate [22]. Given the confidentiality of most underwater communication applications, it is compelling to assess and enhance the security of a UWA system. There are two approaches to secure a system, namely computational security and information-theoretic security [23]. Computational security depends on ciphering the data in order to conceal it from attackers. All cryptography measures are based on the premise that it is computationally infeasible for the attackers to decipher the communication without knowledge of the secret key. However, with the relentless enhancements in computational abilities, there have been numerous cases where cryptography failed to secure the system [23]. Recently, the information-theoretic approach has been investigated both as an alternative and a complementary approach to conventional cryptography methods [24]. The information-theoretic methods depend on the physical layer characteristics to secure the data. Information-theoretic security

46

provides guarantees by requiring security to be a design constraint just like reliability. As a result, the design possibilities offered by an information-theoretic approach are invariant to the increase in the computational power of an adversary [23], [24]. Another disadvantage of the cryptographic schemes is the need to exchange the secret key between legitimate parties. Key sharing requires a trusted entity, which cannot always be ensured in distributed wireless networks, like wireless sensor networks and wireless ad-hoc networks [24]. On the other hand, the lower layers (physical and data link layers) are oblivious to any security considerations. Considering the recent challenges, physical layer security needs to be implemented to increase the robustness of existing schemes [24]. The fundamental principle behind physical layer security is to exploit the inherent randomness of noise and communication channels, as well as the capabilities of the information sources, to limit the amount of information that can be extracted at the bit level by an unauthorized receiver [25]. The attack might be by a jammer acting as a fake server, a fake device sending a large amount of information to cripple the network, or an eavesdropper (Eve) that listens to the communication. Physical security of the FD-R-NOMA UWA network has not been investigated in the literature. This chapter analyzes the physical security of an FD-R-NOMA UWA network against an Eve attack. The contributions of this chapter are as follows:

1. Assess the inherent security of a FD-R-NOMA network in an UWA environment against an Eve attack.

2. Formulate and solve an optimization problem to calculate the secrecy sum rate (SSR) in two cases:

    (a) If the system is oblivious to the presence of an Eve, and hence allocates the power to maximize the sum rate.

    (b) If the system adjusts the power based on the presence of an Eve and allocates the power to maximize the SSR.

3. Compare the performance of the system in the two aforementioned cases.

4. Compare the performance of the half-duplex orthogonal multiple access (HD-OMA) and FD-R-NOMA from the physical security perspective.

The remainder of this chapter is organized as follows: the system model is presented in Section 3.3. The optimization problems are formulated and solved in Section 3.4, and the results are discussed in Section 3.5. Finally, conclusions are drawn in Section 3.6.

3.3 System Model

In this chapter, a hierarchical UWA communication network consisting of a buoy (B), a FD-R, and two sensors S_1, S_2 is considered, as depicted in Fig. 3.1. An Eve is attempting to intercept the communication of the network. The network nodes, B, R, S_1, and S_2 are located at two dimensional coordinates of $[x_B, y_B]$, $[x_R, y_R]$, $[x_{S_1}, y_{S_1}]$ and $[x_{S_2}, y_{S_2}]$ respectively. The x co-ordinate represents the horizontal location of the node with respect to R, and the y co-ordinate represents the height of the node from the seabed. The sensors send data to R on the uplink (UL) channel, and R forwards the data to B. The UL-NOMA group is formed as $S_1{\rightarrow}R$, $S_2{\rightarrow}R$. R performs SuIC on the strong interfering signal in order to guarantee accurate signal detection. The SuIC efficiency is represented by $\theta \in [0,1]$, where $\theta=0$ denotes perfect SuIC. R decodes-and-forwards the received data to B.

The FD-R uses FD to receive data from the sensors and send data to B simultaneously. The FD transmission causes SI. The FD-R is equipped with a SI cancellation (SIC) unit. Residual SI (RSI) is calculated as [16]:

$$I = \frac{p_R^{(1-\lambda)}}{\beta\mu^{\lambda}},\tag{3.1}$$

where p_R denotes the transmit power of the FD-R, β and μ are the interference suppression factors due to the passive cancellation technique, and λ is the SIC factor. In this chapter, $\lambda=1$ represents the perfect SIC.
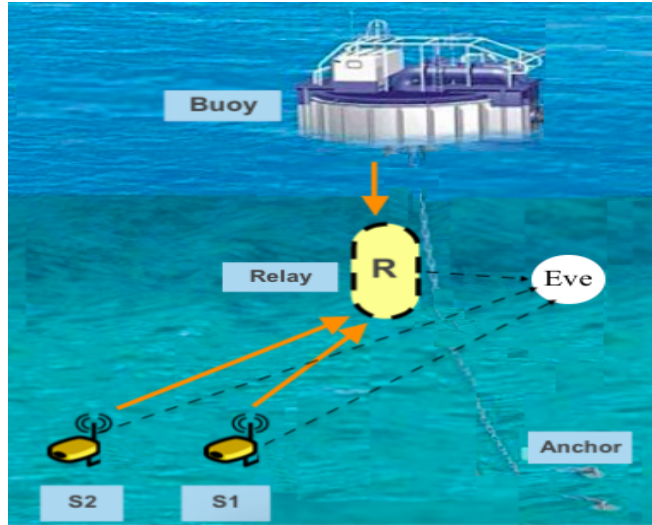
Figure 3.1: System model.

Underwater Channel Model: There is no standardized UWA channel model [26]. In this chapter, the large-scale fading is represented by the path loss model from [27], while the small-scale fading is modeled by Rayleigh fading [28]. In UWA communications, the path loss (A) is governed by the transmission frequency (f in kHz) and the transmission distance (l in km) [27] according to the expression

$$10 \log(A(l, f)) = 10k \log(1000l) + 10 \log(a(f)), \tag{3.2}$$

where $k \in [0,2]$ denotes the spreading factor that describes the geometry of propagation, e.g., $k = 2$ corresponds to spherical spreading, $k = 1$ to cylindrical spreading, and $k = 1.5$ to typical, practical spreading. $a(f)$ denotes the absorption coefficient given by the Thorp's formula in (dB/km) as [27],

$$10 \log(a(f)) = \frac{0.11 f^2}{1 + f^2} + \frac{44 f^2}{4100 + f^2} + 2.75(10^{-4}) f^2 + 0.003. \tag{3.3}$$

Ambient Noise Model: The ambient noise has four components, namely: turbulence noise, shipping noise, wave noise, and thermal noise, represented by the power spectral densities (PSDs) $N_t(f)$, $N_s(f)$, $N_w(f)$, and $N_{th}(f)$, respectively. The empirical formulas in (3.4) give the individual PSDs of these noise components in dB re μ Pa per Hz as a function of frequency (f in kHz) [29]:

$$N_t(f) = 17 - 30 \, \log f,$$

$$N_s(f) = 40 + 20 \, (s - 0.5) + 26\log f - 60 \, \log(f + 0.03),$$

$$N_w(f) = 50 + 7.5w^{1/2} + 20\log f - 40 \, \log(f + 0.4),$$

$$N_{th}(f) = -15 + 20 \, \log f, \tag{3.4}$$

where $s \in [0,1]$ depends on the level of ship activity and w denotes the wind speed in m/s. The four components added together represent the PSD of the ambient noise, $N_a(f)$, in the underwater environment. In order to convert the PSD from acoustic to electrical domain (W/Hz), the following formula is used [10]:

$$N(f) = \frac{10^{-17.2} N_a(f)}{\phi}, \tag{3.5}$$

where $N(f)$ is the equivalent electrical noise PSD and ϕ denotes the efficiency of the electric circuit in converting the acoustic power to electrical power. The noise power σ_N^2 can be easily calculated over a frequency band. The maximum link sum rate (C in bps/Hz) is calculated as:

$$C = \log_2(1 + \gamma), \tag{3.6}$$

where γ is the signal-to-interference-plus-noise ratio (SINR) of the link. The SINR for the channels $S_1 \rightarrow R$, $S_2 \rightarrow R$, and $R \rightarrow B$, are respectively defined as:

$$\gamma_1(\mathbf{p}) = \frac{p_{S_1} G_{S_1,R}}{p_{S_2} G_{S_2,R} + I + \sigma_N^2}, \tag{3.7}$$

$$\gamma_2(\mathbf{p}) = \frac{p_{S_2} G_{S_2,R}}{\theta p_{S_1} G_{S_1,R} + I + \sigma_N^2}, \tag{3.8}$$

$$\gamma_3(\mathbf{p}) = \frac{p_R G_{R,B}}{p_{S_1} G_{S_1,B} + p_{S_2} G_{S_2,B} + \sigma_N^2}, \tag{3.9}$$

where p_{S_a} is the transmit power of sensor $a = 1, 2$, p_R is the transmit power of R, and I denotes the RSI at R. The channel gains between $S_1 \rightarrow R$, $S_2 \rightarrow R$, and $R \rightarrow B$ are symbolized by $G_{S_1,R}$, $G_{S_2,R}$, and $G_{R,B}$,

respectively.

In this chapter, it is assumed that Eve listens to the communication, as shown in Fig. 3.1. The channel gains at Eve with respect to the sender nodes S_1, S_2, and R are denoted by $G_{S_1,E}$, $G_{S_2,E}$, and $G_{R,E}$, respectively. The location of Eve in the two-dimensional plane is [x_E, y_E]. Although all communications happen at the same time, I assume that each signal reaches Eve on its own time, due to propagation delays; hence, Eve could differentiate the signals. This represents a worst case scenario; in general, Eve would not be able to differentiate the communication from one source or the other. This chapter assumes that Eve is moving around in the water at different locations and the centralized optimization decision-maker (B) may or may not know the channel information (CI) of Eve; accordingly, both situations are investigated.

3.4 SSR Optimization

The legitimate sum rate (C_L) is the sum rate between the two communicating nodes. SSR is the amount of information that can be sent, not only reliably, but also confidentially in the presence of an Eve. Eve sum rate (C_E) is the sum rate Eve can achieve using the channel between Eve and the sender. The system SSR (C_S) is calculated as:

$$C_S = C_L - C_E = \log_2(1 + \gamma_i) - \log_2(1 + \gamma_{i_E}). \tag{3.10}$$

C_L and C_E are calculated based on Shannon's formula, where γ_i is the SINR on link i and γ_{i_E} is the SINR on the channel between Eve and the sender on that link. For each link, γ_{i_E} is calculated as follows:

$$\gamma_{1_E}(\mathbf{p}) = \frac{p_{S_1} G_{S_1,E}}{p_{S_2} G_{S_2,E} + p_R G_{R,E} + \sigma_N^2}, \tag{3.11}$$

$$\gamma_{2_E}(\mathbf{p}) = \frac{p_{S_2} G_{S_2,E}}{p_{S_1} G_{S_1,E} + p_R G_{R,E} + \sigma_N^2}, \tag{3.12}$$

$$\gamma_{3_E}(\mathbf{p}) = \frac{p_R G_{R,E}}{p_{S_1} G_{S_1,E} + p_{S_2} G_{S_2,E} + \sigma_N^2}. \tag{3.13}$$

This chapter considers two possible scenarios: the system has knowledge of the CI of Eve, and it has no knowledge.

3.4.1 Unknown CI of Eve

If the CI of Eve is unknown to B, the power is optimized in order to increase the system's legitimate sum rate irrespective of the SSR. Based on that the objective of the optimization function is the maximization of the legitimate sum rate of the system. The C_L maximization problem is formulated using equations (3.7)-(3.9), where the relationship between the rate and the SINR (γ) of a channel is expressed as per (3.6) in bps/Hz. The goal is to obtain the optimal transmit powers of the sensors, B, and R. The optimization problem is thus expressed as:

$$\max_{\mathbf{p}} \quad \sum_{i=1}^{3} \log_2(1 + \gamma_i(\mathbf{p})) \tag{3.14}$$

$$\text{s.t.} \quad C_{\min} \leq C_{S_1,R}, C_{\min} \leq C_{S_2,R}, \tag{3.14a}$$

$$C_{S_1,R} + C_{S_2,R} \leq C_{R,B}, \tag{3.14b}$$

$$0 \leq p_{S_1} \leq \bar{p}_{S_1}, 0 \leq p_{S_2} \leq \bar{p}_{S_2},$$

$$0 \leq p_R \leq \bar{p}_R, \tag{3.14c}$$

where $\bar{p}_{S_1}$, $\bar{p}_{S_2}$, $\bar{p}_B$, and $\bar{p}_R$ denote the maximum transmit powers of S_1, S_2, B, and R, respectively, and $C_{x,y}$ represents the rate of channel x→y. The constraints in (3.14a) guarantee that a minimum sum rate of $C_{\min}$ is achieved on each channel. Constraint (3.14b) limits the sum rates of UL channels C_{S,R_1} and C_{S,R_2} to their achievable capacities, $C_{R,B}$ and $C_{B,R}$, respectively. Furthermore, constraint (3.14c) limits the transmission power of the nodes.

Problem (3.14) is non-convex because of the non-convexity in the objective function (3.14) and the constraint (3.14b). $\gamma_i(\mathbf{p})$ is a fraction of two functions in $\mathbf{p}$. The linearity of $\gamma_i(\mathbf{p})$ is not conserved due

to the division of these functions. Therefore, (3.14) and (3.14b) are non-convex. Consequently, optimally solving this problem is computationally exigent. To solve (3.14) more efficiently, the resulting problem will be transformed and approximated by a convex problem, and then a convergent iterative algorithm will be proposed as a solution.

First, two new slack x_i and y_i are introduced such that:

$$\gamma_i(\mathbf{p}) \triangleq \frac{\zeta_i(\mathbf{p})}{\omega_i(\mathbf{p})} \geq x_i \, \forall i, \tag{3.15}$$

$$x_i y_i \leq \zeta_i(\mathbf{p}) \, \forall i, \tag{3.16}$$

$$\omega_i(\mathbf{p}) \leq y_i \, \forall i. \tag{3.17}$$

After applying the transformation, (3.14) can be equivalently rewritten as:

$$\max_{\mathbf{p}, y_i, x_i} \quad \sum_{i=1}^{3} \log_2(1 + x_i) \tag{3.18}$$

$$\text{s.t.} \quad x_i y_i \leq \zeta_i(\mathbf{p}) \, \forall i, \tag{3.18a}$$

$$\omega_i(\mathbf{p}) \leq y_i \, \forall i, \tag{3.18b}$$

$$(3.14a) - (3.14c). \tag{3.18c}$$

The constraint (3.18a) incorporates the product of two variables x_i and y_i; therefore, it is neither concave nor convex. Besides, $\omega_i(\mathbf{p})$ has concave interference terms according to (3.7) and (3.8), and hence, the inequality in (3.18b) is not convex for all i. Whenever $\omega_i(\mathbf{p})$ has interference terms, the constraint in (3.18b) is not convex, as $\omega_i(\mathbf{p})$ is on the left-hand side of the inequality. The non-convex constraints are approximated by convex functions using (3.19) and (3.20), as follows:

For constraint (3.18a), the upper bound approximation is used as [30]:

$$f(x_i, y_i) = x_i y_i \leq F(x_i, y_i, \Lambda_i) \triangleq \frac{1}{2\Lambda_i} x_i^2 + \frac{\Lambda_i}{2} y_i^2 \, \forall \Lambda_i > 0. \tag{3.19}$$

For $\hat{\Lambda}_i = x_i/y_i$, it can be easily observed that $f(x_i, y_i) = F(x_i, y_{i,} \hat{\Lambda}_i)$ and $\nabla f(x_i, y_i) = \nabla F(x_i, y_{i,} \hat{\Lambda}_i)$, where ∇f represents the gradient of f.

For constraint (3.18b) and (3.14b) The first-order Taylor series. For (3.18b), I approximate $p^{(1-\lambda)}$, for

$0 \leq \lambda \leq 1$, with a first-order Taylor series at $p(n)$ as follows [31]:

$$I_{\mathrm{L}}(n+1) = \frac{(p_{\mathrm{R}}(n))^{(1-\lambda)}}{\beta\mu^{\lambda}} + (1-\lambda)\frac{(p_{\mathrm{R}}(n))^{(-\lambda)}}{\beta\mu^{\lambda}} \times (p_{\mathrm{R}} - p_{\mathrm{R}}(n)). \tag{3.20}$$

Using a similar approach, $C_{\mathrm{S_1,R}}$ and $C_{\mathrm{S_2,R}}$ are approximated as:

$$C_{\mathrm{S_1,R_L}}(n+1) = \log_2(1 + x_1(n)) + \frac{(x_1 - x_1(n))}{\log_2(1 + x_1(n))}, \tag{3.21}$$

$$C_{\mathrm{S_2,R_L}}(n+1) = \log_2(1 + x_2(n)) + \frac{(x_2 - x_2(n))}{\log_2(1 + x_2(n))}, \tag{3.22}$$

where n is the iteration index. Hence, the condition (3.14b) can be approximated as:

$$C_{\mathrm{S_1,R_L}} + C_{\mathrm{S_2,R_L}} \leq C_{\mathrm{R,B}}. \tag{3.23}$$

After applying the aforementioned transformations, (3.14) is equivalently rewritten as:

$$\max_{\mathbf{P}, y_i, x_i} \quad \sum_{i=1}^{3} \log_2(1 + x_i) \tag{3.24}$$

$$\text{s.t.} \quad p_{\mathrm{S_2}} G_{\mathrm{S_2,R}} + I_{\mathrm{L}}(n) + \sigma_N^2 - y_1 \leq 0, \tag{3.24a}$$

$$\theta p_{\mathrm{S_1}} G_{\mathrm{S_1,R}} + I_{\mathrm{L}}(n) + \sigma_N^2 - y_2 \leq 0, \tag{3.24b}$$

$$p_{\mathrm{S_1}} G_{\mathrm{S_1,R}} + p_{\mathrm{S_2}} G_{\mathrm{S_2,R}} + \sigma_N^2 - y_3 \leq 0, \tag{3.24c}$$

$$\frac{1}{2\hat{\Lambda}_i(n)}x_i^2 + \frac{\hat{\Lambda}_i(n)}{2}y_i^2 - \zeta_i(\mathbf{p}) \leq 0 \,\forall i, \tag{3.24d}$$

$$C_{\mathrm{S_1,R}L} + C_{\mathrm{S_2,R}L} \leq C_{\mathrm{R,B}}, \tag{3.24e}$$

$$(3.14a), (3.14c). \tag{3.24f}$$

Problem (3.24) is then solved iteratively using the proposed sum rate optimization algorithm summarized in Algorithm 2, where C_{tot} is the total sum rate on all channels and G is a set that consists of the channel gains, $G_{\mathrm{S_1,R}}$, $G_{\mathrm{S_2,R}}$, and $G_{\mathrm{R,B}}$.

The problem at the nth iteration is convex and the optimal solution of this iteration is a feasible input point to the problem at the $(n+1)$th iteration. The algorithm produces non-decreasing objective

---

Algorithm 2 Iterative Sum Rate Maximization Algorithm.

Input $\bar{p}_{S_1}$, $\bar{p}_{S_2}$, $\bar{p}_R$, G, λ, θ, σ^2, $C_{\min}$, and tolerance (ϵ)

Output $\mathbf{p}$ and C_{tot}.

Set $n := 0$ and initialize $\mathbf{p}(n)$, $y_i(n)$, $x_i(n)$, and $\hat{\Lambda}_i(n)$ by $\frac{x_i(n)}{y_i(n)}$.

1: **Repeat:**

2: Solve (3.24), for $\mathbf{p}^*$, y_i^*, x_i^* $\forall i$;

3: Set $n := n + 1$;

4: Update $x_i(n)$ by x_i^*, $y_i(n)$ by y_i^* and $\hat{\Lambda}_i(n)$ by $\frac{x_i^*}{y_i^*} \forall i$;

5: **Until** convergence of sum rate with tolerance ϵ.

---

function values at each iteration. The algorithm converges to a local optimal solution representing the network sum rate because the problem is bounded by the maximum power constraints. The resultant sum rate and the CI of Eve are used to calculate the SSR as per (3.10).

3.4.2 Known CI of Eve

If the CI of Eve is known, the system can calculate Eve's sum rate, and hence, maximize the SSR as:

$$\max_{\mathbf{p}} \quad \sum_{i=1}^{3} \log_2(1 + \gamma_i(\mathbf{p})) - \sum_{i=1}^{3} \log_2(1 + \gamma_{i_E}(\mathbf{p})) \tag{3.25}$$

$$\text{s.t.} \quad C_{\min} \leq C_{S_1,R}, C_{\min} \leq C_{S_2,R}, \tag{3.25a}$$

$$C_{S_1,R} + C_{S_2,R} \leq C_{R,B}, \tag{3.25b}$$

$$0 \leq p_{S_1} \leq \bar{p}_{S_1}, 0 \leq p_{S_2} \leq \bar{p}_{S_2}, 0 \leq p_R \leq \bar{p}_R, \tag{3.25c}$$

$$C_{S_1,E} \geq 0, C_{S_2,E} \geq 0, C_{R,E} \geq 0, \tag{3.25d}$$

where $C_{s_{a,E}}$ is the SSR at the link between $a=$ S$_1$, S$_2$, R, and Eve. Equations (3.25a) - (3.25c) are similar to (3.14a) - (3.14c), respectively. Equation (3.25a) ensures a minimum sum rate per link, (3.25b) limits the sum rate of the links of R from the two sensors to the sum rate between R and B, and (3.25c) guarantees a positive value for the power of each node. Finally, (3.25d) guarantees that the SSR of each link is above zero [32]. This condition might not be feasible in some situations, as similarly mentioned in [33]. In order to approximate $\log_2(1+\gamma_i(\mathbf{p}))$ into a convex function the same transformations are followed as in (3.15)-(3.17) and (3.19)-(3.22). For $-\log_2(1+\gamma_{i_E}(\mathbf{p}))$, two new slack variables x_{i_E} and y_{i_E} are used as follows:

$$\gamma_{i_E}(\mathbf{p}) \triangleq \frac{\zeta_{i_E}(\mathbf{p})}{\omega_{i_E}(\mathbf{p})} \leq x_{i_E} \ \forall i, \tag{3.26}$$

$$\zeta_{i_E}(\mathbf{p})y_{i_E} \leq x_{i_E} \ \forall i, \tag{3.27}$$

$$1 - \omega_{i_E}(\mathbf{p})y_{i_E} \leq 0 \ \forall i. \tag{3.28}$$

Utilizing the above approximations, (3.25) can be transformed into:

$$\max_{\mathbf{P},y_i,y_{i_E},x_i,x_{i_E}} \quad \sum_{i=1}^{3} \log_2(1+x_i) - \sum_{i=1}^{3} \log_2(1+x_{i_E}) \tag{3.29}$$

$$\text{s.t.} \quad p_{S_2}G_{S_2,R} + I_L(n) + \sigma_N^2 - y_1 \leq 0, \tag{3.29a}$$

$$\theta p_{S_1} G_{S_1,R} + I_L(n) + \sigma_N^2 - y_2 \leq 0, \tag{3.29b}$$

$$p_{S_1}G_{S_1,R} + p_{S_2}G_{S_2,R} + \sigma_N^2 - y_3 \leq 0, \tag{3.29c}$$

$$\frac{1}{2\hat{\Lambda}_i(n)}x_i^2 + \frac{\hat{\Lambda}_i(n)}{2}y_i^2 - \zeta_i(\mathbf{p}) \leq 0 \ \forall i, \tag{3.29d}$$

$$(\zeta_{i_E}(\mathbf{p})y_{i_E}) \leq x_{i_E} \ \forall i, \tag{3.29e}$$

$$1 - \omega_{i_E}(\mathbf{p})y_{i_E} \leq 0 \ \forall i, \tag{3.29f}$$

$$C_{S_1,R_L} + C_{S_2,R_L} \leq C_{R,B}, \tag{3.29g}$$

$$(3.25a) - (3.25d). \tag{3.29h}$$

the upper bound transformation is used as in (3.19) to approximate (3.29e), where $\Lambda_{i_\mathrm{E}} = \frac{\zeta_{i_\mathrm{E}}(\mathbf{p})}{y_{i_\mathrm{E}}}$. In order to approximate (3.29f) to a convex equation, the following transformation is applied:

$$1 \leq \omega_{i_\mathrm{E}}(\mathbf{p})y_{i_\mathrm{E}}, \tag{3.30}$$

$$1 \leq \frac{1}{4}(y_{i_\mathrm{E}} + \omega_{i_\mathrm{E}}(\mathbf{p}))^2 \quad - \frac{1}{4}(y_{i_\mathrm{E}} - \omega_{i_\mathrm{E}}(\mathbf{p}))^2,$$

$$1 + \frac{1}{4}(y_{i_\mathrm{E}} - \omega_{i_\mathrm{E}}(\mathbf{p}))^2 \quad \leq \frac{1}{4}(y_{i_\mathrm{E}} + \omega_{i_\mathrm{E}}(\mathbf{p}))^2,$$

$$\sqrt{1 + \frac{1}{4}(y_{i_\mathrm{E}} - \omega_{i_\mathrm{E}}(\mathbf{p}))^2} \leq \frac{1}{2}(y_{i_\mathrm{E}} + \omega_{i_\mathrm{E}}(\mathbf{p})),$$

$$\|0.5(y_{i_\mathrm{E}} - \omega_{i_\mathrm{E}}(\mathbf{p})), 1\|_2 \leq \frac{1}{2}(y_{i_\mathrm{E}} + \omega_{i_\mathrm{E}}(\mathbf{p})).$$

At this point, the constraints are resolved to either linear or convex constraints; however, the objective function is still non-convex because the subtraction of two convex functions is not universally convex; so, it is converted as:

$$\sum_{i=1}^{3}(\log_2(1 + x_i) - \log_2(1 + x_{i_\mathrm{E}})) = \sum_{i=1}^{3} \log(\frac{1 + x_i}{1 + x_{i_\mathrm{E}}}). \tag{3.31}$$

Similar to (3.15), two new slack variables u_i and v_i are incorporated , where

$$\frac{1 + x_i}{1 + x_{i_\mathrm{E}}} \geq u_i \, \forall i, \tag{3.32}$$

$$u_i v_i \leq 1 + x_i \, \forall i, \tag{3.33}$$

$$1 + x_{i_\mathrm{E}} \leq v_i \, \forall i. \tag{3.34}$$

After applying the transformation (3.31)-(3.34), and an upper bound transformation (3.19) on (3.33),

using $\Lambda_{i_2} = \frac{u_i(n)}{v_i(n)}$, (3.29) can be equivalently rewritten as:

$$\max_{\mathbf{p}, y_i, y_{i_E}, x_i, x_{i_E}, u_i, d_i} \quad \sum_{i=1}^{3} \log_2(u_i) \tag{3.35}$$

$$\text{s.t.} \quad p_{S_2} G_{S_2,R} + I_L(n) + \sigma_N^2 - y_1 \leq 0, \tag{3.35a}$$

$$\theta p_{S_1} G_{S_1,R} + I_L(n) + \sigma_N^2 - y_2 \leq 0, \tag{3.35b}$$

$$p_{S_1} G_{S_1,B} + p_{S_2} G_{S_2,B} + \sigma_N^2 - y_3 \leq 0, \tag{3.35c}$$

$$\frac{1}{2\hat{\Lambda}_i(n)} x_i^2 + \frac{\hat{\Lambda}_i(n)}{2} y_i^2 - \zeta_i(\mathbf{p}) \leq 0 \,\forall i, \tag{3.35d}$$

$$\frac{1}{2\hat{\Lambda}_{i_E}(n)} \zeta_i(\mathbf{p})^2 + \frac{\hat{\Lambda}_{i_E}(n)}{2} y_{i_E}^2 - (1 + x_{i_E}) \leq 0 \,\forall i, \tag{3.35e}$$

$$\frac{1}{2\hat{\Lambda}_{i_2}(n)} u_i^2 + \frac{\hat{\Lambda}_{i_2}(n)}{2} v_i^2 - (1 + x_i) \leq 0 \,\forall i, \tag{3.35f}$$

$$(1 + x_{i_E}) - d_i \leq 0 \,\forall i, \tag{3.35g}$$

$$\|0.5(y_{i_E} - \omega_{i_E}(\mathbf{p})), 1\|_2 \leq \frac{1}{2}(y_{i_E} + \omega_{i_E}(\mathbf{p})), \tag{3.35h}$$

$$(3.29g) - (3.29h). \tag{3.35i}$$

The pseudocode for the proposed SSR optimization is summarized in Algorithm 3.

In Algorithm 3, $C_{S_{tot}}$ is the total SSR on all channels, and G_E is a set that includes the channel gains between Eve and the network nodes, $G_{S_1,E}$, $G_{S_2,E}$, and $G_{R,E}$.

Problem (3.35) is solved iteratively using Algorithm 3. The convexity of the problem at the nth iteration is achieved. Similar to Algorithm 2, Algorithm 3 converges to a local optimal solution, which is used to calculate the SSR of the network.

Algorithm 3 Iterative SSR Maximization Algorithm.

Input $\bar{p}_{\mathrm{S}_1}$, $\bar{p}_{\mathrm{S}_2}$, $\bar{p}_{\mathrm{R}}$, G, G_{E}, λ, θ, σ^2, $C_{\min}$, and tolerance (ϵ).

Output p and $C_{S_{\mathrm{tot}}}$.

Set $n := 0$ and initialize $\mathbf{p}(n)$, $y_i(n)$, $x_i(n)$, $y_{i_{\mathrm{E}}}(n)$, $x_{i_{\mathrm{E}}}(n)$, $u_i(n)$, $v_i(n)$, $\hat{\Lambda}_i(n)$ by $\frac{x_i(n)}{y_i(n)}$, $\hat{\Lambda}_{i_2}(n)$ by $\frac{u_i(n)}{v_i(n)}$ and $\hat{\Lambda}_{i_{\mathrm{E}}}(n)$ by $\frac{x_{i_{\mathrm{E}}}(n)}{y_{i_{\mathrm{E}}}(n)}$.

1: **Repeat:**

2: Solve (3.35), for $\mathbf{p}^*$, y_i^*, x_i^*, $y_{i_{\mathrm{E}}}^*$, $x_{i_{\mathrm{E}}}^*$, u_i^*, v_i^* $\forall i$;

3: Set $n := n + 1$;

4: Update all parameters with corresponding values from the iteration (n);

5: **Until** convergence of SSR with tolerance ϵ.

3.5   Results and Discussion

This section studies the performance of an FD-R-NOMA UWA network with respect to the SSR and energy efficiency. The optimization problems from Section 3.4, (3.24) and (3.35), are solved centrally at B. The algorithms are implemented using CVX with SEDUMI as internal solver on Matlab [36], [37]. The employed system parameters are given in Table 1, unless otherwise mentioned. It is assumed that Eve moves from the left hand-side (LHS) to the right hand-side (RHS), in all scenarios. The SSR of FD-R-NOMA with and without knowledge of Eve's CI, are compared. Then, the performance of FD-R-NOMA is evaluated versus the performance of HD-OMA in terms of SSR, energy efficiency, and feasibility. Afterwards, the effect of the depth of Eve, interference cancellation efficiency, noise and sensor distribution on the SSR of a FD-R-NOMA UWA system is investigated.

Table 3.1: Simulation parameters.

Parameter	Value
System Parameters	
Water depth	1000 m
R coordinates	[0 m, 0.5 depth m]
B x and y coordinates	[0 m, 1000 m]
S_1 x and y coordinates	[-1050 m, 0 m]
S_2 x and y coordinates	[-3100 m, 0 m]
Eve x-coordinates	[-30e3 : 30e3 m]
Eve y-coordinates	0.5 depth m
Maximum power of each sensor	3 W [34]
Maximum power of R	3 W [35]
C_{min}	25 kbps
ϵ	0.5 kbps
Channel Parameters	
SuIC efficiency θ	0 [22]
SIC efficiency λ	1 [22]
Bandwidth	5.5 kHz [26]
Minimum frequency	10 kHz [26]
Spreading factor k	1.5 [26]
Shipping activity s	1 [27]
Speed of wind w	10 m/s [27]
Conversion efficiency Φ	1 [10]
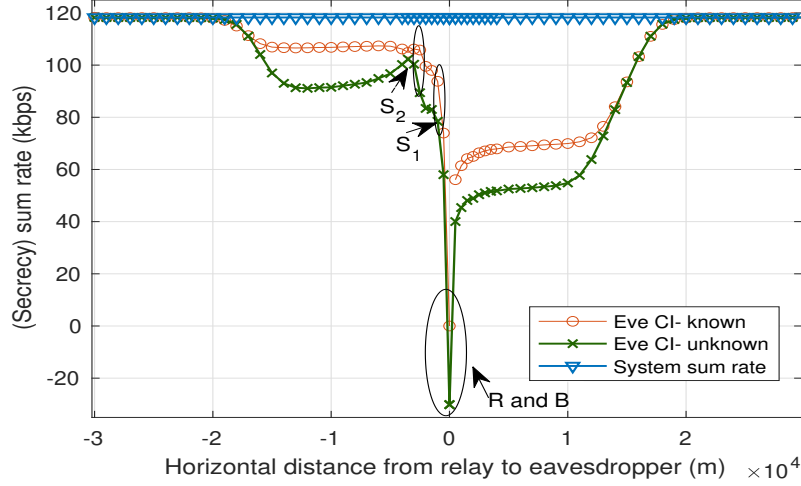
Figure 3.2: The achievable sum rate and the SSR vs. the horizontal distance between R and Eve.

3.5.1 FD-R-NOMA with and without CI knowledge versus HD-NOMA

3.5.1.1 SSR

The SSR of FD-R-NOMA with CI knowledge is compared versus FD-R-NOMA without CI knowledge; then, the worst of the two is compared with HD-OMA.

Fig. 3.2 shows the achievable system sum rate and the SSR if Eve's CI is known or not. The knowledge of Eve's CI allows the system to make better decisions when assigning the power. Therefore, it guarantees better SSR compared to not knowing Eve's CI, while Eve is at the vicinity of the network. As Eve moves farther from the network, its capability to intercept the communication diminishes; hence, the SSR for both cases becomes similar.

Fig. 3.2 also illustrates that when Eve is on the RHS of R and B, the SSR is lower. As Eve moves to the RHS of R, the interference from the sensors declines. In addition, the sum rate of the link between R and B, by definition, is greater than the sum rate of the other links as per (3.14b) and (3.25b). Hence, the SSR decreases, as Eve is capable of intercepting the communication on R →B better when located on the RHS of R and B.

Furthermore, Fig. 3.2 shows that problem (3.14) is infeasible from 0 to 400 m on the RHS of R for FD-R-NOMA with Eve's CI knowledge. As mentioned earlier, at some locations of Eve, it is infeasible
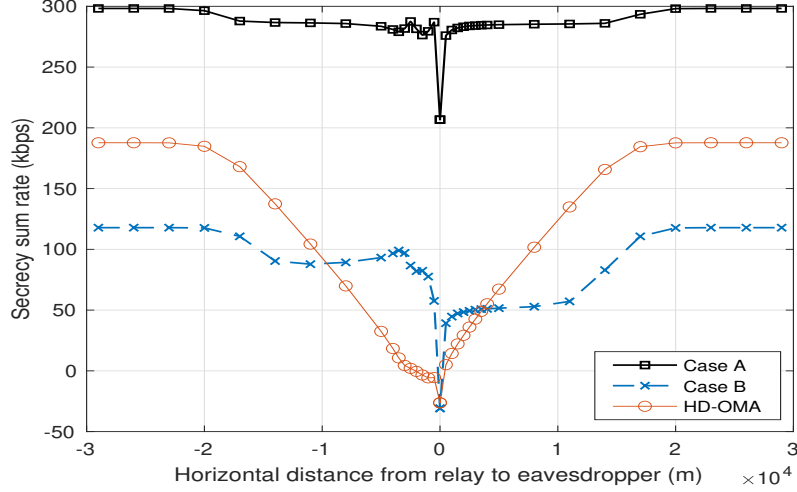
Figure 3.3: SSR of FD-R-NOMA case A, FD-R-NOMA case B, and HD-OMA vs. the horizontal distance between R and Eve.

to achieve the minimum secrecy rate per link. Given that problem (3.14) is conditioned on the secrecy rate per link, it is not possible to calculate the power per node or the SSR at these locations of Eve (in our case it is from 0 to 400 m). For FD-R-NOMA without the knowledge of Eve's CI, the SSR is calculated, irrespective of the feasibility of the secrecy rate per link, as the secrecy rate per link is not a condition of (3.25). The feasibility of securing the communication for FD-R-NOMA with and without the knowledge of Eve's CI, and HD-OMA is studied later in this section.

Fig. 3.3 compares the SSR of FD-R-NOMA without CI knowledge, without and with interference from $G_{s_1,B}$ and $G_{s_2,B}$ (case A and case B respectively), with the SSR of HD-OMA.[1] It is expected that applying FD and NOMA provides better SSR when compared to HD-OMA, due to the better utilization of resources. However, the interference from $G_{s_1,B}$ and $G_{s_2,B}$ shown in (3.9) affects the SSR of FD relay-assisted NOMA (FD-R-NOMA). FD-R-NOMA has a better SSR compared to HD-OMA when Eve is moving from -10 km (10 km to the LHS) to 5 km (to the RHS) of R in both cases. However, as Eve moves farther from the system, the performance of HD-OMA becomes better than FD-R-NOMA with

---

[1]Note that FD-R-NOMA with Eve's CI knowledge is omitted as its SSR is better than the case without Eve's CI knowledge, and for the readability of the figure.

interference from $G_{s_1,B}$ and $G_{s_2,B}$. When $G_{s_1,B}$ and $G_{s_2,B}$ are insignificant, the system secrecy rate for FD-R-NOMA is better than HD-OMA at all locations of Eve.

3.5.1.2 Secrecy of Communication

Figs. 3.4a, 3.4b, and 3.4c show the secrecy rate per link versus the horizontal distance between R to Eve for HD-OMA, FD-R-NOMA without and with Eve's CI knowledge. If the secrecy rate per any of the links is below zero, this indicates that it is infeasible to secure the system under the given constraints and conditions. The interference from the simultaneous communicating links in the FD-R-NOMA assists in securing the system, and makes it possible to maintain the security of the communication for more Eve locations than HD-OMA. Fig. 3.4a shows that the HD-OMA communication cannot be secured for 7000 m, 2500 m, and 1000 m for the time slots for S2$\rightarrow$ R, S1$\rightarrow$ R, and R$\rightarrow$ B, respectively. This averages to an insecure region of 3500 m. Figs. 3.4b and 3.4c illustrate that introducing FD-R-NOMA decreases the infeasible region to less than half, (around 1500 m) for FD-R-NOMA without knowing Eve's CI, and to nearly one third (400 m) with knowledge of Eve's CI.

3.5.1.3 Secrecy Energy Efficiency (SEE)

SEE is the ratio of the achievable SSR to the total consumed power of the system [38]. Fig. 3.5 depicts the SEE versus the horizontal distance between Eve and R, in FD-R-NOMA with and without Eve's CI knowledge and HD-OMA. It shows that FD-R-NOMA is more energy efficient than HD-OMA for all Eve's locations, except when Eve is at R. At R, the energy efficiency of the three systems (HD-OMA, FD-R-NOMA with CI known/ unknown) are nearly the same. However, as previously discussed, it is infeasible to maintain the security close to R, and hence, the SEE is not applicable. Furthermore, the results illustrate that Eve's CI knowledge has a significant effect on the SEE. It compels the system to assign the power in order to maximize the SSR, and decreases the power utilization; hence, it increases the energy efficiency. It can be noticed that the SEE of the FD-R-NOMA with CI knowledge can be more efficient that FD-R-NOMA without CI knowledge by up to 6 kbps/W.
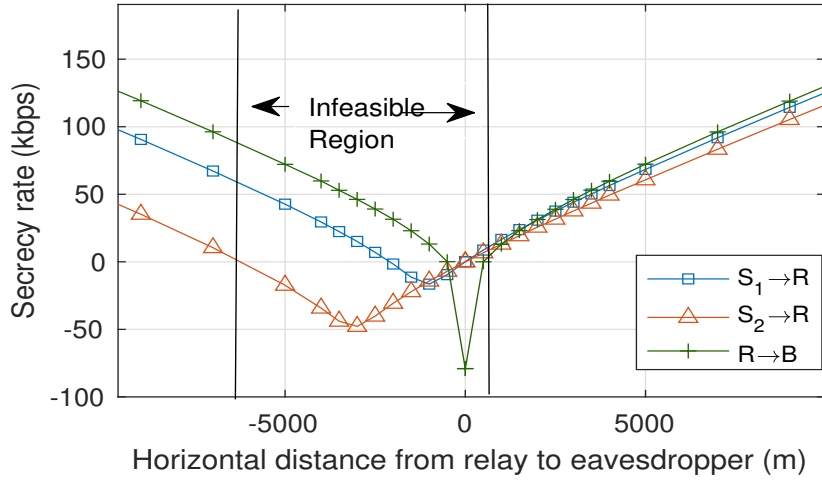
(a) HD-OMA.
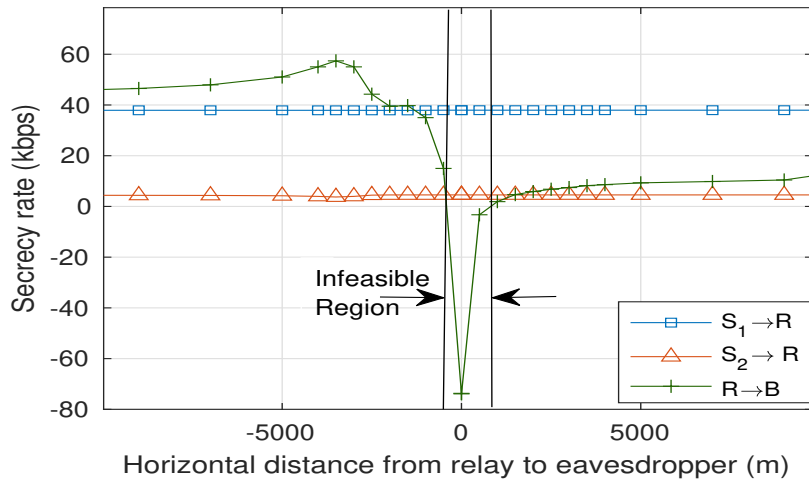
(b) FD-R-NOMA without knowledge of Eve's CI.
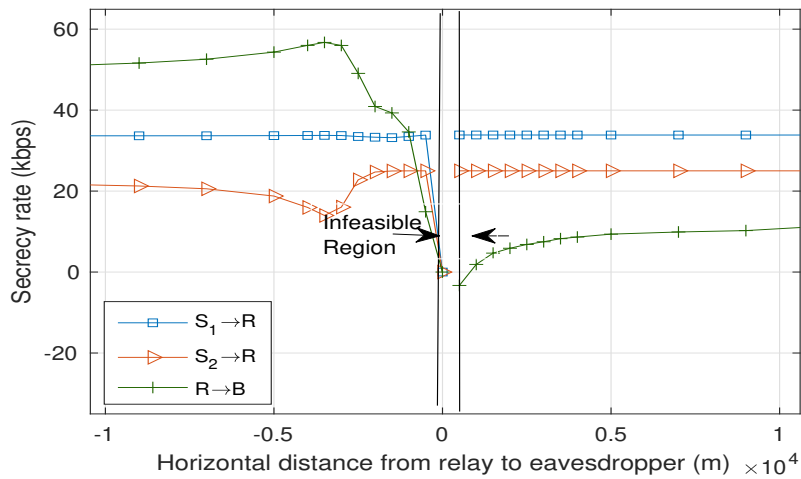
(c) FD-R-NOMA with knowledge of Eve's CI.

Figure 3.4: Secrecy rate per link vs. the horizontal distance from R to Eve.
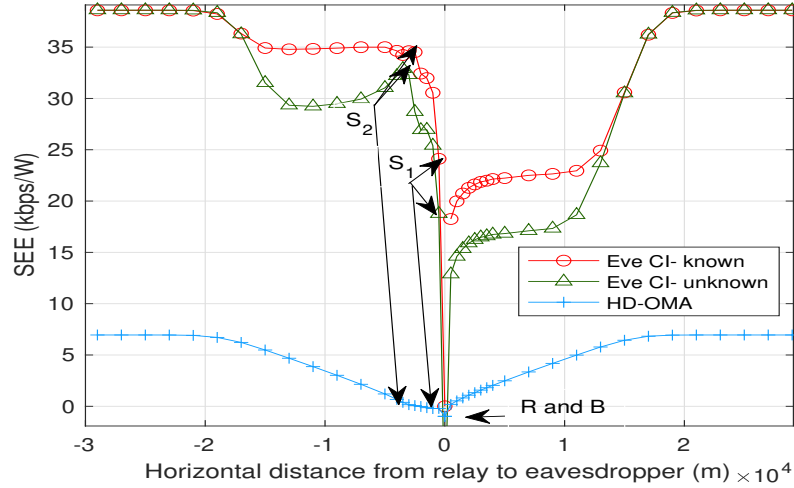
Figure 3.5: SEE for FD-R-NOMA with and without knowledge of Eve's CI and HD-OMA vs. the horizontal distance from R to Eve.

3.5.2 FD-R-NOMA with Eve's CI: Investigating the Effect of Changing Parameters

This subsection investigates the effect of the change of different parameters on the SSR of a network with FD-R-NOMA with Eve's CI.

3.5.2.1 Depth of Eve

Fig. 3.6a depicts the effect of changing Eve's depth on the SSR versus the horizontal location of Eve. The figure illustrates the variation in the SSR of the network with Eve at different depths, namely 0 m, 200 m, 500 m, 800 m, and 1000 m. For the purpose of this chapter, I assume that Eve moves from the LHS to the RHS of the network. As shown in the figure, the change in the depth of Eve causes only a minor change of the SSR. The most change is noticeable when one of the sensors and Eve overlap. When Eve is at or close to the sea bed (0 m and 200 m), Eve is at a close vertical location from the sensors. Hence, as it approaches the sensors horizontally from the LHS, the capability of Eve to listen to the communication from the sensors increases, and thus, the SSR decreases. This is shown in Fig. 3.6a: as Eve moves close to S_2, the SSR exhibits a sharp dip because Eve is very close to S_2,
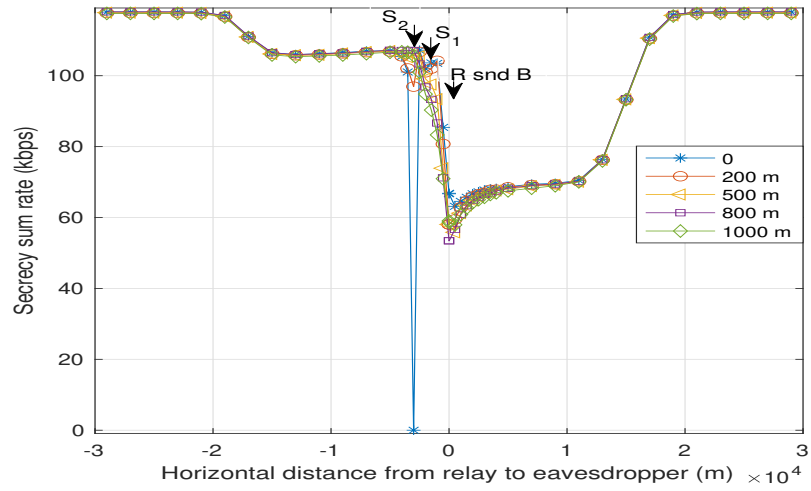
(a) Water depth is 1000 m.
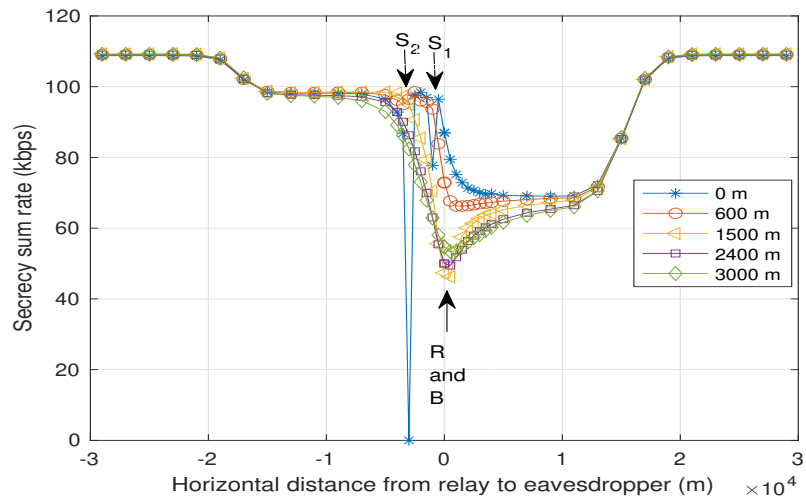
(b) Water depth is 3000 m.

Figure 3.6: SSR for different depths of Eve vs. the horizontal distance from R to Eve.

while still far from possible interference from other links. As Eve moves towards the RHS, the SSR improves because the interference from the legitimate communication escalates gradually, decreasing the capability of Eve to intercept the data from S_2. As Eve approaches S_1, it can better intercept the communication between S_1 and R, so another dip in the SSR occurs. It should be noted that the dip in SSR at S_1 is not as steep as the dip that occurs at S_2. The reason for the aforementioned behavior is that S_1 is closer to the rest of the network nodes, and consequently, Eve is susceptible to more interference than when located at S_2. Another behavior that can be observed from Fig. 3.6a is that the SSR decreases as Eve approaches R horizontally, irrespective of the depth of Eve. This is because Eve's capability to intercept R$\rightarrow$ B increases, and hence, the SSR decreases. It should be noted that the link R$\rightarrow$ B has the highest sum rate as per equation (25b). Consequently, the SSR is affected the most when the security of the link R$\rightarrow$ B is compromised. As Eve goes further from the sensors vertically (500 m to 1000 m), the vertical distance between Eve and the sensors is enough to secure the communication from the sensor, irrespective of the horizontal location of Eve. Hence, it is feasible to maintain high SSR of all the studied horizontal locations of Eve, except when R and Eve nearly coincide (500 m vertically, 0 m horizontally). In spite of the information provided by Fig. 3.6a, it is hard to understand the full effect of the depth of Eve on the communication from the figure, as most of the curves overlap. In order to further investigate the effect of changing the depth of Eve, I increase the water depth to 3000 m and show results in Fig. 3.6b.

It can be seen that securing the communication when Eve is at 1500 m depth and 0 m horizontally is infeasible; hence, it is the worst location. This is because the locations of Eve and R coincide, which gives Eve high access to the data received and sent by R. As Eve goes further up or down, the SSR increases due to getting away from R. Moving towards the buoy allows Eve to better intercept the communication between R and B, and hence a lower SSR is achieved. As Eve goes downwards from R, the SSR increases due to the higher interference by the sensors. Hence, the network is more resilient to attacks when Eve is at the sea bed, due to the interference from S_1 and S_2, along with being at the farthest distance from R. Besides, if Eve's location coincides with one of the network nodes (same

vertical and horizontal coordinates), the capability of Eve to intercept the communication increases, causing a dip in the SSR.

3.5.2.2   Interference Cancellation Efficiency

In this section, the effect of interference cancellation (SuIC and SIC) efficiency is investigated. Fig. 3.7a shows the effect of varying the efficiency of the SuIC as 0, 0.0001, and 0.001. As the SuIC factor increases, the SuIC efficiency decreases, and the SSR decreases. When θ is zero, the interference from S_1 on the communication of $S_2 \rightarrow R$ is negligible. Hence, increasing θ degrades the system sum rate, which results in a decrease in the SSR.

Fig. 3.7b shows that a similar effect occurs as the SIC decreases from 1 to 0.7 and 0.5, respectively. It is shown that the SSR is lower when RSI exists, irrespective of the location of Eve. Further, the interference from the SI of the relay on Eve decreases the ability of Eve to intercept the communications at S_1. Thus, the improvement in the SSR as Eve moves between S_2 and S_1 enhances as the interference from SI increases.

3.5.2.3   Shipping and Wind Noises

Here, the effect of the noise on the SSR is studied. The shipping and the wind noises are dependent on the s and w factors, respectively. The typical values for s range from 0 to 1, denoting low and high shipping activity, respectively [27]. w represents the wind speed; the higher the wind speed is, the higher the noise caused by the wind is. In this chapter, it is assumed that harsh shipping noise conditions with a shipping factor of 1 and an average wind speed of 10 m/s, which is equivalent to a fresh breeze [39]. The chapter compares the previously mentioned setup with the case when the noise is minimal, with a shipping factor of 0 and the wind speed of 0 m/s. Fig. 3.8 shows the SSR versus the horizontal distance between Eve and R with a change in the noise level, high and low, representing the original setup and the low noise setup, respectively. When Eve is close to the system, the decrease of noise does not change the SSR. However, when Eve is far from the system, lower noise allows Eve to
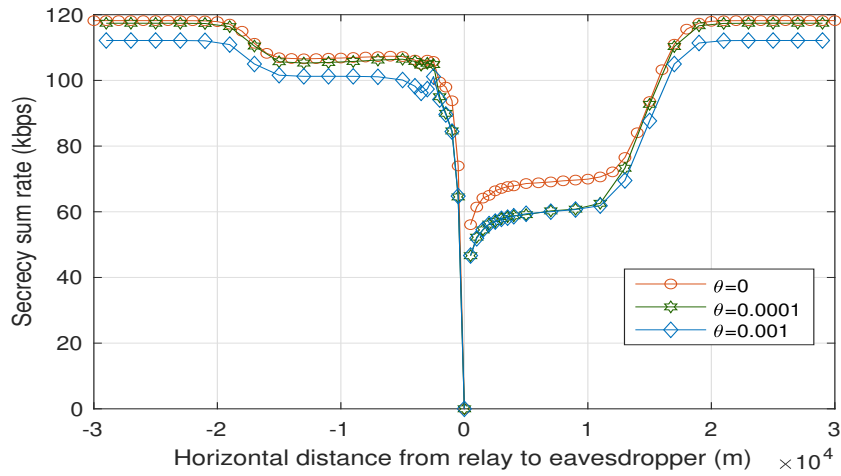
(a) Change of the SuIC efficiency at perfect SIC efficiency.
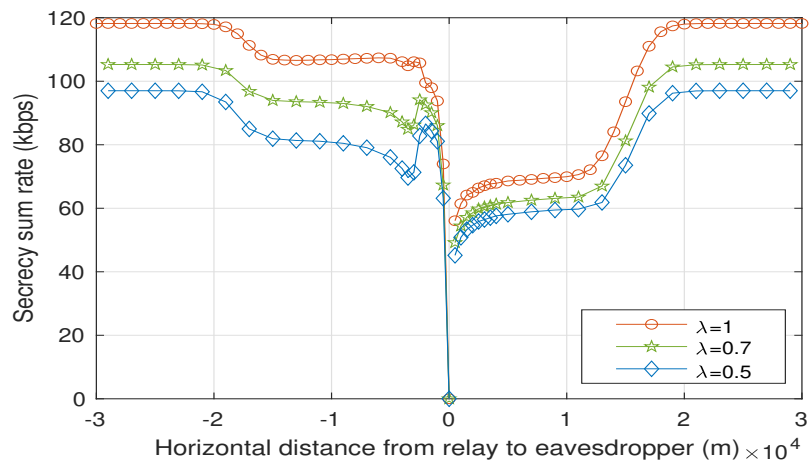
(b) Change of the SIC efficiency at perfect SuIC efficiency.

Figure 3.7: SSR vs. horizontal distance from R to Eve: efficiency of interference cancellation.
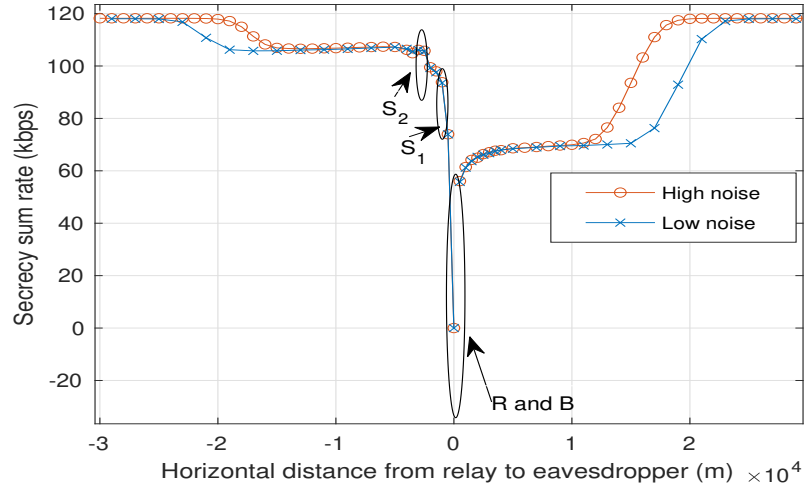
Figure 3.8: SSR for FD-R-NOMA with CI knowledge vs. the horizontal distance from R to Eve: change of the noise level.

tap the network from far distance, and hence, a lower SSR occurs. When Eve and R coincide, the SSR decreases sharply as explained earlier.

3.5.2.4 Sensor Distribution

The sensor distribution is an important factor in the SSR behavior. Fig. 3.9 presents the SSR versus the horizontal distance from Eve to R, where the sensors are distributed on the LHS, the RHS, and both sides of R, respectively. When the sensors are placed on one side, it can be noticed that there is asymmetry in the shape of the SSR curve. This happens because when Eve is on the same side as the sensors, the sensors interfere with the capability of Eve to tap the communication, and hence, the secrecy rate improves. However, when Eve moves to the other side (without the sensors), Eve can tap the communication between R and B, and the secrecy rate on the opposite side to the sensors drops. When the sensors are evenly distributed, they interfere on both sides and the SSR is similar on both sides. In all cases, as Eve gets far from the system nodes, the SSR improves.
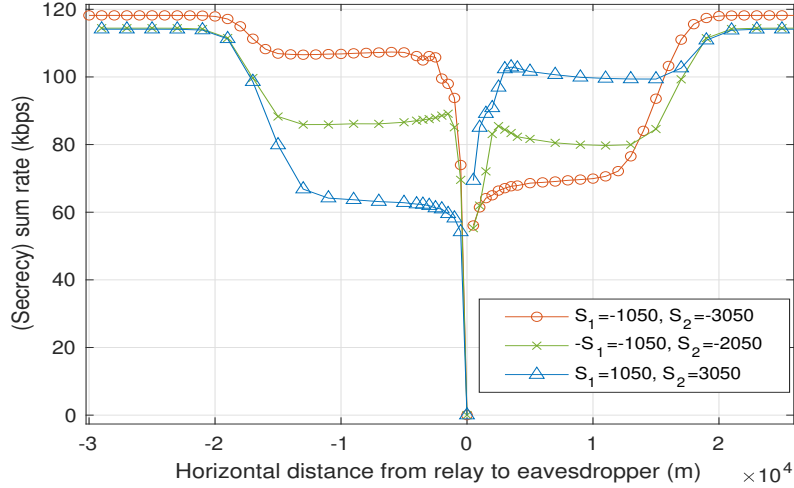
Figure 3.9: SSR for FD-R-NOMA with CI knowledge vs. the horizontal distance from R to Eve: Sensor Distribution

3.6 Conclusion

The study of secrecy of UWA networks is crucial due to the sensitivity of the applications of underwater communication. In this chapter, the secrecy performance of a FD-R-NOMA network has been studied. A power allocation problem has been solved in order to maximize the SSR under two scenarios, namely in the presence and absence of Eve's CI knowledge. The problem has been approximated by a convex problem and solved. The SSR of FD-R-NOMA with and without knowledge of Eve's CI has been compared. The performance of FD-R-NOMA has been also evaluated versus the performance of HD-OMA in terms of SSR, energy efficiency, and feasibility. FD-R-NOMA has better resilience to an Eve attack, as it maintains better feasibility to secure the network at higher SEE when compared to HD-OMA. Knowing Eve's CI increases the SSR, decreases the possibility of a security breach, and increases SEE. Furthermore, the effect of different factors, like the depth of Eve, interference cancellation efficiency, noise and sensor distribution, on FD-NOMA has been studied. It has been found that Eve's depth affects the SSR differently, depending on the water's depth. At a water depth of 1000 m, the change in Eve's depth is not effective on the sum rate. At a water depth of 3000 m, as Eve gets closer to R, the SSR decreases. It has been shown that improving the interference cancellation efficiency,

whether SuIC or SIC, improves the SSR. In addition, it has been illustrated that changes in the shipping and wind noises do not affect the SSR when Eve is close to the system. However as Eve goes farther, lower noise allows for better tapping of the communication, and hence, decreases the SSR. The change in the distribution of the sensors affects the SSR, as it changes the interference Eve is subject to. As Eve approaches a sensor or multiple sensors, the interference affects the ability of Eve to monitor the communication, which increases the SSR. In future work, the expansion of the system is considered to include multiple sensors and applying machine learning techniques to achieve the power allocation.

References

[1] S. Jiang, "On reliable data transfer in underwater acoustic networks: A survey from networking perspective," *IEEE Commun. Surveys Tuts.*, vol. 20, no. 2, pp. 1036–1055, Jan. 2018.

[2] C. M. Gussen et al., "A survey of underwater wireless communication technologies," *J. Commun. Inf. Sys*, vol. 31, no. 1, pp. 242–255, Oct. 2016.

[3] A. Gkikopouli, G. Nikolakopoulos, and S. Manesis, "A survey on underwater wireless sensor networks and applications," in *Proc. Mediterranean Conference on Control Automation*, Barcelona, Spain, 2012, pp. 1147–1154.

[4] E. Felemban, F. K. Shaikh, U. M. Qureshi, A. A. Sheikh, and S. B. Qaisar, "Underwater sensor network applications: A comprehensive survey," *Int. J. of Distr. Sensor Netw.*, vol. 11, no. 11, pp. 1–14, Nov. 2015.

[5] D. C. Nguyen, M. Ding, P. N. Pathirana, A. Seneviratne, J. Li, D. Niyato, O. A. Dobre, and H. V. Poor, "6G internet of things: A comprehensive survey," *IEEE Internet Things J.*, pp. 1–1, Aug. 2021.

[6] Y. Wang, W. Feng, J. Wang, and T. Q. S. Quek, "Hybrid satellite-UAV-terrestrial networks for 6G ubiquitous coverage: A maritime communications perspective," *IEEE J. Sel. Areas Commun.*, vol. 39, no. 11, pp. 3475–3490, Jun. 2021.

[7] C. D. Alwis, A. Kalla, Q.-V. Pham, P. Kumar, K. Dev, W.-J. Hwang, and M. Liyanage, "Survey on 6G frontiers: Trends, applications, requirements, technologies and future research," *IEEE Open Journal of the Communications Society*, vol. 2, pp. 836–886, Apr. 2021.

[8] M. Jahanbakht, W. Xiang, L. Hanzo, and M. R. Azghadi, "Internet of underwater things and big marine data analytics a comprehensive survey," *IEEE Commun. Surveys Tuts.*, vol. 23, no. 2, pp. 904–956, Jan. 2021.

[9] Y. Li, Y. Zhang, H. Zhou, and T. Jiang, "To relay or not to relay: Open distance and optimal deployment for linear underwater acoustic networks," *IEEE Trans. Commun.*, vol. 66, no. 9, pp. 3797–3808, Sep. 2018.

[10] R. Wang, A. Yadav, E. A. Makled, O. A. Dobre, R. Zhao, and P. K. Varshney, "Optimal power allocation for full-duplex underwater relay networks with energy harvesting: A reinforcement learning approach," *IEEE Commun. Lett.*, vol. 9, no. 2, pp. 223–227, Oct. 2019.

[11] S. M. R. Islam, N. Avazov, O. A. Dobre, and K. Kwak, "Power-domain non-orthogonal multiple access (NOMA) in 5G systems: Potentials and challenges," *IEEE Commun. Surveys Tuts.*, vol. 19, no. 2, pp. 721–742, Oct. 2017.

[12] A. Yadav and O. A. Dobre, "All technologies work together for good: A glance at future mobile networks," *IEEE Trans. Wireless Commun.*, vol. 25, no. 4, pp. 10–16, Aug. 2018.

[13] H. V. Nguyen, V.-D. Nguyen, O. A. Dobre, D. N. Nguyen, E. Dutkiewicz, and O.-S. Shin, "Joint power control and user association for NOMA-based full-duplex systems," *IEEE Trans. Commun.*, vol. 67, no. 11, pp. 8037–8055, Aug. 2019.

[14] Z. Shi, W. Gao, S. Zhang, J. Liu, and N. Kato, "Machine learning-enabled cooperative spectrum sensing for non-orthogonal multiple access," *IEEE Trans. Wireless Commun.*, vol. 19, no. 9, pp. 5692–5702, May 2020.

[15] J. Liu, Z. Shi, S. Zhang, and N. Kato, "Distributed Q-learning aided uplink grant-free noma for massive machine-type communications," *IEEE J. Sel. Areas Commun.*, vol. 39, no. 7, pp. 2029–2041, Jul. 2021.

[16] M. Duarte, C. Dick, and A. Sabharwal, "Experiment-driven characterization of full-duplex wireless systems," *IEEE Trans. Wireless Commun.*, vol. 11, no. 12, pp. 4296–4307, Dec. 2012.

[17] N. Shende, O. Gurbuz, and E. Erkip, "Half-duplex or full-duplex relaying: A capacity analysis under self-interference," in *Proc. Annual Conference on Information Sciences and Systems*, Baltimore, MD, USA, 2013, pp. 1–6.

[18] M. F. Kader, S. Y. Shin, and V. C. M. Leung, "Full-duplex non-orthogonal multiple access in cooperative relay sharing for 5G systems," *IEEE Trans. Veh. Technol.*, vol. 67, no. 7, pp. 5831–5840, Jul. 2018.

[19] M. Zeng, N.-P. Nguyen, O. A. Dobre, Z. Ding, and H. V. Poor, "Spectral- and energy-efficient resource allocation for multi-carrier uplink noma systems," *IEEE Trans. Veh. Technol.*, vol. 68, no. 9, pp. 9293–9296, Jul. 2019.

[20] J. Cheon and H. Cho, "Power allocation scheme for non-orthogonal multiple access in underwater acoustic communications," *Sensors*, vol. 17, no. 11, p. 2465, Oct. 2017.

[21] F. Qu, H. Yang, G. Yu, and L. Yang, "In-band full-duplex communications for underwater acoustic networks," *IEEE Netw.*, vol. 31, no. 5, pp. 59–65, Sept. 2017.

[22] E. A. Makled, A. Yadav, O. A. Dobre, and R. D. Haynes, "Hierarchical full-duplex underwater acoustic network: A NOMA approach," in *Proc. IEEE OCEANS*, Charleston, SC, USA, 2018, pp. 1–6.

[23] A. Yener and S. Ulukus, "Wireless physical-layer security: Lessons learned from information theory," *Proc. IEEE*, vol. 103, no. 10, pp. 1814–1825, Sept. 2015.

[24] F. Jameel, W. U. Khan, Z. Chang, T. Ristaniemi, and J. Liu, "Secrecy analysis and learning-based optimization of cooperative NOMA SWIPT systems," in *Proc. IEEE International Conference on Communications Workshops*, Shanghai, China, 2019, pp. 1–6.

[25] A. Mukherjee, S. A. A. Fakoorian, J. Huang, and A. L. Swindlehurst, "Principles of physical layer security in multiuser wireless networks: A survey," *IEEE Commun. Surveys Tuts.*, vol. 16, no. 3, pp. 1550–1573, Feb. 2014.

[26] P. Qarabaqi and M. Stojanovic, "Statistical characterization and computationally efficient modeling of a class of underwater acoustic communication channels," *IEEE J. Ocean. Eng.*, vol. 38, no. 4, pp. 701–717, Oct. 2013.

[27] M. Stojanovic, "On the relationship between capacity and distance in an underwater acoustic communication channel," *ACM SIGMOBILE Mobile Computing and Communications Review*, vol. 11, no. 4, pp. 34–43, Oct. 2007.

[28] R. Wang, E. A. Makled, A. Yadav, O. A. Dobre, and R. Zhao, "Reinforcement learning-based energy-efficient power allocation for underwater full-duplex relay network with energy harvesting," in *Proc. IEEE Veh. Technol. Conference*, Victoria, BC, Canada, 2020, pp. 1–5.

[29] R. F. Coates, *Underwater Acoustic System*. MacMillan International Higher Education, 1990, ch. 6, pp. 90–100.

[30] A. Yadav, O. A. Dobre, and N. Ansari, "Energy and traffic aware full-duplex communications for 5G systems," *IEEE Access*, vol. 5, pp. 11 278–11 290, Jul. 2017.

[31] C. Canuto and A. Tabacco, *Taylor Expansions and Application*. Milano: Springer Milan, 2008, ch. 7, pp. 223–255.

[32] N. Zaghdoud, A. B. Mnaouer, W. H. Alouane, H. Boujemaa, and F. Touati, "Secure performance analysis for full-duplex cooperative NOMA system in the presence of multiple eavesdroppers," in *Proc. International Wireless Communications and Mobile Computing*, Limassol, Cyprus, 2020, pp. 1719–1725.

[33] Y. Zhang, H.-M. Wang, Q. Yang, and Z. Ding, "Secrecy sum rate maximization in non-orthogonal multiple access," *IEEE Commun. Lett.*, vol. 20, no. 5, pp. 930–933, Mar. 2016.

[34] Evologics. (2012, Jun.) Usbl positioning and communication system s2cr 7/17 usbl product information. Evologics. [Online]. Available: https://goo.gl/SMLFGE

[35] ——. (2016, Sep.) Underwater acoustic communication system s2cr 7/17d product information. datasheet. [Online]. Available: https://goo.gl/2SW6Qn

[36] M. Grant and S. Boyd, "CVX: Matlab software for disciplined convex programming, version 2.1," http://cvxr.com/cvx, mar 2014.

[37] ——, "Graph implementations for nonsmooth convex programs," in *Recent Advances in Learning and Control*, ser. Lecture Notes in Control and Information Sciences, V. Blondel, S. Boyd, and H. Kimura, Eds.   Springer-Verlag Limited, 2008, pp. 95–110.

[38] R. Yao, L. Yao, X. Zuo, N. Qi, Y. Liu, and J. Xu, "Secrecy energy efficiency maximization in a noma system," in *Proc. International Conference on Communication Software and Networks*, Chongqing, China, 2019, pp. 106–110.

[39] L. White and J. Hanson, "An automatic sea state calculator," in *Proc. IEEE Oceans*, vol. 3, Providence, RI, USA, 2000, pp. 1727–1734.

Chapter 4

Detection and Identification of Mobile Network Signals

4.1 Abstract

This chapter presents a method to detect and identify mobile network signals. The method relies on features extracted from the power spectral density of the signals. The performance of the proposed method is evaluated using over-the-air measurements acquired in various cellular bands, in different geographical areas, and in rural and urban settings. Results verify the high detection and identification accuracy of the method.

4.2 Introduction

Intelligent radios can detect and identify radio signals and transmission parameters. There is a rising demand for employing intelligent radios in commercial and military applications, such as cognitive radios, electronic warfare, and spectrum surveillance [1], [2]. An example application is improving the effectiveness of electronic countermeasure (ECM) devices in targeting network threats by transmitting a tailored waveform, rather than a generic one [3]. Automatic signal identification (ASI) is

78

an essential task of such intelligent radios [4], [5]. There are two common types of ASI algorithms: likelihood-based and feature-based [3], [6]. Although the former category provides higher accuracy of identification, the solutions are complex and susceptible to error due to model mismatches, such as frequency offset [7]. Feature-based algorithms are simpler to implement and provide sub-optimal performance [3].

Feature-based algorithms typically require estimation of the noise floor, signal segmentation and setting a detection threshold in order to detect the signals accurately. Some segmentation methods are found in the literature, such as histogram, wavelet and multi-scale product methods [8], [9], [10]. The wavelet and multi-scale product methods are computationally heavy techniques, while the histogram method requires user refinement and changes to its parameters [10]. Detection thresholds are set by the user based on prior knowledge or assumption of the environment [11]. An exception is in [12], where the presence of a signal is detected from the power spectral density (PSD) without estimating the noise floor. Further, in [13] the PSD is converted into a binary image that undergoes morphological operations to estimate the detection threshold. In [14] it is assumed that the PSD contains two distinct groups, namely a noise group and a signal group, with small variance within each group. Based on this assumption, the PSD is split into segments with specific thresholds to guarantee the flatness of each PSD within each segment and enable signal detection. Earlier work [15] used deep learning for signal identification using synthetic data. The proposed algorithm does not rely on synthetic data and does not require training, but rather uses hand-crafted features that are adjusted based on each PSD measurement.

In this context, the contribution of this chapter is as follows:

1. Propose a signal detection algorithm that automatically updates the detection threshold based on the content of the PSD.

2. Propose an identification algorithm that categorizes the signal types based on features extracted from the PSD of the detected signal, including its bandwidth, variance and edge slope.

3. Combine both algorithms to form a novel method that detects the signals and identifies their types without prior knowledge of the environment.

4. Evaluate the performance of the proposed method using over-the-air measurements of different cellular systems, namely global system for mobile communications (GSM), universal mobile telecommunications service (UMTS), and long term evolution (LTE).

5. Validate the detection and identification performance of the method through over-the-air measurements, versus a commercial detection and identification software [16].

The rest of this chapter is organized as follows: Section 4.3 introduces the proposed signal detection and identification method; Section 4.4 provides the experimental setup and results; and Section 4.5 draws conclusions.

4.3 Signal Detection and Identification Method

The method consists of two algorithms: *(A) Signal Detection*, in which the noise floor estimate is automatically updated and the PSD measurement is segmented; *(B) Signal Identification*, in which the signal type in each segment is identified to be either GSM, UMTS or LTE, depending on features such as bandwidth and variance of the PSD.

4.3.1 Signal Detection Algorithm

Let $\mathbf{x} = \{x_1, x_2, \ldots, x_N\}$ represent the measured PSD values, where x_j is the PSD value in dB at frequency bin j and N is the total number of frequency bins. The first step of the detection algorithm is to estimate the detection threshold (Γ). A bin with x_j above Γ is considered to contain a signal. To

estimate Γ, $\mathbf{x}$ is mapped into a 2D binary array $\mathbf{A} = \left[a_{ij}\right]_{100 \times N}$ as follows:

$$
a_{ij} = \begin{cases} 1, & \text{if } i \leq \frac{100\left(x_j - v\right)}{\Upsilon - v}, 1 \leq j \leq N, \\ \\ \\ 0, & \text{otherwise}, \end{cases} \tag{4.1}
$$

where $\Upsilon = \max\limits_{1 \leq j \leq N}\{x_j\}$ and $v = \min\limits_{1 \leq j \leq N}\{x_j\}$. The vector defines $\mathbf{b} = \left[b_j\right]_{1 \times N}$ such that $b_j = \sum_{i=1}^{100} a_{ij}$. A vector $\mathbf{c} = \left[c_j\right]_{1 \times L}$, where $L \leq N$, is formed by sorting the components of vector $\mathbf{b}$ (ascending order) and considering the components with the same value only once.

Based on the relationship between $\mathbf{x}$, $\mathbf{A}$, $\mathbf{b}$, and $\mathbf{c}$, the detection threshold Γ is calculated as

$$
\Gamma = \begin{cases} c_n + G & \text{if } \psi \leq 0.3, \\ \\ c_n, & \text{otherwise}, \end{cases} \tag{4.2}
$$

where c_n is the n-th component of $\mathbf{c}$, $\psi = \frac{\sum_{i=1}^{100} \sum_{j=1}^{N} a_{ij}}{100N}$ is the ratio of ones to the total number of elements in $\mathbf{A}$, which is indicative of the area under the PSD curve, and $G = \frac{P}{3} \times \max\limits_{1 \leq j \leq L}\{c_j\}$ is a guard margin, with

$$
P = \min(\Psi, 0.3). \tag{4.3}
$$

Based on extensive observations, $n = \lceil\rceil PL$ is selected, where $\lceil\rceil$ denotes the ceiling function. ψ has a direct relation with n: the higher the ambient noise, the more 1's will appear in $\mathbf{A}$ to represent the noise.

Using the detection threshold, the PSD of the detected signals $\hat{\mathbf{x}} = \{\hat{x}_1, \hat{x}_2, \ldots, \hat{x}_N\}$ is obtained as

$$
\hat{x}_j = \begin{cases} x_j, & \text{if } b_j \geq \Gamma, \\ \\ v, & \text{otherwise}. \end{cases} \tag{4.4}
$$

Figs 4.1a and 4.1b illustrate a measured PSD and the resulting PSD after subtracting the noise floor using (4.4), respectively. Results are obtained based on over-the-air measurement data. At this point,

81

all the bins that contain signals are detected. A given signal $\hat{s}$ is defined in $\hat{\mathbf{x}}$ as

$$\hat{s} = \{\hat{x}_{k_s+1}, \hat{x}_{k_s+2}, \ldots, \hat{x}_{k_s+J_s}\}, \tag{4.5}$$

such that k_s is the index of the last noise bin before signal $\hat{s}$, $\hat{x}_m > \upsilon \ \forall m \ (k_s + 1 \le m \le k_s + J_s)$, $\hat{x}_{k_s} = \upsilon$ and $\hat{x}_{k_s+J_s+1} = \upsilon$, and J_s is the number of bins in signal $\hat{s}$.

Adjacent signals in $\hat{\mathbf{x}}$ may not be well separated due to a coarse spectral resolution, which affects the identification accuracy. To locate the signal edges, the fluctuation is considered in power within one signal $\hat{s}$ should not exceed 6 dB per bin. When a change in the values of any two adjacent signal bins in $\hat{s}$ is more than 6 dB, this indicates the start of a new signal. Consequently, all successive elements $\hat{x}_j > \alpha$ and $\hat{x}_{j+1} > \alpha \in \hat{s}$, $j = k_s + 1, 2, \ldots, k_s + J_s$, are updated as follows

$$\hat{x}_j = \alpha \text{ if } \hat{x}_{j+1} - \hat{x}_j > 6,$$
$$\hat{x}_{j+1} = \alpha \text{ if } \hat{x}_j - \hat{x}_{j+1} > 6. \tag{4.6}$$

$\hat{s}$ is then updated based on (4.5). Then, a signal s in $\mathbf{x}$ can be defined as:

$$s = \{x_{k_s+1}, x_{k_s+2}, \ldots, x_{k_s+J_s}\}. \tag{4.7}$$

Each signal s is associated with a vector $\mathbf{b}_s = \{b_{k_s+1}, b_{k_s+2}, \ldots, b_{k_s+J_s}\}$. Fig. 4.1c illustrates the resulted PSD after detecting signal edges using (4.6), separated and ready to undergo the type identification algorithm.
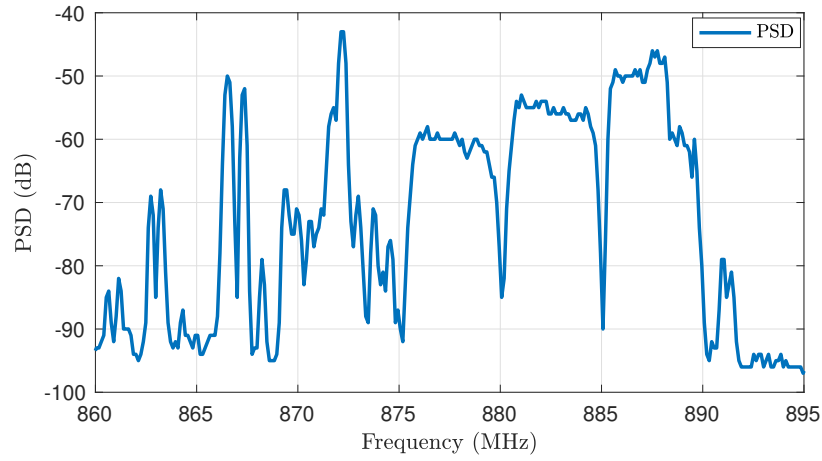
(a) A measured PSD.
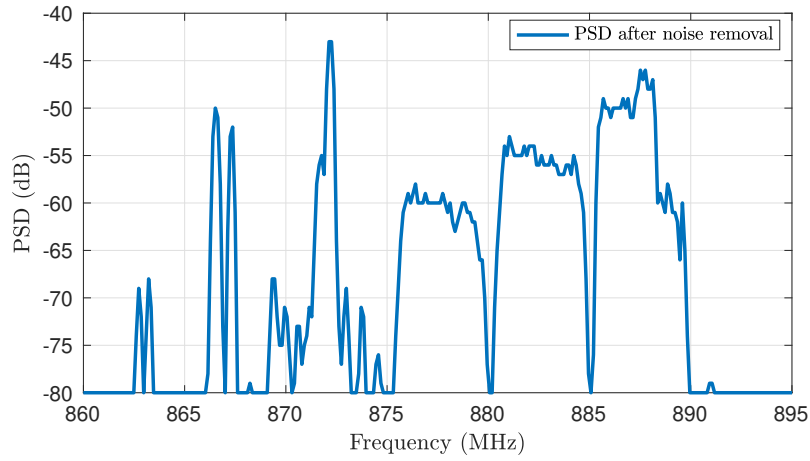
(b) PSD after subtracting the noise floor using (4.4).
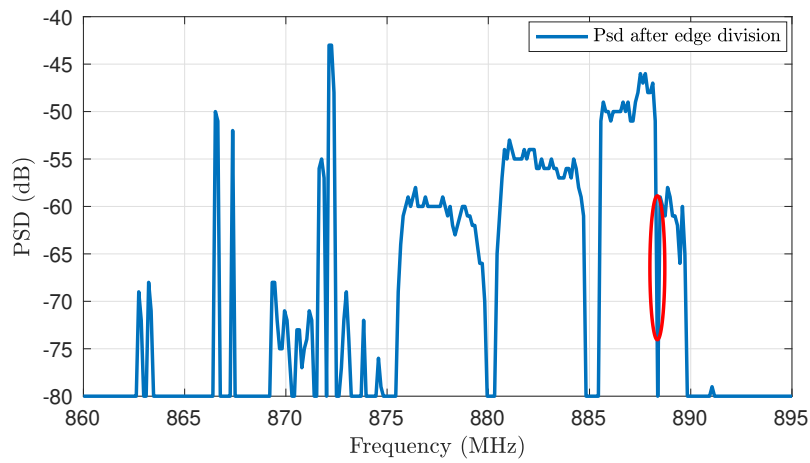
(c) Magnified PSD after edge separation using (4.6).

Figure 4.1: A sample PSD at different stages of the signal detection algorithm, obtained based on over-the-air measurements.

4.3.2   Signal Identification Algorithm

In this algorithm, the signal type (GSM, UMTS or LTE) is identified based on the following features of s: (1) Signal bandwidth (W_s), which can be obtained as

$$W_s = \frac{W}{N} J_s, \tag{4.8}$$

where W is the total observed bandwidth; (2) The variation of the values of the elements in $\mathbf{b}_s$.

4.3.2.1   Stage 1: Differentiating GSM from UMTS/LTE

The bandwidth of a UMTS signal is 5 MHz [17], the bandwidth of an LTE signal can be 1.4, 5, 10, 15, or 20 MHz [18], while the minimum bandwidth of a signal in GSM band is 200 kHz [19]. Hence, if W_s is less than 1.4 MHz, the spectrum segment is identified as a GSM band.

To identify signals with W_s greater than 1.4 MHz, 5,685 PSD readings are examined, containing a total of 28,311 over-the-air captured signals and noticed that the values of the PSDs of GSM signals fluctuate more compared to those of UMTS/LTE signals. Consequently, the variance of the elements in $\mathbf{b}_s$ ($\sigma_{b_s}^2$) is calculated for each signal; Fig. 4.2 illustrates the resulting histogram. In Fig. 4.2, it is clear that $\sigma_{b_s}^2$ for the over-the-air captured GSM signal is generally higher in comparison with that of the over-the-air captured UMTS/LTE signals. However, there is no clear threshold that separates the histograms of the GSM and UMTS/LTE due to the overlap.
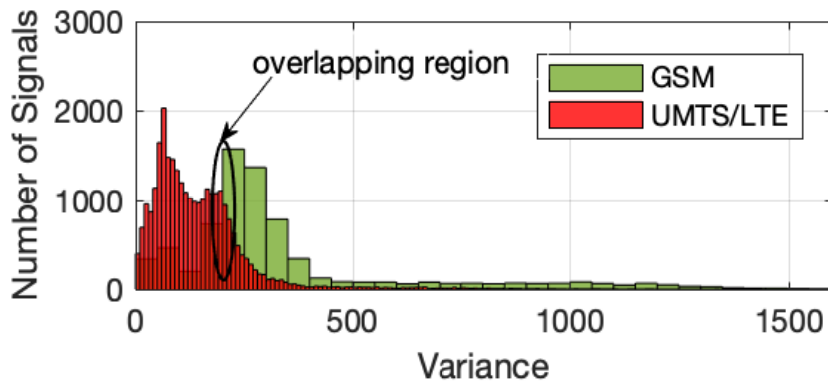
Figure 4.2: Variance of the components of $\mathbf{b}_s$.
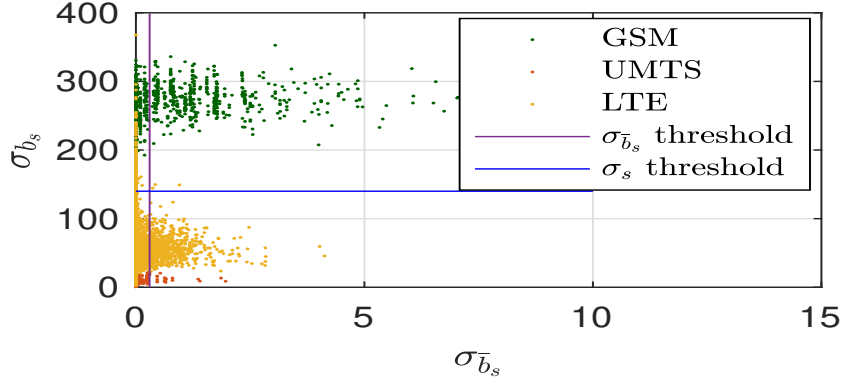
Figure 4.3: Variance of the components of $\bar{\mathbf{b}}_s$ vs. variance of the components of $\mathbf{b}_s$.

To separate the histograms of GSM and UMTS/LTE, a vector $\bar{\mathbf{b}}_s = \{\bar{b}_{k_s+1}, \bar{b}_{k_s+2}, \ldots, \bar{b}_{k_s+J_s}\}$ is obtained for each signal s, such that $\forall k_s + 1 \leq m_s \leq k_s + J_s$.

$$\bar{b}_{m_s} = \begin{cases} b_{m_s}, & \text{if } b_{m_s} \leq \lambda, \\ \\ \lambda, & \text{otherwise,} \end{cases} \quad (4.9)$$

where $\lambda = 0.30 \times \max_{k_s+1 \leq m_s \leq k_s+J_s} \{b_{m_s}\}$. $\sigma_{\bar{b}_s}^2$ is defined as the variance of the elements in $\bar{\mathbf{b}}_s$ and calculate $\sigma_{\bar{b}_s}^2$ of each signal. Fig. 4.3 shows that for signals with $W_s > 1.4$ MHz, most of the over-the-air captured GSM signals have $\sigma_{\bar{b}_s}^2 > 0.3$ and $\sigma_{b_s}^2 > 140$. Consequently, a signal s with W_s greater than 1.4 MHz is identified based on $\sigma_{\bar{b}_s}^2$ and $\sigma_{b_s}^2$. If $\sigma_{\bar{b}_s}^2 > 0.3$ and $\sigma_{b_s}^2 > 140$, s is identified as a GSM signal. Otherwise, s is not a GSM signal and undergoes the next stage.

4.3.2.2 Stage 2: Differentiating LTE from UMTS

If s is not a GSM signal, the signal is either UMTS or LTE. According to [18], the use of LTE bandwidth below 10 MHz is rare. Hence, W_s is used to differentiate between LTE and UMTS, such that if $W_s > 5.5$ MHz, s is identified as an LTE signal; otherwise s is identified as an UMTS signal. The identification algorithm flow chart is shown in Fig. 4.4.
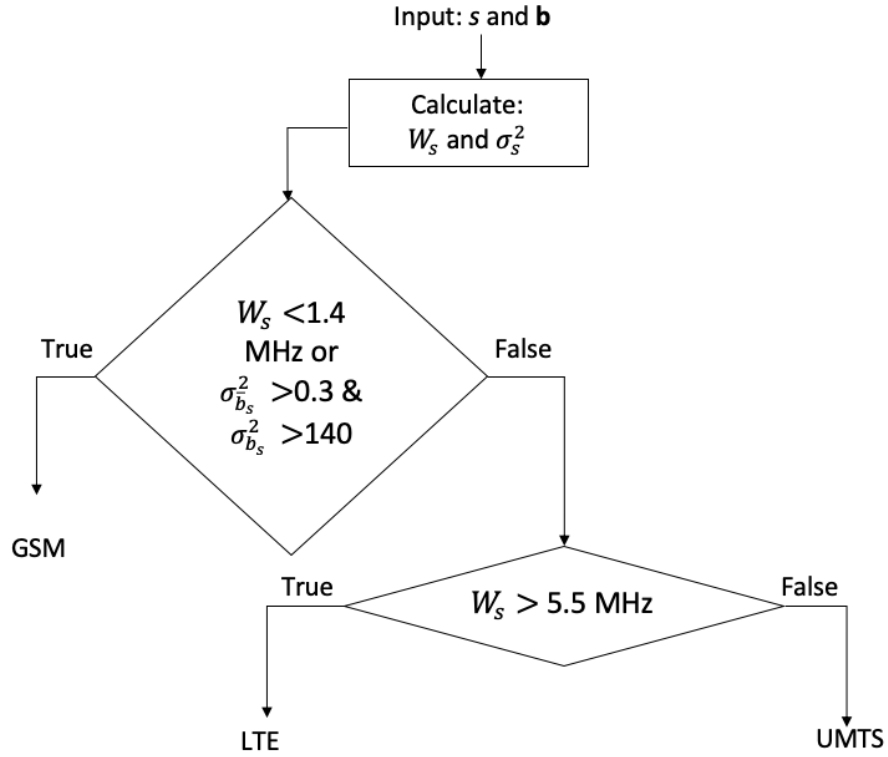
Figure 4.4: Identification algorithm flow chart.

4.3.2.3 Stage 3: Grouping

By this stage, the type of each signal in $\mathbf{x}$ is identified. However, some signals may be over-divided due to (4.4) and (4.6). Consequently, over-divided signals should be grouped. Grouping is done in two steps; small signal re-identification and type-based grouping.

1. Small Signal Re-identification:

   A small signal is defined as a GSM signal with bandwidth below 1.4 MHz or a UMTS/LTE signal with bandwidth below 2.5 MHz. A GSM signal with bandwidth below 1.4 MHz is considered a small signal because of the insufficient number of representative bins of the signal, which inhibits the ability to calculate an accurate variance of the signal. A UMTS or LTE signal with bandwidth below 2.5 MHz is considered a small signal because the smallest possible bandwidth of a UMTS signal is 5 MHz, and in this chapter the smallest considered bandwidth of an LTE is 10 MHz.

   Any three consecutive signals in $\mathbf{x}$ are defined as $s_{(l-1)} = \{x_{k_{s_{(l-1)}}+1}, x_{k_{s_{(l-1)}}+2}, \ldots, x_{k_{s_{(l-1)}}+J_{s_{(l-1)}}}\}$,

$s_l = \{x_{k_{s_l}+1}, x_{k_{s_l}+2}, \ldots, x_{k_{s_l}+J_{s_l}}\}$, and $s_{(l+1)} = \{x_{k_{s_{(l+1)}}+1}, x_{k_{s_{(l+1)}}+2}, \ldots, x_{k_{s_{(l+1)}}+J_{s_{(l+1)}}}\}$. The

separation between $s_{(l-1)}$ and s_l is defined as $\delta^1_{s_l} = \dfrac{\left(k_{s_l}+1-\left(k_{s_{(l-1)}}+J_{s_{(l-1)}}\right)\right)W}{N}$ MHz and the sep-

aration between s_l and s_{l+1} is defined as $\delta^2_{s_l} = \dfrac{\left(k_{s_{(l+1)}}+1-\left(k_{s_l}+J_{s_l}\right)\right)W}{N}$ MHz.

A small signal is considered as s_l , if $\delta^1_{s_l}$ is below 0.2 MHz, and s_{l-1} has a greater bandwidth than

s_l, then s_l is identified with the same type as s_{l-1}. Also, if s_{l-1} and s_{l+1} have the same type and

$\delta^1_{s_l}$ and $\delta^2_{s_l}$ are both below 0.5 MHz, s_l is identified with the same type as the adjacent signals.

Some noise bins have values greater than Γ, which leads to recognizing them as small signals.

In order to avoid false alarms, each signal s with $\sum_{m=k_s}^{k_s+J_s} b_m < 200$ is discarded, where 200 is

double the maximum value at one bin (i.e., $\max\limits_{1 \leq j \leq N} \{b_j\} = 100$).

4.3.2.4 Stage 4: Signal Recovery

The bandwidth of a UMTS signal is 5 MHz, and the bandwidth of a LTE signal is either 10, 15 or

20 MHz. The operations in (4) and (5) may alter the borders of the signals of the UMTS and LTE.

Henceforth, the number of bins of the affected signal are roudn up to obtain a bandwidth as close as

possible to 5, 10, 15 or 20 MHz, without interfering with the neighbouring signals.

Figure 4.5: Illustration of the spectral identification using a commercial drive test software.

4.4 Experimental Setup and Results

A Rohde and Schwartz R&S® TSME drive test scanner was used to capture measurement data [16].

This instrument can measure multiple cellular technologies simultaneously in wireless communications

bands from 350 MHz to 4.4 GHz. The scanner recorded power spectrum readings from several cellular

bands with distinct bandwidths, to assess the efficacy of the method to detect and identify different signals. Recorded data in R&S propriety format was exported into ASCII files to be processed in MATLAB® using the export tool provided with the scanner software.

A 20 MHz instantaneous capture bandwidth was utilized to scan each cellular band. PSD measurements with a frequency resolution of 180 kHz were provided by the measurement device by applying the fast Fourier transform with the size of 128 to time domain signal samples. PSD measurements were processed with the R&S® ROMES software automatic channel detection tool to label the measurement results as a reference for validation [16]. An example of spectrum capture from 1900 MHz band covering the downlink of UMTS, GSM and LTE is shown in Figs 4.5 and 4.6. Fig. 4.5 depicts the labeled output showing spectral identifications of the validation software, while Fig. 4.6 illustrates the spectrum capture, signal detection and type identification of the proposed method for the same band.
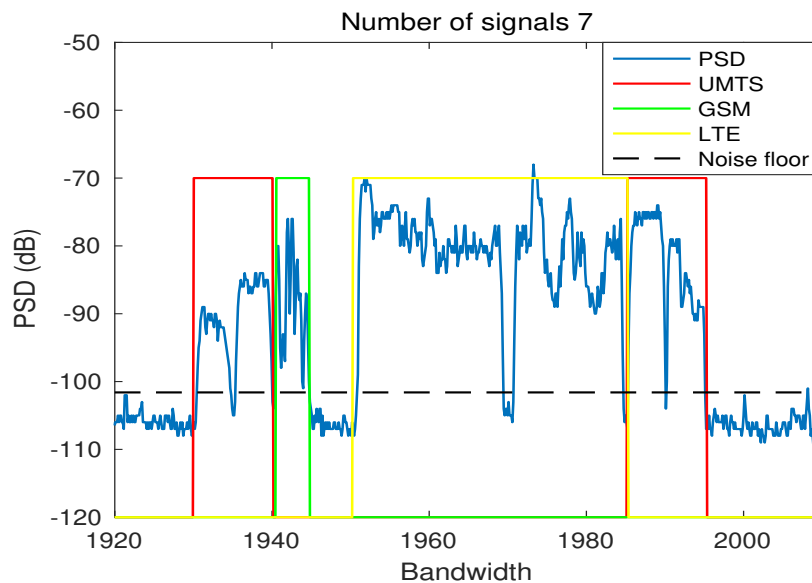
Figure 4.6: The proposed method output.

The proposed algorithm has been evaluated using 10243 real-world PSD measurements captured from three different locations, including both rural and urban settings, and at different times. Table 4.1 illustrates the identification performance of the proposed algorithm at these locations. It is noticed that

the algorithm demonstrates a robust identification performance with identification accuracies above 92%.

Table 4.1: Results of the proposed algorithm.

Location	1	2	3
Number of sites	21	4	1
Number of PSD readings	4395	5786	62
Identification accuracy	93%	92%	98%

The average execution time of the algorithm on a machine with Intel ® Core i7 CPU working at a clock frequency of 1.7 GHz with 8 GB of RAM is 16 ms per PSD reading.

4.5 Conclusion

In this chapter, a method was proposed to detect and identify mobile network signals from their PSD measurements. The method consists of a signal detection and an identification algorithm. The detection algorithm sets a decision threshold automatically without complex operations or human intervention. The identification algorithm relies on spectral shape parameters such as bandwidth and variance of the PSD of each detected signal to classify them as GSM, UMTS or LTE. Proposed algorithms were validated against a commercial automatic channel detection software using data captured from a drive test scanner. The proposed method successfully detected all of the experimental data and accurately identified 92% of the signals.

References

[1] Y. A. Eldemerdash, O. A. Dobre, O. Üreten, and T. Yensen, "Identification of cellular networks for intelligent radio measurements," *IEEE Trans. Instrum. Meas.*, vol. 66, no. 8, pp. 2204–2211, Aug. 2017.

[2] L. De Vito, D. D. Napolitano, S. Rapuano, and M. Villanacci, "Eigenvalue-based signal detector for an automatic modulation classifier," in *Proc. IEEE Int. Instrum. Meas. Technol. Conf. (I2MTC)*, 2010, pp. 1131–1136.

[3] Y. A. Eldemerdash, O. A. Dobre, O. Üreten, and T. Yensen, "Fast and robust identification of GSM and LTE signals," in *Proc. IEEE Int. Instrum. Meas. Technol. Conf. (I2MTC)*, 2017, pp. 1–6.

[4] E. Karami, O. A. Dobre, and N. Adnani, "Identification of GSM and LTE signals using their second-order cyclostationarity," in *Proc. IEEE Int. Instrum. Meas. Technol. Conf. (I2MTC)*, 2015, pp. 1108–1112.

[5] D. Bao, P. Daponte, L. De Vito, and S. Rapuano, "Classification of future aeronautical communication signals," in *Proc. IEEE MetroAeroSpace*, 2014, pp. 570–575.

[6] O. A. Dobre, "Signal identification for emerging intelligent radios: classical problems and new challenges," *IEEE Instrum. Meas. Mag.*, vol. 18, no. 2, pp. 11–18, Apr. 2015.

[7] F. Hameed, O. A. Dobre, and D. C. Popescu, "On the likelihood-based approach to modulation classification," *IEEE Trans. Wireless Commun.*, vol. 8, no. 12, pp. 5884–5892, Dec. 2009.

[8] L. D. Vito, "A review of wideband spectrum sensing methods for cognitive radios," in *Proc. IEEE Int. Instrum. Meas. Technol. Conf.*, 2012, pp. 2257–2262.

[9] L. Angrisani, D. Capriglione, G. Cerro, L. Ferrigno, and G. Miele, "Analysis of different wavelet segmentation methods for frequency-domain energy detection based spectrum sensing," in *Proc. IEEE Int. Instrum. Meas. Technol. Conf. (I2MTC)*, 2017, pp. 1–6.

[10] D. Bao, L. De Vito, and S. Rapuano, "A histogram-based segmentation method for wideband spectrum sensing in cognitive radios," *IEEE Trans. Instrum. Meas.*, vol. 62, no. 7, pp. 1900–1908, July 2013.

[11] F. Patenaud and M. Dufour, "Method and apparatus for noise floor estimation," U.S. Patent 7,340,375, Mar. 4, 2008.

[12] A. A. Al-Habob, E. A. Makled, O. A. Dobre, and O. Üreten, "Blind signal detection in cellular bands," *IEEE Trans. Instrum. Meas.*, vol. 69, no. 3, pp. 657–659, Jan. 2020.

[13] M. J. Ready, M. L. Downey, and L. J. Corbalis, "Automatic noise floor spectrum estimation in the presence of signals," in *Proc. IEEE Asilomar*, vol. 1, 1997, pp. 877–881.

[14] L. Gonzales-Fuentes, K. Barbé, W. Van Moer, and N. Björsell, "Cognitive radios: Discriminant analysis for automatic signal detection in measured power spectra," *IEEE Trans. Instrum. Meas.*, vol. 62, no. 12, pp. 3351–3360, Dec. 2013.

[15] H. Xia, K. Alshathri, V. B. Lawrence, Y.-D. Yao, A. Montalvo, M. Rauchwerk, and R. Cupo, "Cellular signal identification using convolutional neural networks: AWGN and rayleigh fading channels," in *Proc. IEEE Int. Symposium on Dynamic Spectrum Access Networks*, 2019, pp. 1–5.

[16] ROHDE & SCHWARTZ, "R&S® ROMES4 drive test software," Apr. 2021.

[17] T. Ojanpera and R. Prasad, "An overview of air interface multiple access for IMT-2000/UMTS," *IEEE Commun. Mag.*, vol. 36, no. 9, pp. 82–86, April 1998.

[18] "The LTE standard," Signals Research Group-Project commissioned by Ericsson and Qualcomm, Tech. Rep., Apr. 2014. [Online]. Available: https://www.qualcomm.com/media/documents/files/the-lte-standard.pdf

[19] M. Rahnema, "Overview of the GSM system and protocol architecture," *IEEE Commun. Mag.*, vol. 31, no. 4, pp. 92–100, Apr. 1993.

Chapter 5

Identification of Cellular Signal Measurements Using Machine Learning

5.1 Abstract

Spectrum awareness has a plethora of civilian and defense applications, such as spectrum resource management, adaptive transmissions, interference detection, and identification of threat signals. This chapter proposes an identification neural network (INN)-based model that identifies cellular signals from three different radio access technologies, namely global system for mobile communications, universal mobile telecommunications service, and long-term evolution. The proposed INN identifies whether or not the measured power spectral density belongs to a certain cellular signal type. Two data collection approaches (DCAs) are considered; in-band and multiple-band. The over-the-air measurements for the two DCAs show that, with low computational complexity, the proposed INN model provides an identification accuracy between 93% and 100%, with a false alarm rate between 0% and 10%.

5.2 Introduction

The exponential growth in the number of wireless devices has led to rising demands for the limited radio spectrum. Intelligent radios manage the limited available resources to provide the most efficient communication in both commercial and military applications [1]. Intelligent radios require spectrum awareness, where the transmitter gathers knowledge of the surrounding environment to adapt to the environment and transmit accordingly. Automatic signal identification (ASI) is a leading technique to achieve intelligent radios [2], [3]. The two major types of ASI algorithms are likelihood-based and feature-based [1], [4]–[7]. The former is complex and susceptible to error due to model mismatches [3], whereas the latter is simpler and easier to implement at the expense of reduced performance [2].

The works in [8]–[10] investigated the use of traditional machine learning (ML), such as support vector machine, decision tree, and Naïve Bayes algorithm, to identify wireless signals. When trained with diverse and representative data, the ML classification models were more robust to various channel distortions than likelihood-based and feature-based classification techniques. Although ML is more costly and computationally efficient than traditional signal identification techniques, the computational cost and time consumption of ML algorithms are still high [11]. Such complexity prevents the application of ML algorithms to all devices or nodes in the network [12].

Deep learning (DL) is a computational paradigm that encompasses a diverse array of techniques, including deep neural networks (DNNs), reinforcement learning, generative models, transfer learning, unsupervised learning, and others. In the context of this work, DL refers mainly to DNNs, which utilize multi-layered neural networks (NNs) aimed at extracting increasingly representative and concise information from data, frequently achieving this while minimizing computational and time expenditure. DL models need less feature engineering because of the inherent automatic feature extraction. Consequently, DL can provide better solutions than traditional ML algorithms. DL algorithms have been used in earlier signal identification problems, such as identifying ZigBee, WiFi, and Bluetooth based on phase and amplitude data [13]. Other works used in identification are based on features such

as frequency, bandwidth, and power spectral density [14]–[16]. The authors in [12] and [17] used DL to identify the cellular signals based on synthetic raw signals. Previous works have concluded that for synthetic data, the DL models often provide better identification performance than the traditional ML models due to their architecture [4]. To identify cellular signals automatically in real systems, drive test scanners rely on on demodulating/decoding RF signals, which introduces a high latency as detection over multiple channels in a large spectrum is required. To the best of the author's knowledge, this is the first proposed DL framework for identifying cellular networks based on real measurements that can be readily applied to real systems. This chapter proposes an identification neural network (INN) to identify cellular signal types based on real power spectral density (PSD) measurements without the need for demodulation/decoding of the targeted cellular signal. The contribution of this research is summarized as follows:

- Propose an INN model that is based on the PSD of the over-the-air measurements of cellular networks, namely global system for mobile communications (GSM), universal mobile telecommunications service (UMTS), and long term evolution (LTE) system.

- The identification accuracy and false alarm (FA) rate of the proposed INN model are assessed using two different PSD data collection approaches (DCAs): in-band and multiple-band.

- The computational complexity of the proposed INN model for different scenarios is presented.

The chapter is organized as follows: Section 5.3 introduces the system model, Section 5.4 presents the experimental setup, Section 5.5 shows the numerical results, and Section 5.6 concludes the chapter.

5.3   Proposed Signal Identification Model

5.3.1   Model Description

The proposed INN model determines if the PSD measurement of an occupied bandwidth belongs to a target cellular signal type or not. Fig. 5.1 shows the identification process of the proposed model, which

95

includes data preprocessing and the proposed NN structure. The data preprocessing stage consists of PSD-to-2D image mapping and reshaping. The proposed NN consists of an input layer, multiple fully connected feed-forward (FC-FF) NN layers, and an output layer.
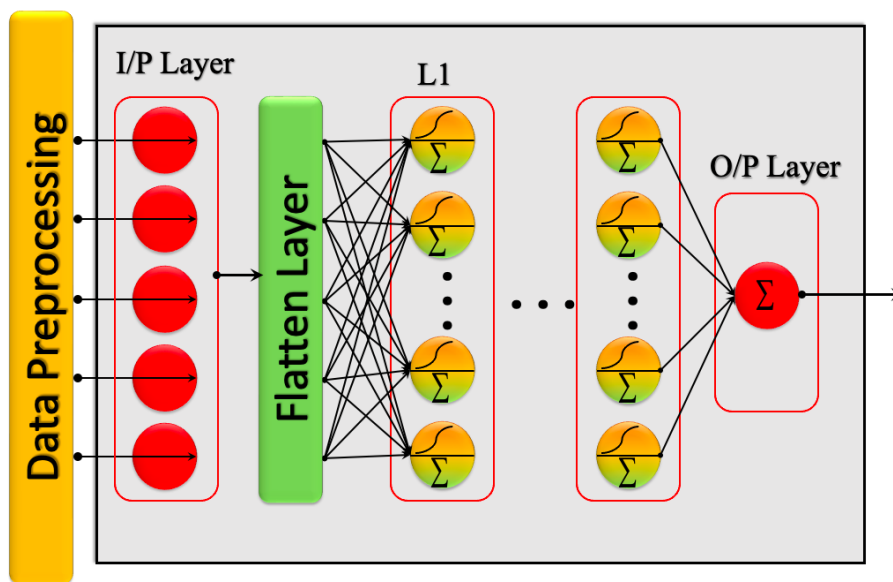
Figure 5.1: Proposed INN model.

PSD-to-2D Image Mapping

Consider that the measured PSD values are represented by $\mathbf{P} = \{p_1, p_2, \ldots, p_F\}$, where p_j is the PSD value in dB at frequency bin j and F is the total number of frequency bins. To build a 2D binary image, $\mathbf{I}$, using the PSD data, the following equation is formulated:

$$\mathbf{I} = \begin{bmatrix} a_{ij} \end{bmatrix}_{H \times T}, a_{ij} = \begin{cases} 1, & \text{if } i = \left\lfloor \frac{100(p_j - \phi)}{\Phi - \phi} \right\rceil, 1 \leq j \leq T, \\ \\ 0, & \text{otherwise}, \end{cases} \tag{5.1}$$

where $\Phi = \max\limits_{1 \leq j \leq T}\{p_j\}$, $\phi = \min\limits_{1 \leq j \leq T}\{p_j\}$, and $\lfloor \cdot \rceil$ approximates a fractional number to the nearest integer. H and T are the number of pixels along the height and width of the image $\mathbf{I}$, respectively. Each

96

I is then divided into its constituent signals, using a signal detection algorithm to determine the signal borders [18].

Reshaping

After obtaining the dataset of the binary images, reshaping is needed to ensure that all input images have the same size. Two reshaping methods are considered: re-sizing (RS) and zero-padding (ZP). In RS, the input image size is scaled up or down to the desired image size, whereas in ZP, the desired image size is achieved by padding the image edges with zeros. The reshaping method is carefully chosen as a hyperparameter.

NN structure

The proposed NN has four different types of layers: an input layer, a flatten layer, multiple FC-FF hidden layers, and an output layer. The input layer receives a 2D binary image, representing the PSD measurement variation over the signal bandwidth, and inputs it to the flatten layer. The frequency bands corresponding to the PSD measurements are not used as an input to the INN model, as a priori knowledge of the spectral allocation cannot be assumed for ad-hoc deployments. The number of neurons of the input layer is the number of pixels of the input image. The flatten layer reshapes the 2D binary image into a 1D vector, then forwards it to the FC-FF hidden layers. The number of FC-FF hidden layers and their sizes vary according to each scenario. Finally, the output layer contains a single neuron that shows whether the input PSD measurement belongs to the target cellular technology or not.

The proposed NN is trained using one cellular signal type, while the testing dataset contains all the cellular signal types that are available in the deployment location.

5.3.2   Complexity Analysis

The complexity of the proposed INN can be measured by three parameters: C_P, C_M, and C_A, denoting the number of weights and biases of the INN, number of real multiplications, and number of real

additions, respectively. Since the proposed INN consists of FC-FF hidden layers, C_P, C_M, and C_A are respectively given as

$$C_P = \sum_{i=1}^{N} (\eta_i + 1)\eta_{i+1}, \tag{5.2}$$

$$C_M = \sum_{i=1}^{N} \eta_i \eta_{i+1}, \tag{5.3}$$

and

$$C_A = \sum_{i=1}^{N} \eta_i \eta_{i+1} + \sum_{i=1}^{N} \eta_{i+1}, \tag{5.4}$$

where η_i and N are the number of neurons in the i-th layer and total number of layers, respectively, that are employed in each scenario. It is worth noting that the cost of each activation function is assumed to be one real addition. Also, the flatten layer shown in Fig. 5.1 is a reshaping layer that does not add a computational cost.

5.4 Measurement Setup

In order to build a reliable NN with a high identification accuracy, the training dataset needs to be accurate, variant, representative, and large enough. This section explains how the data is collected to guarantee such conditions.

The over-the-air measurements were collected through a proprietary software defined radio receiver. Each captured band was band-pass filtered, down-converted to intermediate frequency (IF) and filtered to 100 MHz bandwidth, but did not have the same center frequency. The IF signals were then sampled at 250 MSPS and converted to complex in-phase and quadrature components. 1024-point fast Fourier transforms (FFT) were applied to complex time domain samples in a field-programmable gate array, resulting in about 122 kHz FFT bin size. Magnitude squared FFT values were then averaged over several frames to compose PSD estimates.

The PSDs were captured from the downlink of three different cellular bands: 850 MHz (Band 1), 1900 MHz (Band 2), and 2100 MHz (Band 3). This enhances the diversity in the data as different

cellular bands have various path losses and multi-path delays. The number of PSD measurements for Band 1, Band 2, and Band 3 are 931, 825 and 830, respectively. Typically, the PSD measured from each band contains several cellular signals, as exemplified in Fig. 5.2. The measured cellular signals for each band and their type are categorized as 2493 LTE and 1662 UMTS signals in Band 1; 2793 UMTS and 2793 GSM signals in Band 2; 1652 LTE, 1652 UMTS, and 825 GSM signals in Band 3. In Fig. 5.2, three UMTS channels of 5 MHz each, one 20 MHz LTE channel, one 15 MHz LTE channel and a number of GSM channels are manually marked. Note that the measurement FFT bin size of 122 kHz is not fine enough to resolve individual GSM channels of 200 kHz separation in these PSD captures. Figs. 5.3(a), 5.3(b) and 5.3(c) show samples of the labeled PSD-2D images of GSM, UMTS and LTE, respectively.
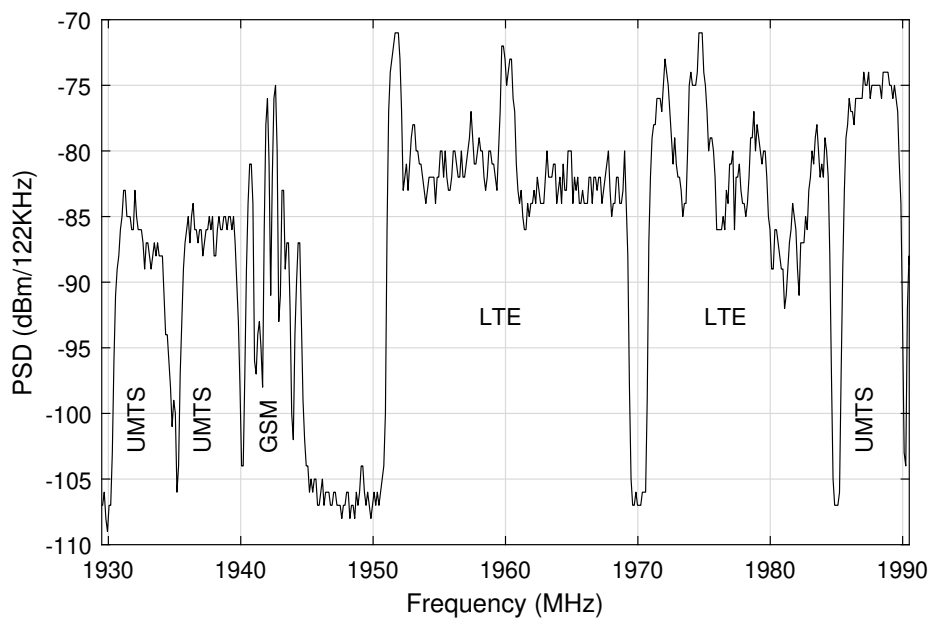
Figure 5.2: Sample PSD measurement.

In order to accurately label the measured PSD data automatically, a Rohde and Schwartz R&S® TSME drive test scanner [18] is used to assess the accuracy of identification of the proposed INN model. This instrument scanned all bands of interest, and the R&S® ROMES4 drive test software automatic channel detection (ACD) tool labeled cellular spectrum as GSM, UMTS or LTE [18].

<div align="center">(a)   (b)   (c)</div>
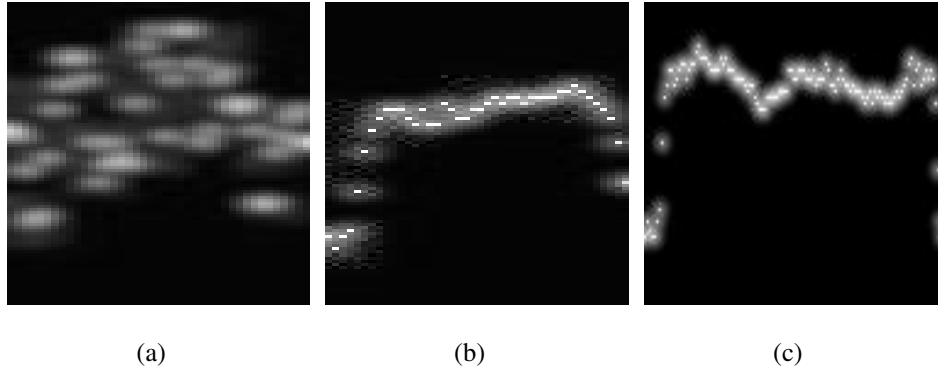
Figure 5.3: PSD to 2-D of (a) GSM (b) UMTS (c) LTE.

5.5 Numerical Results

In this section, the identification performance of the proposed INN model is assessed in terms of identification accuracy and FA rate. The identification accuracy is expressed as the probability of correctly identifying the signal within the target class. An FA happens when the algorithm identifies a PSD measurement as belonging to the target signal type, although it does not. Finally, the output of the proposed INN shows whether the input PSD measurement belongs to the target cellular technology or not. Hence, the output layer contains a single neuron. The training dataset consists of 70% of the PSD captured for each scenario, while the remaining 30% is employed for testing. The reshaping size (i.e., $H \times T$), the number of hidden layers, and their sizes are hyperparameters of the model, which change for each scenario. The hyperparameters used in the proposed INN are as follows: the activation function is *ReLU*, the optimizer is *Adam*, the loss function is *binary cross-entropy*, the learning rate is 0.01, the number of epochs is 5, and the batch size is 100. The hyperparameters were selected based on an exhaustive trial and error search.

Tables 5.1, 5.2 and 5.3 display selected hyperparameters for the proposed INN models corresponding to GSM, LTE and UMTS signals, respectively, and the performance of each INN model based on the identification accuracy and FA rate. The first column depicts the scenario specifications (S), the DCA, either in-band (I) or multiple-band (M), and the scenario number. In the in-band DCA, the training and test datasets are selected from the PSD measurement of one band, whereas in multiple-band

Table 5.1: GSM performance.

S	Band	Layers	L1/L2+	Preprocessing	Accuracy	FA
I,1	1	2	50/50	RS (100×140)	100%	0%
I,2	2	2	50/50	RS (100×140)	100%	0%
M	1& 2	2	100/50	RS (100×200)	97%	3%

Table 5.2: LTE performance.

S	Band	Layers	L1/L2+	Preprocessing	Accuracy	FA
I,1	3	2	100/50	ZP (100×200)	97%	2%
I,2	2	2	50/50	ZP (100×200)	99%	0%
M	2& 3	2	50/200	ZP (200×200)	97%	2%

DCA, training and test data were collected from multiple acquisition bands. The second column represents the band where the measurements were taken. The third column provides the number of NN hidden layers, while the fourth column shows the number of neurons in each hidden layer. The first hidden layer's size is denoted by L1, and all subsequent hidden layers have the same size as L2+. The fifth column presents the selected prepossessing method, whether RS or ZP along with the input image size $(H \times T)$. Finally, the identification accuracy and the FA rate performances are provided in the last two columns.

Table 5.1 shows that the proposed INN model identifies the GSM signals in Band 1 (850 MHz) and Band 2 (1900 MHz) perfectly under in-band DCA. In the multiple-band DCA, a high accuracy of nearly 97% and a low FA rate of 3% are achieved.

Table 5.2 depicts that the INN model provides a high identification accuracy of the LTE signals (i.e., between 97% and 99%), with low FA rates between 0% and 2%.

Table 5.3: UMTS performance.

S	Band	Layers	L1/L2+	Preprocessing	Accuracy	FA
I,1	3	3	100/50	RS (100×140)	98%	4%
I,2	1	2	50/50	ZP (100×100)	100%	0%
I,3	2	3	500/50	RS (300×50)	99%	0%
M	$1, 2 \& 3$	5	50/50	RS (300×50)	93%	10%

The UMTS technology is used in all three bands of interest. Table 5.3 shows that the identification accuracy of the proposed INN is high when the in-band datasets are used. UMTS signal identification performance degrades slightly in multiple-band DCA cases, e.g., an accuracy of 97% and FA rate of 10%. This could be attributed to a more significant change in the RF propagation characteristics over three bands (850 MHz, 1900 MHz, 2100 MHz), indicating the need for a more extensive training dataset from these bands.

Figs. 5.4 and 5.5 present the accuracy and the FA rate of the GSM, LTE, and UMTS signal identification side-by-side, respectively. As summarized in Fig. 5.4, the proposed INN model identifies the three cellular signals with an accuracy between 93% and 100%. Moreover, Fig. 5.5 shows that the proposed INN model provides a low FA rate for the studied scenarios, with the maximum FA rate of about 10% for the multiple-band DCA while targeting UMTS.

Fig. 5.6 illustrates the complexity comparison of the ten studied scenarios, in terms of C_P, C_A, and C_M in (2)-(4) after plugging the parameters of each scenario mentioned in Tables I-III. From this figure, it is seen that the UMTS scenario I,3 has the highest complexity due to its corresponding INN parameters. In particular, in comparison to other INNs, the INN for the UMTS scenario I,3 has a significantly higher number of neurons in its first hidden layer (500 vs. 50 and 100 neurons). The varying propagation characteristics resulting from the existence of UMTS signals in all three bands, required a larger number of neurons, to achieve the needed identification accuracy. It is worth noting that the proposed INN model may need a hyperparameter retuning to identify 5G cellular signals.
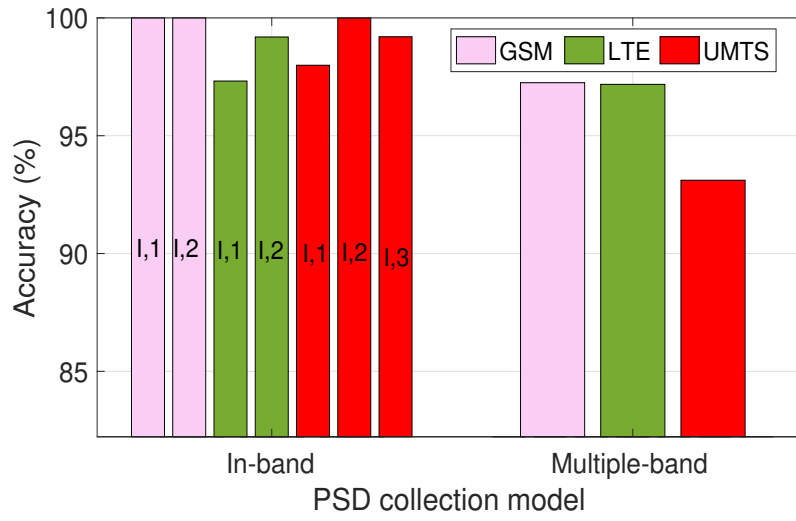
Figure 5.4: Identification accuracy comparison.
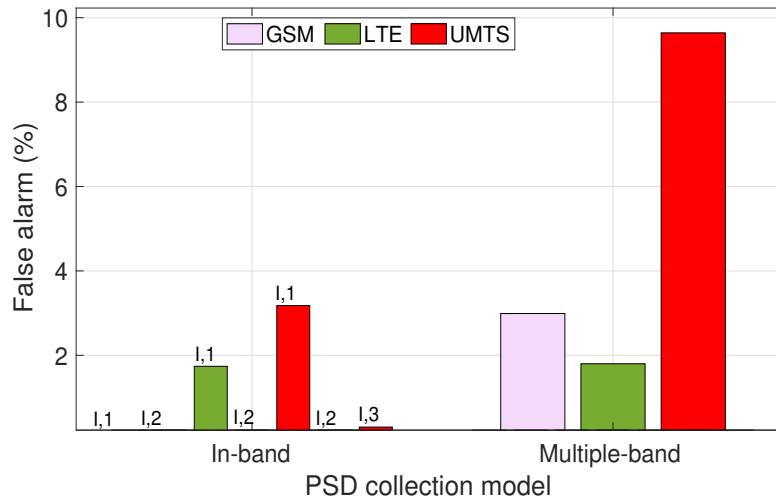
Figure 5.5: FA rate comparison.
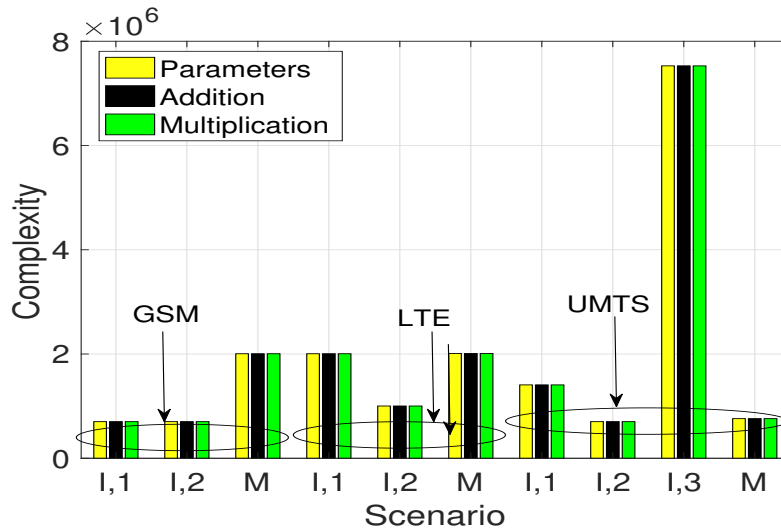
Figure 5.6: Complexity comparison.

5.6 Conclusion

This chapter proposed an INN model that can be appropriately adapted to identify the GSM, UMTS, or LTE cellular signals. The performance of the proposed INN model was assessed in terms of identification accuracy, FA rate, and complexity using two DCAs of the measurements, i.e., in-band and multiple-band. For the in-band DCA, the proposed INN identified the predetermined cellular signal type with a minimum of 97% accuracy and a maximum of 4% FA rate. For the multiple-band DCA, the identification accuracy of both GSM and LTE was around 97%, while the FA rates were below 3%. For the UMTS, the identification accuracy was 93%, and the FA rate was 10%. Hence, the proposed INN successfully identified the cellular signals when trained with both in-band and multiple-band datasets. Most of the scenarios had comparable low complexity. The most complex scenario occured when the three signal types coexisted in the same band. Such an arrangement required a larger NN to learn the changes in the dataset containing the three technologies. Future work will include exploring other NN models, multiple-class identification, and identifying other cellular signal types, including 5G signals.

References

[1] Y. A. Eldemerdash, O. A. Dobre, O. Üreten, and T. Yensen, "Identification of cellular networks for intelligent radio measurements," *IEEE Trans. Instrum. Meas.*, vol. 66, no. 8, pp. 2204–2211, Aug. 2017.

[2] ——, "Fast and robust identification of GSM and LTE signals," in *Proc. IEEE Int. Instrum. Meas. Technol. Conf.*, 2017, pp. 1–6.

[3] F. Hameed, O. A. Dobre, and D. C. Popescu, "On the likelihood-based approach to modulation classification," *IEEE Trans. Wireless Commun.*, vol. 8, no. 12, pp. 5884–5892, Dec. 2009.

[4] E. Karami, O. A. Dobre, and N. Adnani, "Identification of GSM and LTE signals using their second-order cyclostationarity," in *Proc. IEEE Int. Instrum. Meas. Technol. Conf.*, 2015, pp. 1108–1112.

[5] O. A. Dobre, "Signal identification for emerging intelligent radios: classical problems and new challenges," *IEEE Instrum. Meas. Mag.*, vol. 18, no. 2, pp. 11–18, Apr. 2015.

[6] E. A. Makled, A. A. Al-Habob, O. A. Dobre, and O. Üreten, "Detection and identification of mobile network signals," *IEEE Trans. Instrum. Meas.*, vol. 70, pp. 1–4, Sep. 2021.

[7] D. Grimaldi, S. Rapuano, and L. De Vito, "An automatic digital modulation classifier for measurement on telecommunication networks," *IEEE Trans. Instrum. Meas.*, vol. 56, no. 5, pp. 1711–1720, Oct. 2007.

[8] H. Agirman-Tosun, Y. Liu, A. Haimovich, O. Simeone, W. Su, J. Dabin, and E. Kanterakis, "Modulation classification of MIMO-OFDM signals by independent component analysis and support vector machines," in *Proc. Conf. Record of the Forty Fifth Asilomar Conf. on Signals, Systems and Computers*, 2011, pp. 1903–1907.

[9] F. Xing, D. Xu, W. Xu, and H. Wang, "A modulation recognition algorithm of communication signals and implementation based on digital signal processor," in *Proc. IEEE MTT-S Int. Wireless Symp.*, 2021, pp. 1–3.

[10] M. D. Wong, S. K. Ting, and A. K. Nandi, "Naive Bayes classification of adaptive broadband wireless modulation schemes with higher order cumulants," in *Proc. 2nd Int. Conf. on Signal Process. and Commun. Syst.*, 2008, pp. 1–5.

[11] X. Li, F. Dong, S. Zhang, and W. Guo, "A survey on deep learning techniques in wireless signal recognition," *Wireless Communications and Mobile Computing*, vol. 2019, pp. 1–12, Feb. 2019.

[12] H. X. et. al, "Cellular signal identification using convolutional neural networks: AWGN and Rayleigh fading channels," in *Proc. IEEE Int. Symp. on Dynamic Spectrum Access Networks*, 2019, pp. 1–5.

[13] M. Kulin, T. Kazaz, I. Moerman, and E. De Poorter, "End-to-end learning from spectrum data: A deep learning approach for wireless signal identification in spectrum monitoring applications," *IEEE Access*, vol. 6, pp. 18 484–18 501, Mar. 2018.

[14] K. Ahmad, U. Meier, and H. Kwasnicka, "Fuzzy logic based signal classification with cognitive radios for standard wireless technologies," in *Proc. IEEE Int. Conf. on Cognitive Radio Oriented Wireless Networks and Commun.*, 2010, pp. 1–5.

[15] K. Ahmad, G. Shresta, U. Meier, and H. Kwasnicka, "Neuro-fuzzy signal classifier (NFSC) for standard wireless technologies," in *Proc. IEEE Int. Symp. on Wireless Commun. Syst.*, 2010, pp. 616–620.

[16] M. Schmidt, D. Block, and U. Meier, "Wireless interference identification with convolutional neural networks," in *Proc. IEEE Conf. on Industrial Informatics*, 2017, pp. 180–185.

[17] K. Alshathri, H. Xia, V. Lawrence, and Y.-D. Yao, "Cellular system identification using deep learning: GSM, UMTS and LTE," in *Proc. 28th Wireless and Optical Commun. Conf.*, 2019, pp. 1–4.

[18] Rohde & Schwartz, "R&S® ROMES4 drive test software," Apr. 2021.

Chapter 6

Identification of Cellular Measurements: A Neural Network Approach

6.1 Abstract

The efficient utilization of the wireless spectrum is essential to fulfill the rising demand of scarce bandwidth resources. Identifying the cellular signal types occupying the spectrum allows for usage optimization. Neural networks (NNs) are a promising approach for the signal identification problems. This chapter proposes a hybrid convolutional and feedforward NN (HCFNN) that classifies the cellular signals from the power spectral density (PSD) of real measurements into their corresponding types: global system for mobile communications, universal mobile telecommunications service, and long-term evolution. The measured dataset is collected based on two acquisition modes: multiple-band and in-band PSD acquisition modes. In the multiple-band model, the data is collected, trained and tested from various frequency bands, while in the in-band model, the data is collected, trained and tested from a single frequency band. The accuracy and the precision-recall metrics are used to evaluate the performance of the proposed HCFNN model. Moreover, the complexity analysis of the model is derived in terms of the number of real additions, real multiplications, and parameters. The extensive assessments of

the over-the-air measurements show that the proposed HCFNN model accurately identifies the cellular signal types in all studied scenarios.

6.2   Introduction

The introduction of the Internet of Things has boosted the demand on wireless devices over the past years. Such growth creates an increased demand on the limited spectrum. Therefore, a need emerges to utilize the spectrum efficiently by capitalizing on intelligent radio technologies. Intelligent radios are used across civil and military applications [1], [2]. One of the pivotal pillars of intelligent radios is spectrum awareness, in which the transmitter gathers information from the environment to adjust its transmission accordingly. One of the tools of spectrum awareness is automatic signal identification (ASI) [3]. Traditional ASI methods are based on either likelihood calculations or feature assessments [2], [4], [5]. Likelihood-based ASI is cost inefficient, but susceptible to error due to possible mismatches [6]. Feature-based ASI is faster, simpler, and more accessible; however, its performance is sub-optimal compared to the likelihood-based methods.

Earlier research explored the application of machine learning (ML) in wireless signal identification to identify wireless signals to overcome the limitations associated with traditional ASI methods [7]– [15]. It was proven that when trained with diverse and representative datasets, the ML-based methods are more robust and resilient to dynamic channel conditions than traditional ASI methods. Although the traditional ML methods are more efficient than traditional ASI ones, their cost and time consumption are not adequate to be executed by all devices or nodes in a network for large datasets, especially by simpler nodes like handheld devices or sensors [16], [17]. In addition, the performance of the traditional ML-based algorithms varies heavily based on the selected features and dataset. Hence, the traditional ML methods depend on expert knowledge to extract the relevant features, as well as on the proper size of the dataset.

Deep neural networks (DNNs) have been proposed to overcome the limitations of the traditional

109

ML-based algorithms. DNNs are based on layering multiple shallow NNs together to enable the extraction of more representative and concise information at efficient complexity and time costs. Moreover, sometimes the DNN models do not require feature engineering because of the inherent automatic feature extraction [3]. Earlier works used DNNs in signal identification problems [18]–[23]. Some investigated the identification of cellular signals based on features such as frequency, bandwidth, and power spectral density (PSD) [18]–[20]. In [21], DNN was used to classify whether a signal belongs to a certain cellular technology or not. The works in [22], [23] used a deep convolutional NN (DCNN) to identify the cellular signals based on a synthetic raw dataset. In the DCNN, multiple convolutional layers are stacked to form the model. A convolutional layer processes the input as regions instead of processing it as a whole. These regions are employed to extract the essential features used to discriminate between different classes. This reduces the size of the input dimension and hence simplifies the processing.

The global system for mobile communications (GSM), universal mobile telecommunications service (UMTS), and long-term evolution (LTE) are major mobile communication technologies that have significantly influenced cellular networks. GSM, the pioneering digital standard, operates at frequencies such as 900 MHz and 1800 MHz in Europe, Africa, and Asia, and 850 MHz and 1900 MHz in North and South America. UMTS, also known as 3G, offers higher data rates and operates in the 700-2600 MHz frequency range. LTE, the 4G successor, achieves even higher data rates using various frequency bands, including 700 MHz, 1800 MHz, 1900 MHz, 2100 MHz, and 2600 MHz.

In this chapter, a hybrid convolutional feedforward NN (HCFNN) is proposed to classify GSM, UMTS, and LTE cellular signals measured over-the-air in diverse frequency bands. Two PSD acquisition modes for the measured datasets are considered; multiple-band (MB) and in-band (IB) acquisition modes. The MB-PSD model is trained, and tested over measurements from various frequency bands, whereas the IB-PSD model is trained and tested over measurements from a single frequency band. The proposed HCFNN models of the two studied acquisition modes (i.e., MB-PSD and IB-PSD) are assessed and compared in terms of identification accuracy, and precision-recall (PR) metrics. The con-

tributions of this chapter are as follows:

1. Introduce a mapper that extracts the signal images from the PSD of the measured dataset.

2. Propose a DNN model (i.e., HCFNN model) to identify over-the-air measurements based on the PSD signal images into one of three classes (i.e, GSM, UMTS, or LTE).

3. Propose two PSD acquisition modes (i.e., MB-PSD and IB-PSD) to study the proposed HCFNN model.

4. Assess the accuracy of the HCFNN model in identifying cellular PSD measurements using real measurements, evaluating both identification accuracy and PR metrics. The numerical results demonstrate that the proposed model effectively identifies all cellular PSD measurements in the two examined acquisition modes.

5. Derive and discuss the complexity of the proposed HCFNN model in terms of the number of real additions, multiplications, and parameters that are required to identify the cellular signal types.

6. Compare the identification performance and complexity cost of the proposed HCFNN model with other DNN structures, and traditional ASI methods, to verify the superiority of the proposed HCFNN model.

The remainder of this chapter is organized as follows: Section 6.3 introduces the proposed signal identification model, and Section 6.4 analyzes its complexity. The experimental setup and numerical results are discussed in Section 6.5, and Section 6.6 concludes the chapter.

6.3 Proposed Signal Identification Model

The proposed HCFNN model aims to identify the cellular signals based on over-the-air PSD measurements. The model, shown in Fig. 6.1, encompasses multiple stages: PSD acquisition, PSD/two-
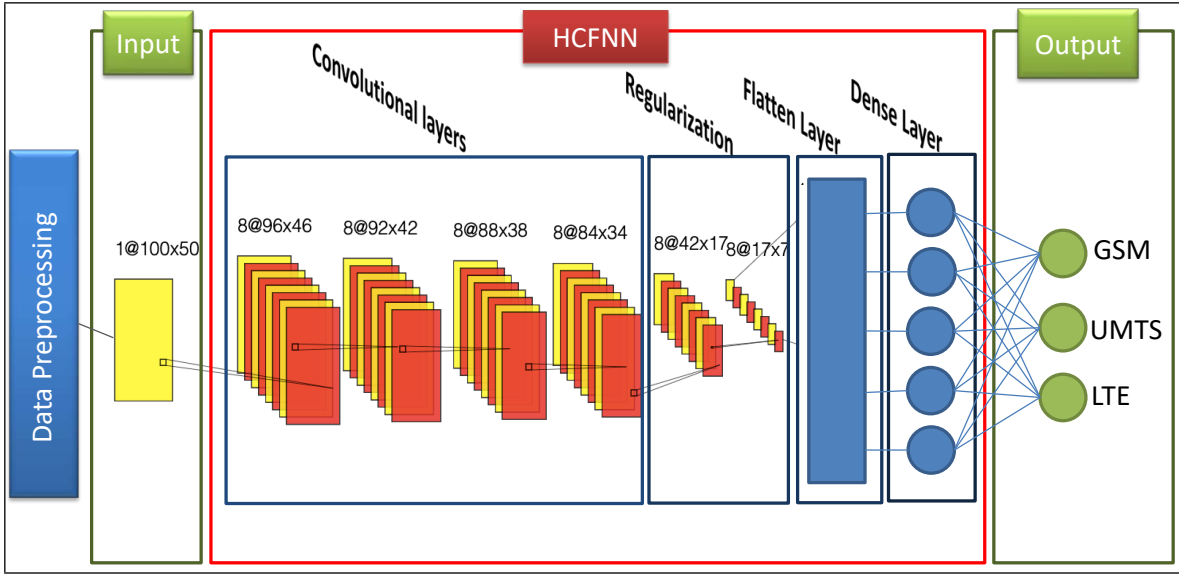
Fig. 6.1: Proposed HCFNN model.

dimensional (2D) image mapper, data preprocessing, and the proposed DNN structure. Each block of the proposed HCFNN model in Fig. 6.1 is explained in detail in the following subsections.

6.3.1 PSD Acquisition

Over-the-air PSD measurements are collected from diverse frequency bands. Samples of the measured PSD are shown in Fig. 6.2. The PSD measurements are represented as $\mathbf{P} = p_1, p_2, \ldots, p_T$, where T denotes the total number of frequency bins and p_t represents the PSD value in dB at frequency bin t. The images of signals are acquired by one of the two acquisition modes, namely MB-PSD or IB-PSD.

6.3.1.1 MB-PSD Acquisition

In MB-PSD, the dataset is gathered from all the frequency bands to train the proposed HCFNN model. Hence, to build a model using the MB-PSD acquisition mode, readings are collected from all bands to be used for training and testing. Within Fig. 6.2a, a representative subset of the MB-PSD dataset is presented, showcasing three samples sourced from individual spectral bands. The comprehensive dataset encompasses all information gleaned across all different spectral bands, serving as the primary
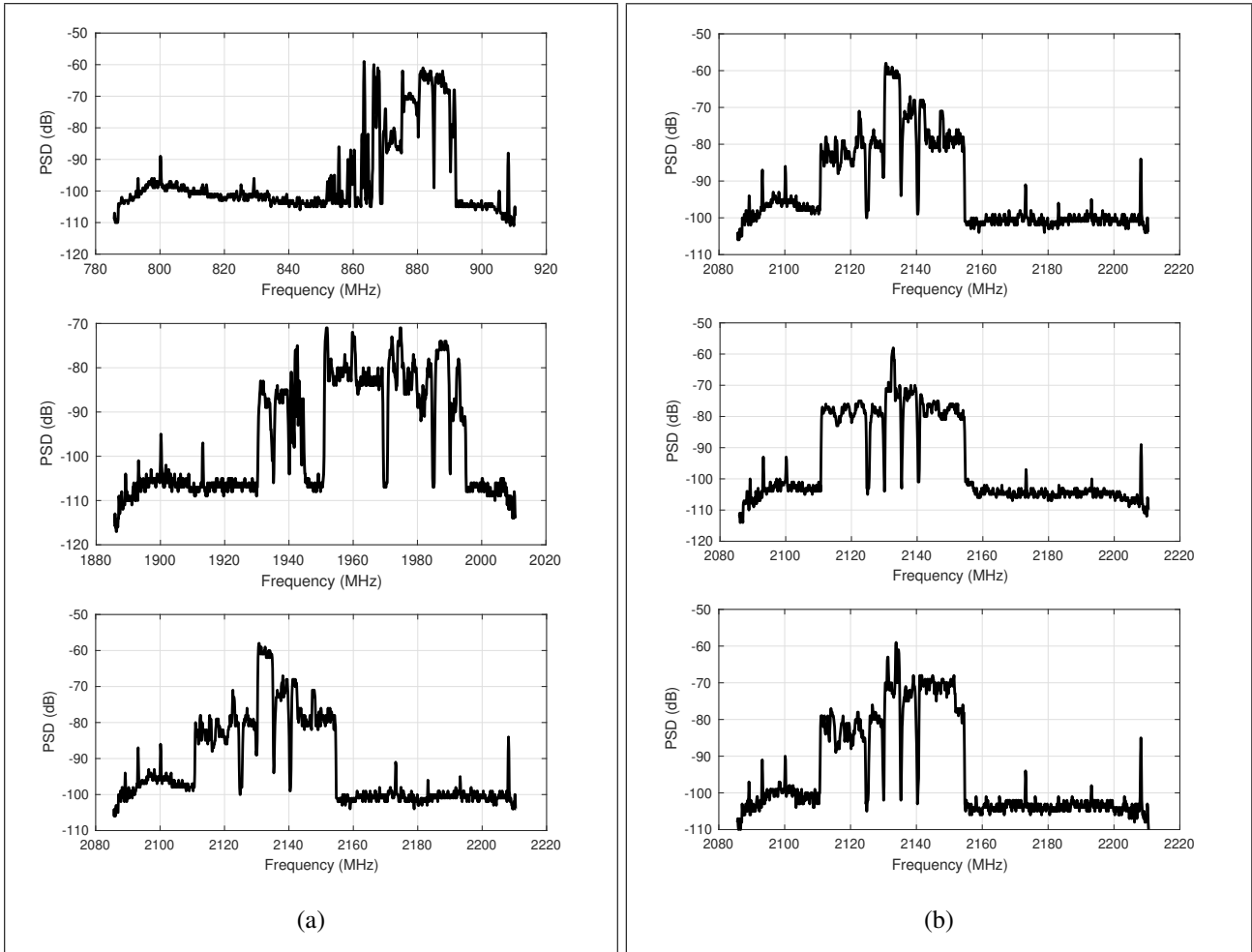
Fig. 6.2: Data collection sample (a) MB-PSD (b) IB-PSD.

corpus for training and testing the proposed HCFNN model. The well-trained HCFNN is used to identify cellular signals from any of the frequency bands in the assembly. The proposed HCFNN identification performance is tested using a dataset with measurements from all frequency bands.

6.3.1.2   IB-PSD Acquisition

In the context of IB-PSD, data extracted from each distinct frequency band serves as the basis for training and testing the proposed HCFNN model tailored to that specific frequency band. Consequently, the process of model construction for a given frequency band exclusively relies on the PSD measurements collected from that particular band alone. Fig. 6.2b presents an illustrative excerpt from the acquired dataset of the IB-PSD at the frequency band of 2100 MHz. The graphical representation therein delineates different measurements obtained from the 2100 MHz band, serving as representative samples for the broader set of measurements to be employed in both training and testing the proposed HCFNN in the 2100 MHz band. Hence, this approach inherently entails the development of individualized HCFNNs for each frequency band, characterized by their unique weights and biases.

6.3.2   PSD/2D-Image Mapper

In this stage, the PSD measured values are converted to a 2-D binary image with the dimensions of 100 by 1024 that encapsulates all the data in a single PSD measurement, $\mathbf{G}_d$. In $\mathbf{G}_d$, all pixels are assigned a value of zero (denoting black pixels), except for the points corresponding to the value of the PSD curve at the calibrated scale, which are assigned the value of one (denoted by white pixels). $\mathbf{G}_d$ is computed using the equation below:

$$\mathbf{G}_d = \begin{bmatrix} a_{ty} \end{bmatrix}_{H \times T}, \tag{6.1}$$

where a_{ty} is given by

$$a_{ty} = \begin{cases} 1, & \text{if } y = \left\lfloor \frac{H(p_t - \phi_d)}{\Phi_d - \phi_d} \right\rceil, 1 \leq t \leq T, \\ \\ \\ 0, & \text{otherwise,} \end{cases} \tag{6.2}$$

where d ranges from 1 to the number of acquired PSD measurements. H is the image height, assumed to be 100, and the image width is equal to T for all $\mathbf{G}_d$. Here, p_t is the PSD value at bin t. Φ_d and ϕ_d are the maximum and minimum measurement of the d-th PSD represented as $\Phi_d = \max\limits_{1 \leq t \leq T} \{p_t\}$ and $\phi_d = \min\limits_{1 \leq t \leq T} \{p_t\}$, respectively, and $\lfloor \cdot \rceil$ approximates the fractional number to the nearest integer value.

6.3.3 Data Preprocessing

Each $\mathbf{G}_d$ is segmented into S_d windows. S_d denotes the number of signals occupying the d-th PSD measurement. Each window, $\mathbf{G}_s$, is a binary image of a single signal with a height H_s and width T_s. The boundaries of each $\mathbf{G}_s$ are estimated by a commercial software that determines the frequency band occupancy. $\mathbf{G}_s$ is defined as

$$\mathbf{G}_s = \left[\dot{a}_{ty} \right]_{H_s \times T_s}, \tag{6.3}$$

with

$$\dot{a}_{ty} = \begin{cases} 1, & \text{if } y = \left\lfloor \frac{H(p_t - \phi_d)}{\Phi_d - \phi_d} \right\rceil, f_{st} \leq t \leq f_e, \\ \\ \\ 0, & \text{otherwise,} \end{cases} \tag{6.4}$$

where H_s, is the height of the window that has the same value as the image height H, while f_{st} and f_e are the start and end frequency bins of the signal s. Each $\mathbf{G}_s$ has its unique image width, N_s, based on its bandwidth occupancy, in which $\sum_{s=1}^{s=S_d} T_s \leq T$. Fig. 6.3 illustrates samples $\mathbf{G}_s$, for UMTS, GSM and LTE.

It is important to note that the frequency bands associated with the PSD measurements do not qualify as inputs for the DNN model because ad-hoc deployments cannot presume prior knowledge of

<div align="center">(a)   (b)   (c)</div>
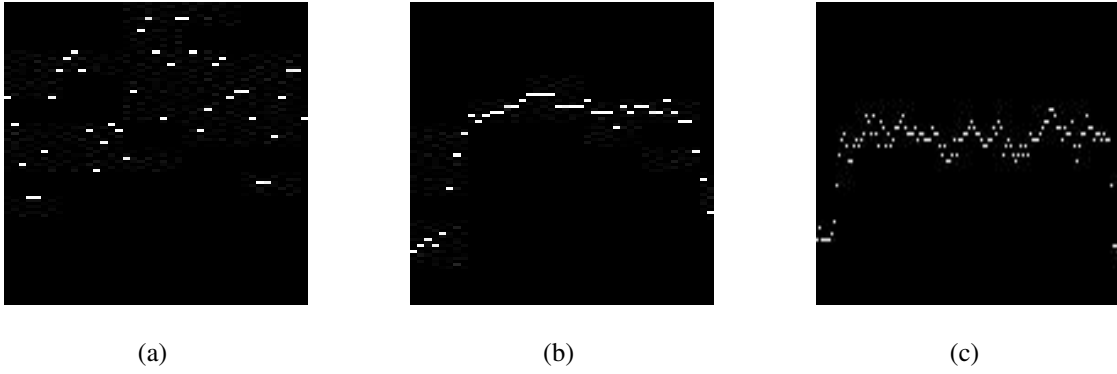
Fig. 6.3: Samples of $\mathbf{G}_s$ (a) GSM (b) UMTS (c) LTE.

spectral allocation.

Since the dimensions of all $\mathbf{G}_s$ need to be standardized, the $\mathbf{G}_s$ images are resized to the same height and width of H_{in} and T_{in}, respectively. The resizing can up-scale or down-scale $\mathbf{G}_s$ to match the required dimensions, using bicubic interpolation. Since H_{in} and T_{in} affect the computational complexity and identification accuracy of the proposed HCFNN model, they are considered as hyperparameters that are properly tuned to enhance the identification accuracy and optimize the computational complexity of the proposed HCFNN model.

6.3.4 Proposed HCFNN Model

DNNs in general are universal approximators composed of several hidden layers between the input and output layers. The DNN approximates any function, $v = g(u)$, to map the input $u \in \mathbb{R}^m$ to the output $v \in \mathbb{R}^n$, where $\mathbb{R}^m$ and $\mathbb{R}^n$ represent two distinct spaces of real numbers. By applying a cascade of Ω non-linear transformations, Z, on the input u, a DNN approximates v as [24]

$$v \approx Z_\Omega(Z_{(\Omega-1)}(...Z_1(u;\theta_1);\theta_Z)), \tag{6.5}$$

with

$$Z_\omega(u;\theta_\omega) \triangleq A_\omega(\mathbf{W}_\omega u + b_\omega)\omega = 1,.....\Omega, \tag{6.6}$$

where $\theta_\omega \triangleq (\mathbf{W}_\omega, b_\omega)$ is a set of the DNN parameters, with $\mathbf{W}_\omega$ and b_ω as the set of weights and biases, respectively, and A_ω denotes the activation function. The weights and biases are learned through the

<div align="center">116</div>

training dataset using a sample set of the data with known labels [24].

In this work, a hybrid between convolutional and feedforward layers is used, namely the HCFNN model. The proposed HCFNN model, shown in Fig. 6.1, has a 2D input image with a height of H_{in} and width of T_{in}, followed by four hidden convolutional layers. To regularize the output of these layers and avoid overfitting, maxpooling and dropout layers are added. A flatten layer is then used to convert the 2D matrix into a 1D array to fit the feedforward layer. Lastly, a fully connected dense (i.e., feedforward) hidden layer after the flatten layer adds another degree of freedom to compromise between the model identification performance and computational complexity. A final dense output layer is used to classify the output into one of the three classes (i.e., UMTS, LTE or GSM). The details of each type of layer are discussed below.

6.3.4.1   Convolutional Layer

The convolutional layer employs a set of filters, each of which scans the input image to identify particular features, such as edges or textures. The filters are applied via the convolution process, which entails multiplying each filter element by a corresponding element in the input image, summing the results, and producing a single output value.

In this procedure, the convolutional layer employs shared weights, meaning that the same set of weights is applied to each input pixel location. Each filter examines only a small portion of the input image at a time due to the layer's use of local connections. This method assists the convolutional layer in efficiently capturing the spatial features of the input image, while simultaneously reducing the number of NN parameters [25]. Hence, it eliminates the need for manual feature engineering and human intervention [25], [26].

The elements of the convolutional layer are the convolutional filter and activation function. Details on these elements are presented below.

- Convolutional filter: Each convolutional layer is comprised of a number of convolutional filters. The convolutional filter is a small-sized matrix of values (i.e., convolutional filter weights). Each

convolutional filter has three dimensions: height, width, and depth. The height and width of the convolutional filter must be smaller than those of the input image, whereas the depth of the convolutional filter may be less than or equal to that of the input image. At the onset of the DNN, the convolutional filter weights are allocated arbitrarily; they are then fine-tuned during each training period. The tunning assists the convolutional filter in extracting significant characteristics from the input image.

The convolution operation, depicted in Fig. 6.4a, is the primary mathematical component of the convolutional filter. It begins by dragging the convolutional filter horizontally and vertically until the entire image has been parsed. The stride specifies how many blocks the convolutional filter traverses per step. Calculated concurrently is the dot product between the input image pixels and the filter, where their respective values are multiplied and added to generate a single scalar value. The same procedure is repeated until the entire image has been parsed. The output feature map is the calculated dot product values. The illustration in Fig. 6.4a depicts an image of 100×50 pixels convolved with eight filters, with the height and width of each convolutional filter being 5 and 5, respectively (i.e., 5×5). This operation will continue the same procedure by using the output of each convolutional layer as an input for the following layer. The convolutional layers can tune their filters during training. Since the filters are updated during training, manual convolutional filter creation is no longer necessary. In addition, the flexibility of the quantity and relevance of convolutional filters is realized to extract complex features.

- Activation function: The activation function is the leading arbitrator of whether or not a neuron is fired, given a particular input. Hence, it determines the corresponding output and employs non-linear operations [25]. The nonlinearity of the activation functions results in a nonlinear relationship between input and output, enabling the convolutional layer to learn complex structures. Significantly, the activation function can differentiate between various outputs, allowing error back-propagation to train the NN. Examples of activation functions are *sigmoid, tanh, recti-*

fied linear unit (ReLU), and its derivatives. In this study, the selected activation function is *ReLU* because it demands a lesser computing load than other activation functions, making it preferable for CNN. *ReLU* converts the input, d, values to 0 or positive by transforming all negative values to 0, as

$$ReLU(d) = \max(0, d). \tag{6.7}$$

6.3.4.2 Regularization

Regularization is a method for appropriately fitting the loss function to the available training dataset and avoiding overfitting or underfitting. In the proposed HCFNN model, regularization is performed in two layers: maxpooling and dropout. Fig. 6.4b illustrates both regularization stages.

- Maxpooling: Pooling is used in NN models to reduce the dimensionality of intermediate feature maps. Maxpooling is a form of pooling that retains the maximum value within each sub-region of the feature map while discarding all other values. Hence, maxpooling extracts the most dominant and significant features while eliminating irrelevant or chaotic data. Maxpooling is generally regarded as more effective than average pooling at reducing noise and preserving the overall shape of feature maps [27].

  The mathematical formulation of maxpooling is given as

  $$\dot{q} = \max\{Q | Q \in [q_r] \forall r \in \{1, \text{filter size}\}, \tag{6.8}$$

  where Q is a set representing all the pixels of the image, q_r, covered by the convolutional filter at one stride. The size of Q is directly related to the size of the convolutional filter. In Fig. 6.4a, the convolutional filter is assumed to have a size of 2×2 and a stride of two. Based on that assumption, the convolutional filter will overlap with one color (from Fig. 6.4a) at a time. Hence, the filter divides the image into four color-coded sets of pixels, each of which corresponds to a distinct set. These sets are passed to the maxpooling. As shown in Fig. 6.4b the maxpooling operation returns the utmost value of each pixel set as its output. Therefore, the scale of the
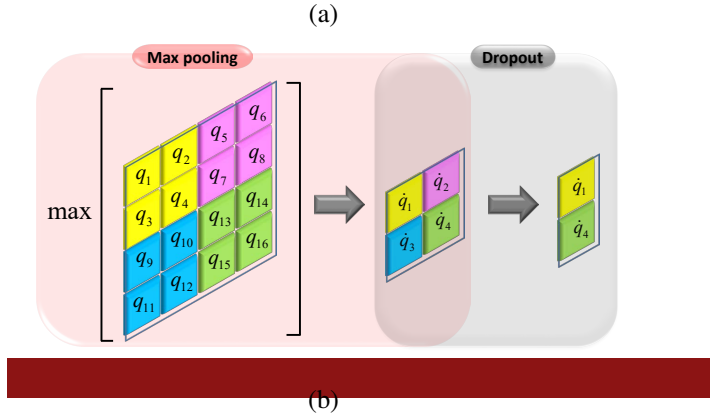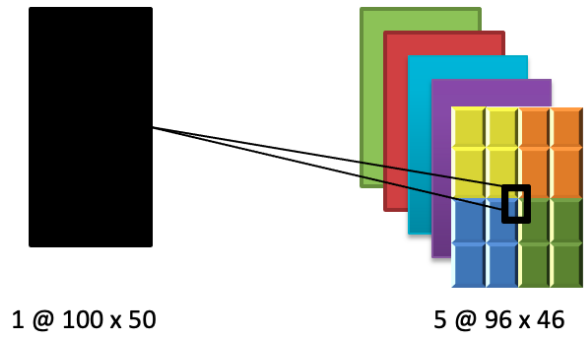
Fig. 6.4: Illustration of (a) Convolution (b) Maxpooling and dropout.

image is reduced from sixteen to four pixels, and any noise or irrelevant features are removed. For example, if the values of pixels q_1 through q_4 range from 1 to 4, the resultant $\dot{q}_1$ will be 4, which is the maximum value in this set.

- Dropout: This is a regularization technique for reducing overfitting in artificial DNNs. The term dropout refers to the random elimination of neurons during the training of an NN [27]. This compels the model to learn different independent features. The equation which represents dropout is $O = \delta I_{do}$, where δ is the dropout factor determining the percentage of the remaining data after omission, I_{do} is the size of the input to the dropout layer, and O is the size of of the output. Fig. 6.4b illustrates the application of 50% dropout on a $2{\times}2$ image, reducing the image size to $2{\times}1$. δ affects the amount of information retained, so it highly affects the performance and optimization of the NN. Hence, δ is a hyperparameter that needs to be properly tuned.

6.3.4.3 Flatten Layer

After learning non-linear combinations of abstract-level structures, the flatten layer creates a column vector from the output image.

6.3.4.4 Dense Layer

Each element from the column output of the flatten layer is connected to all neurons in the dense layer, and similarly each neuron of the dense layer is connected to the three output neurons. The type of the input image will be determined based on the neuron with the highest probability of occurrence.

6.4 Complexity Analysis

Inference complexity, which pertains to the speed and efficiency of making predictions using a pre-trained model, gains prominence over training complexity due to its immediate relevance in providing timely responses. Hence, the memory complexity and computational complexity are the primary contributors to the complexity cost of a DNN. The DNN memory complexity is determined by the number of stored parameters, such as weights and biases for each layer, which are proportional to the memory utilization of the algorithm. The memory complexity is known as parameter complexity, C^{P}. The computational complexity denotes the amount of processing power required to execute the mathematical operations carried out by the DNN. Real multiplications, C^{M}, and additions, C^{A}, are the two primary types of operations that contribute to the computational complexity. C^{P}, C^{M} and C^{A} of a DNN are calculated as the summation over the layers of the DNN. This is mathematically represented as

$$C^{\mathrm{P}} = \Sigma_i C^{\mathrm{P}}_i, \tag{6.9}$$

$$C^{\mathrm{M}} = \Sigma_i C^{\mathrm{M}}_i, \tag{6.10}$$

and

$$C^{\mathrm{A}} = \Sigma_i C^{\mathrm{A}}_i, \tag{6.11}$$

where C_i^P, C_i^M, and C_i^A represent the number of parameters, real additions, and real multiplications of the i-th layer, respectively. In the proposed HCFNN model, layer i can be either a convolutional, regularization, or dense layer. The complexity introduced by each type of layer is presented as follows.

6.4.1 Complexity of Convolutional Layer

The complexity factors of each convolutional layer are calculated as

$$C_{\text{cnn}_i}^P = f_{l_i} f_{w_i} F_i + F_i, \tag{6.12}$$

$$C_{\text{cnn}_i}^M = f_{l_i} f_{w_i} o_{l_i} o_{w_i} F_i, \tag{6.13}$$

and

$$C_{\text{cnn}_i}^A = o_{l_i} o_{w_i} F_i + f_{l_i} f_{w_i} o_{l_i} o_{w_i} F_i, \tag{6.14}$$

where $C_{\text{cnn}_i}^P$, $C_{\text{cnn}_i}^M$ and $C_{\text{cnn}_i}^A$ are the complexity factors for parameters, real multiplications and addition of a convolutional layer, respectively. Here, f_{l_i} and f_{w_i} are the length and width of the convolutional filter applied in layer i, respectively, and F_i is the number of convolutional filters. o_{l_i} and o_{w_i} are the length and width of the output of the i-th layer, calculated as

$$o_{l_i} = \left\lfloor \frac{I_{l_i} - f_{l_i} + 1}{s} \right\rfloor, \tag{6.15}$$

and

$$o_{w_i} = \left\lfloor \frac{I_{w_i} - f_{w_i} + 1}{s} \right\rfloor, \tag{6.16}$$

where I_{l_i} and I_{w_i} are layer i input dimensions. For $i = 1$, I_{l_1} and I_{w_1} are equivalent to the dimensions of the input image. For layers starting $i = 2$, I_{l_i} and I_{w_i} are equivalent to $o_{l_{(i-1)}}$ and $o_{w_{(i-1)}}$, respectively, as the output of layer $i - 1$ is the input of layer i. Here, s is the stride of the convolutional filters.

6.4.2 Complexity of Regularization

The regularization layers do not directly contribute to C^P, C^M, or C^A. However, the regularization operation changes the size of the layer input going through it. Consequently, the regularization layer

affects the complexity of the subsequent layers, by varying the size of the input of the subsequent layer. In the proposed HFCNN model, the regularization layer operates on the output of the last convolutional layer. Assume the size of the last convolutional layer is o^{cnn}. Then, the size of the output of the maxpool layer, o^{mp}, is calculated as

$$o^{\text{mp}} = \eta o^{\text{cnn}}, \tag{6.17}$$

where η is the maxpool factor and o^{cnn} is the multiplication of o_{l_i} by o_{w_i} of the last convolutional layers, calculated using (6.15) and (6.16), respectively. f_{l_i}, f_{w_i}, and s are considered as hyperparameters.

The maxpool layer is followed by a dropout layer. The size of the output of the dropout layer is denoted by o^{do}, which is calculated as

$$o^{\text{do}} = \delta o^{\text{mp}}, \tag{6.18}$$

where δ is the dropout factor assigned as a hyperparameter.

The flatten layer succeeds the regularization, and transforms the 2D output from the drop out layer to a column vector of the size o^{do}. The flatten layer does not introduce any additional complexity, as its sole function is to reorganize the input's structure.

6.4.3 Complexity of Dense Layer

The complexity of the dense layer is calculated as

$$C_{\text{D}_i}^{\text{P}} = (o^{\text{do}} + 1)N_i, \tag{6.19}$$

$$C_{\text{D}_i}^{\text{M}} = (o^{\text{do}})N_i, \tag{6.20}$$

and

$$C_{\text{D}_i}^{\prime\text{A}} = (o^{\text{do}})N_i + N_i, \tag{6.21}$$

where the number of neurons of the dense layer is N_i.

6.5 Experimental Setup and Results

This section describes the experimental setup used to acquire over-the-air PSD measurements for the three cellular signal types, followed by a performance evaluation of the proposed HCFNN model in terms of the identification accuracy and PR for both acquisition modes. The complexity cost and identification accuracy metrics are then used to evaluate the proposed HCFNN model compared to other DNN and ASI models.

6.5.1 Experimental Setup

A proprietary software defined radio receiver was used to gather the over-the-air measurements. The receiver can capture RF signals within the 20-6000 MHz band with a spur free dynamic range of 70 dB and noise figure of 10 dB in an instantaneous capture bandwidth of 100 MHz. Each captured band had a different centre frequency and was band-pass filtered before being down-converted to intermediate frequency (IF) and filtered to 100 MHz bandwidth. The IF signals were next converted to complex in-phase and quadrature components by sampling them at 250 MSPS. In a field-programmable gate array, complex time domain samples were subjected to 1024-point fast Fourier transforms (FFT), which produced an approximate 122 kHz FFT bin size. To generate PSD estimates, magnitude squared FFT values were then averaged over a number of frames. The SNR range of the captured data is 10 dB to 50 dB. The data were collected and exported to ASCII files to be processed in MATLAB®. MATLAB® was then used to divide the processed PSD measurements into their constituent signals as per Section 6.3. The signal images were fed into a Python code that constructs and evaluated the proposed HCFNN model.

Fig. 6.5 depicts a modified capture of a 1900 MHz spectrum from the ROMES software that includes the downlinks of UMTS, GSM, and LTE. The colored rectangles show the occupied areas of the spectrum, and the grey areas show the unoccupied parts of the spectrum. Data is gathered from four distinct frequency bands employed at different locations. The frequency bands are 900 MHz, 2100

TABLE 6.1: Count and types of signals per frequency band.

Band	Frequency (MHz)	GSM	UMTS	LTE
1	900	104	78	-
2	2100	-	1662	1662
3	1900	1652	1652	825
4	850	2793	2793	-

MHz, 1900 MHz, and 850 MHz, designated as frequency bands 1 through 4. Table 6.1 shows the number and types of signals extracted from each frequency band. Band 1 is comprised of 104 GSM signals and 78 UMTS signals. Band 2 is composed of 1662 UMTS and 1662 LTE signals. Band 3 contains 1652 LTE, 1652 UMTS, and 825 GSM signals, while band 4 contains 2793 UMTS and 2793 GSM signals. The measurements of the signals were used to construct balanced training and testing datasets, with 70% for training and 30% for testing, for various scenarios. The identification accuracy and PR metrics are used to construct and evaluate the proposed HCFNN model.

Fig. 6.5: ROMES software output.

6.5.2 Proposed HCFNN Parameters

Table 6.2 shows the parameters of the proposed HCFNN algorithm. The input image is resized to $H_{in} \times T_{in}$ dimensions of 100×50 pixels. The input image is sent to a DCNN structure with four hidden layers; each layer contains eight 5×5 convolutional filters. The output of the CNN is forwarded to a

TABLE 6.2: Proposed HCFNN parameters.

Parameter	Value
Input image height (H_{in})	100
Input image width (T_{in})	50
CNN filter size	5×5
Number of filters	8
Maxpool filter size	2×2
Maxpool stride (s)	2
Drop out factor (δ)	0.4
Dense layer neuroens	400
Learning rate	0.01

maxpool layer of a 2×2 convolutional filter with $s = 2$. Then, a dropout layer with $\delta = 0.4$ is applied. The output of the dropout layer is flattened, then passed to a 400 neuron dense layer through a fully connected feedforward network. Finally, the output layer is a fully connected dense layer with three neurons, which categorizes the input PSD signal into one of three categories representing the three cellular signal types. The optimizer employed in this work is *Adam* at a learning rate of 0.01. The loss function used is *categorical-cross-entropy*. The number of epochs and batch size are independently tuned hyperparameters for each scenario. For the IB-PSD acquisition mode, the following parameters are selected: epochs of 58, 100, 20, and 19, batch sizes of 4, 32, 500, and 10 for frequency bands 1 to 4, respectively. A batch size of 500 and 20 epochs are used for the MB-PSD acquisition mode.

6.5.3 Results and Discussion

6.5.3.1 IB-PSD Acquisition

In the IB-PSD acquisition mode, the data from each frequency band is assessed independently of the other frequency bands. The proposed HCFNN model is trained and tested using datasets collected from the same frequency band.

The accuracy in identifying cellular signal types using the proposed HCFNN model with IB-PSD acquisition mode is presented in Table 6.3. The results show that the cellular signal identification is nearly perfect across all types for the best TensorFlow (TF) seed. To assess the robustness of the proposed HCFNN model, training and testing are performed using 10 and 30 random TF seeds. The identification accuracies of 10 randomly selected TF seeds are robust, with a minimum average accuracy of 97.50%. Furthermore, the results indicate that the average identification accuracies of 30 randomly selected TF seeds are good, with a minimum average accuracy above 92%. The table shows that the frequency band with the highest average identification accuracy is band 3. This is primarily due to the diversity of the training dataset, which includes all types of data, unlike the rest of the bands with only two cellular signal types. Thus, the ability to identify distinct characteristics is enhanced.

In order to examine the distribution of the average identification accuracy for each type across all frequencies, the histogram of the identification accuracy is depicted in Fig. 6.6. Figs. 6 (a), (b) and (c) show the identification accuracy values corresponding to 30 random TF seeds per band for GSM, UMTS, and LTE, respectively. Based on Table I, GSM can be found in the frequency bands 1, 3, and 4 with 30 random TF seeds each; accordingly, GSM has 90 identification accuracy measurements. Similarly, UMTS and LTE exist in four and two frequency bands, respectively. Thus, the figures showcase a total of 90 identification accuracy measurements for GSM, 120 for UMTS, and 60 for LTE. Figs. 6 (a), (b), and (c) show that most of the random TF seeds for all cellular types provide near-perfect identification accuracy. The average identification accuracy of GSM, UMTS, and LTE across all frequency bands for 30 random TF seeds are 97.68%, 97.04%, and 98.67%, respectively.

TABLE 6.3: Average IB-PSD identification accuracy: best seed and multiple random TF seeds.

Band	GSM			UMTS			LTE		
	Best seed	10 seeds	30 seeds	Best seed	10 seeds	30 seeds	Best seed	10 seeds	30 seeds
1	100%	98.0%	94.33%	100%	97.50%	92.17%	-	-	-
2	-	-	-	99.81%	99.22%	98.50%	100%	98.07%	97.34%
3	100%	100%	100%	100%	100%	100%	100%	100%	100%
4	100%	98.97%	98.73%	100%	98.15%	97.50%	-	-	-
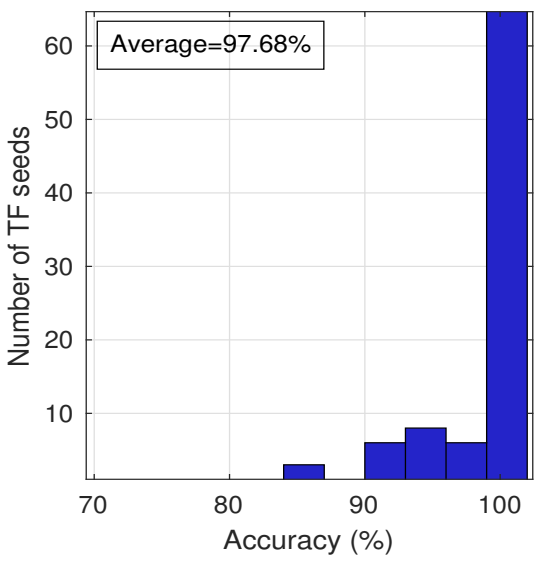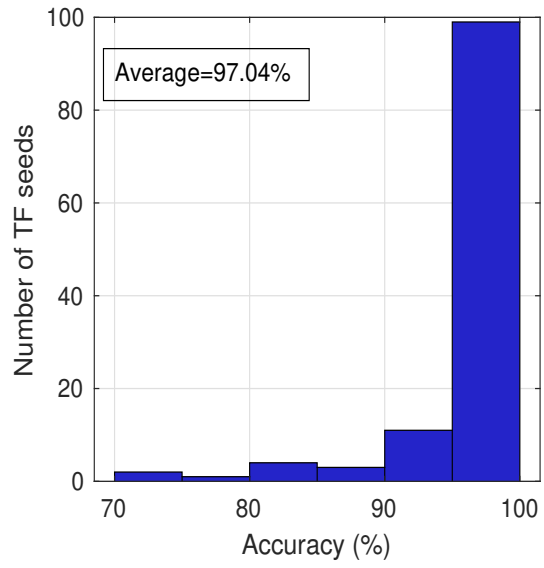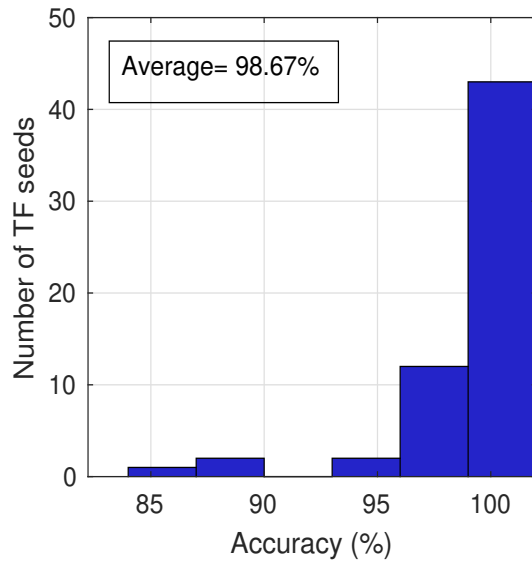
Fig. 6.6: IB-PSD identification accuracy histogram of 30 random TF seeds per band (a) GSM (b) UMTS (c) LTE.

TABLE 6.4: Average MB-PSD identification accuracy: best seed and multiple random TF seeds.

No. Seeds	GSM Accuracy	UMTS Accuracy	LTE Accuracy
Best seed	100%	99.90%	99.80%
10	100%	99.89%	99.76%
30	99.99%	99.88%	99.58%

6.5.3.2 MB-PSD Acquisition

In the MB-PSD acquisition model, all PSD measurements from all frequency bands are used for training and testing. The signal identification accuracy of the best and different number of TF seeds is shown in Table 6.4. The MB-PSD identification accuracy is nearly perfect for the 10 and 30 random TF seeds with a minimum of 99.99%, 99.88%, and 99.58% for GSM, UMTS, and LTE, respectively, and a maximum of 100%. For further illustration, the histogram showing the distribution of the 30 random TF seeds for each cellular signal type is illustrated in Fig. 6.7. This figure shows that the minimum identification accuracy of all cellular signal types for all random TF seeds is 99.17% for LTE. The average identification accuracy of GSM, UMTS, and LTE across all frequency bands for 30 random TF seeds is 99.99%, 99.88%, and 99.58%, respectively.

6.5.3.3 Comparison of Different Acquisition Modes

Fig. 6.8 compares the identification accuracy of various frequency bands in IB-PSD and MB-PSD, over 30 random TF seeds. This figure shows that frequency band 3 in the IB-PSD and MB-PSD acquisition modes has the best identification accuracy for the three cellular signal types due to the diversity of the dataset used in training.

To compare the overall performance of all cellular signal types for the IB-PSD and MB-PSD acquisition modes, the average identification accuracy of each frequency band for 30 random TF seeds is depicted in Fig. 6.9. The figure shows that the average identification accuracy of the MB-PSD model

is around 3% better than identification accuracy of the IB-PSD model. The average identification accuracy of the GSM, UMTS, and LTE is improved in the MB-PSD model by around 3%, 2%, and 1%, respectively, compared with the same cellular signal type in the IB-PSD model. The main reason behind the improved performance of the MB-PSD acquisition mode is the variety and more extensive
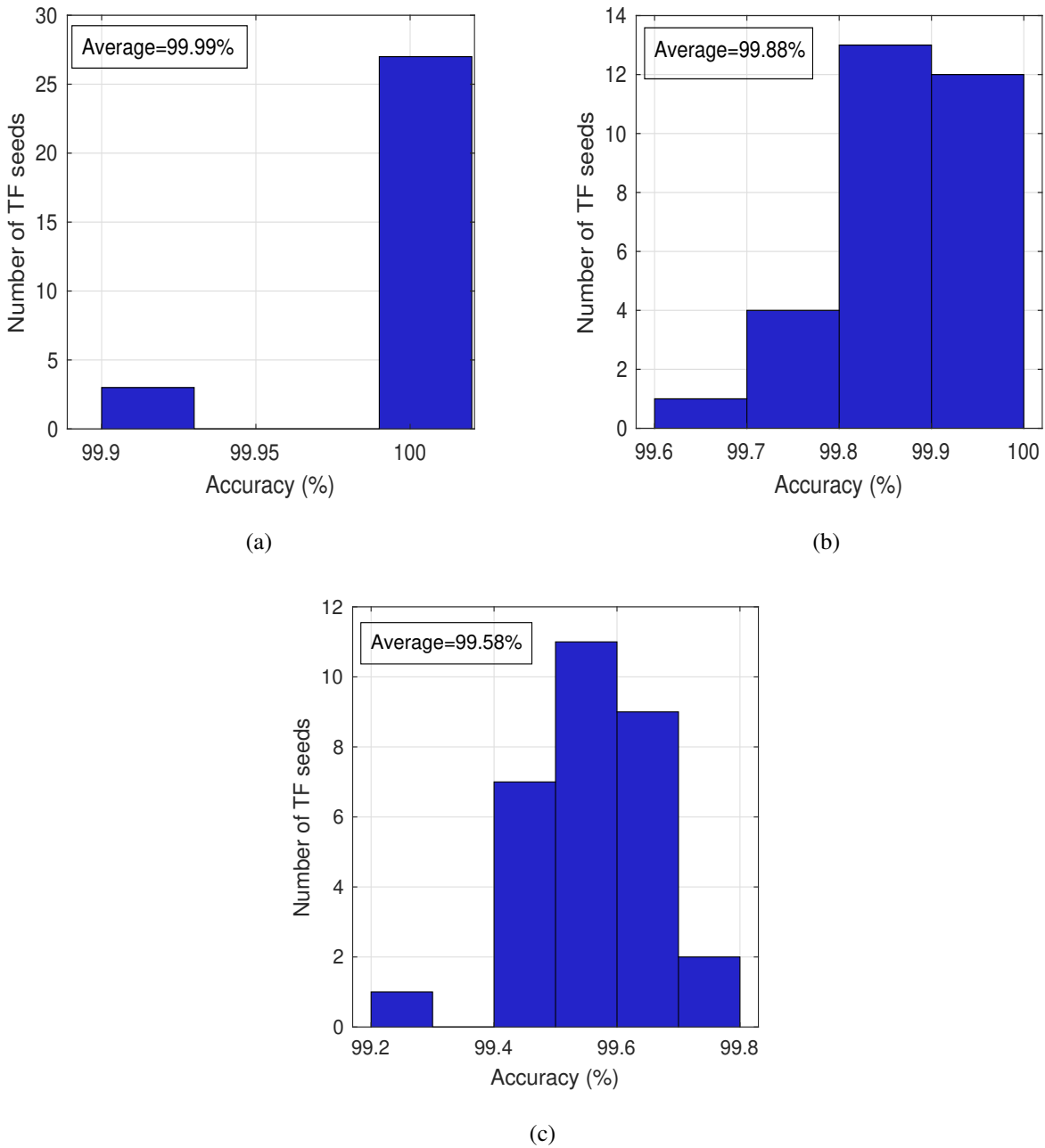
Fig. 6.7: MB-PSD identification accuracy histogram of 30 random TF seeds (a) GSM (b) UMTS (c) LTE.
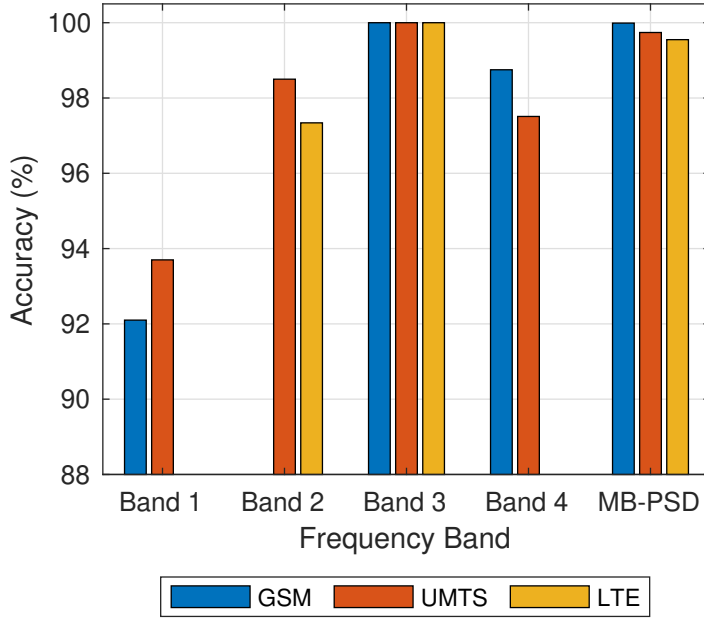
Fig. 6.8: Identification accuracy of IB-PSD on each band compared to MB-PSD for 30 random TF seeds.

dataset used to train the proposed HCFNN model.

6.5.3.4   PR Performance Assessments

Other metrics than accuracy are sometimes used to evaluate the performance of the proposed HCFNN model. PR are the most widely employed performance metrics. The following formulas respectively illustrate the definition of PR, as

$$Precision = \frac{TP}{FP + TP},$$ (6.22)

and

$$Recall = \frac{TP}{FN + TP},$$ (6.23)

where TP, FP, and FN stand for true positive, false positive, and false negative, respectively. TP indicates the values that are correctly identified as belonging to a particular output category, whereas

TABLE 6.5: Average PR for 30 random TF seeds.

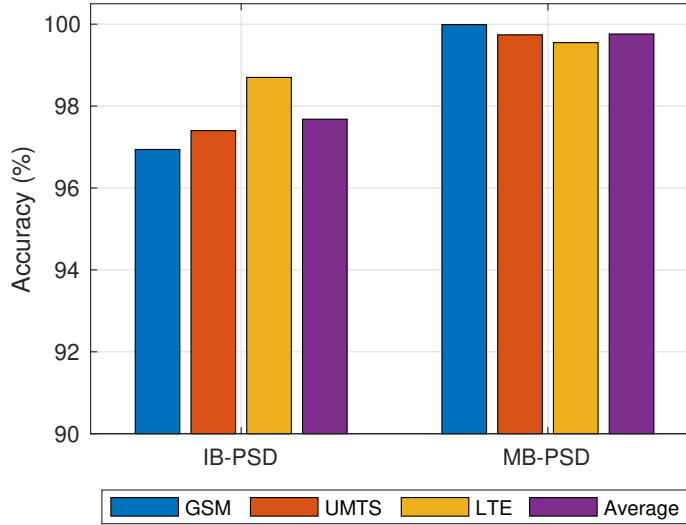| Band	GSM Precision	GSM Recall	UMTS Precision	UMTS Recall	LTE Precision	LTE Recall
1	93.71%	93.08%	92.10%	94.60%	-	-
2	-	-	97.34%	98.53%	98.50%	97.49%
3	99.99%	99.97%	99.95%	100%	100%	99.96%
4	97.50%	98.80%	98.73%	97.78%	-	-
Average IB-PSD	97.06%	97.28%	97.03%	97.94%	99.04%	98.28%
MB-PSD	99.99%	99.67%	99.73%	99.67%	99.86%	99.58%

Fig. 6.9: Average identification accuracy for MB-PSD vs. IB-PSD acquisition modes for 30 random TF seeds.

FP refers to identifying the input as belonging to a particular output category when it does not. FN represents identifying an input as not belonging to a particular output category when it does.

The average PR values for 30 random TF seeds are presented in Table 6.5. The table shows high PR with a minimum precision of 92.10% for the UMTS in frequency band 1, and minimum recall of 93.08% for the GSM in the frequency band 1. On the other hand, most of the PR vary from 97% to 100%. Moreover, the overall improved identification performance of the MB-PSD acquisition mode when compared to the IB-PSD acquisition mode is also maintained when considering the PR performance metrics.

The PR-curves for the proposed HCFNN model of the IB-PSD acquisition mode for frequency bands 1 to 4 are shown in Figs. 6.10-6.13, respectively, while the MB-PSD acquisition mode is depicted in Fig. 6.14. The PR curves are illustrated per TF seed, so each curve contains a plot of the best-performing and worst-performing TF seeds out of 30 random TF seeds. In both IB-PSD and MB-PSD acquisition modes, the best TF seed exhibits the ideal PR curve across all frequency bands for all cellular signal types, while the worst-performing TF seed provides a near-ideal performance. This proves the robustness of the proposed HCFNN model from the perspective of the PR metrics.
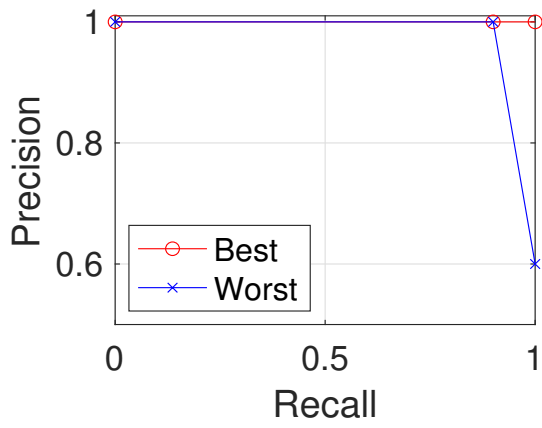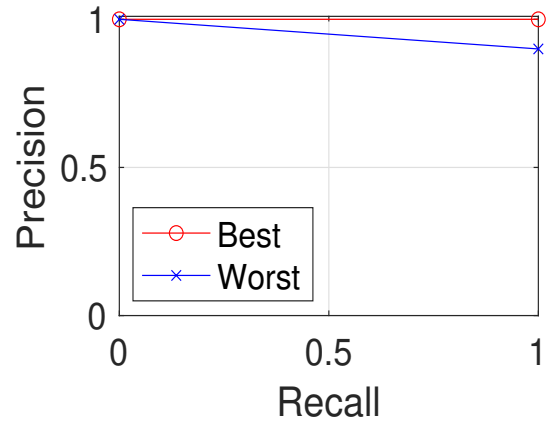
Fig. 6.10: PR curves of the IB-PSD frequency band 1 for the best and worst seeds out of 30 random TF seeds (a) GSM (b) UMTS.

Fig. 6.11: PR curves of the IB-PSD frequency band 2 for the best and worst seeds out of 30 random TF seeds (a) UMTS (b) LTE.

(a)

Fig. 6.12: PR curves of the IB-PSD frequency band 3 for the best and worst seeds out of 30 random TF seeds GSM, UMTS and LTE.
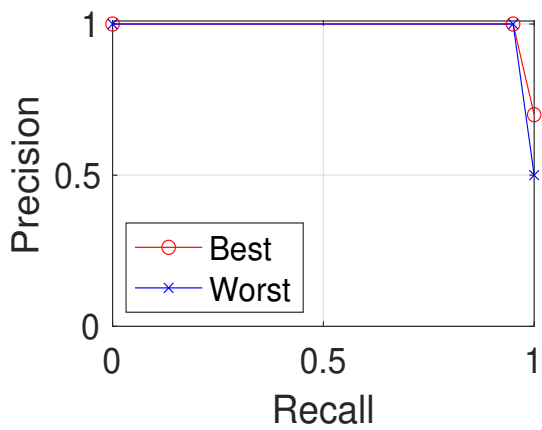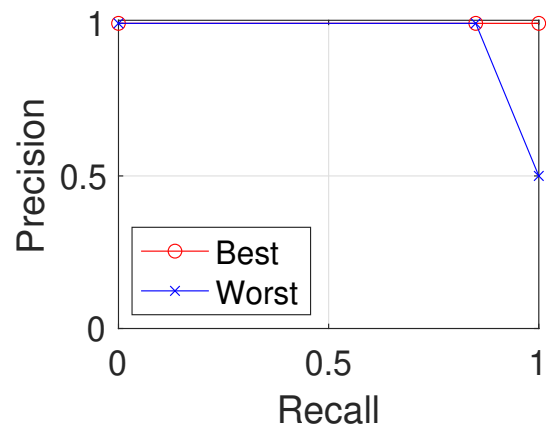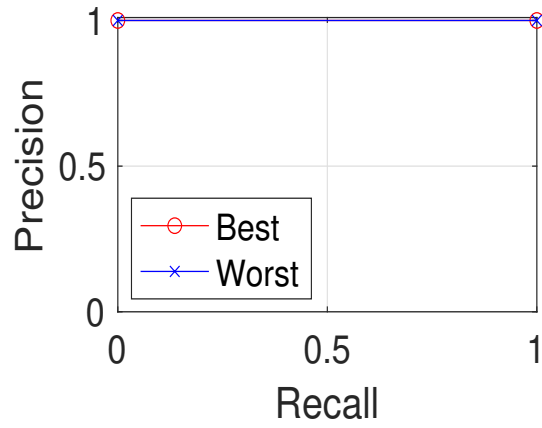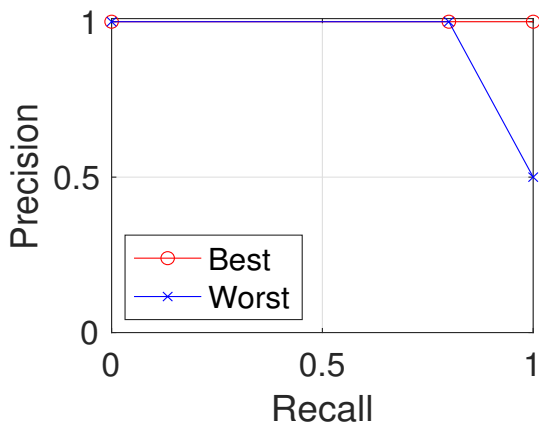

(a)
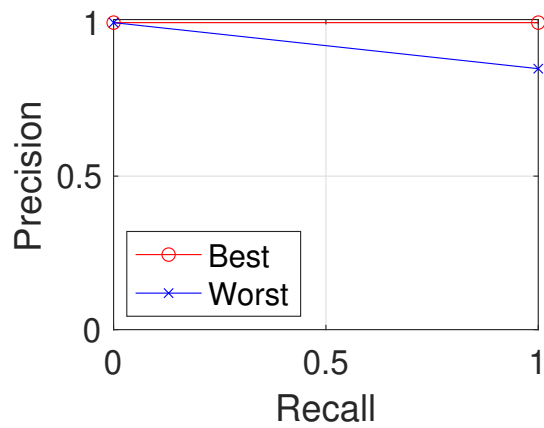
(b)

Fig. 6.13: PR curves of the IB-PSD frequency band 4 for the best and worst seeds out of 30 random TF seeds (a) GSM and (b) UMTS.
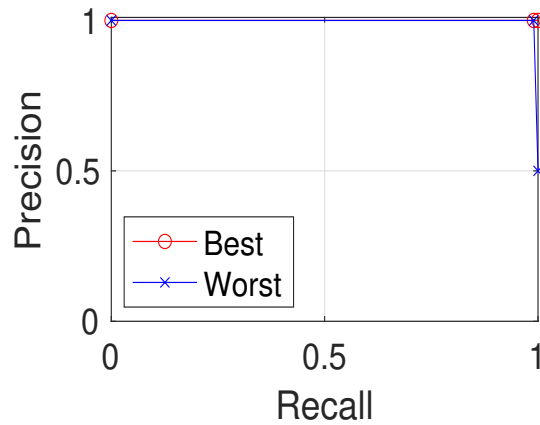
(a)

Fig. 6.14: PR curves of the MB-PSD for the best and worst seeds out of 30 random TF seeds GSM, UMTS and LTE.

6.5.3.5 Comparison with other Identification Models

The proposed HCFNN model is compared with a four-hidden layer DCNN with and without regularization preprocessing. The DCNN structure with regularization is referred to as DCNNR. Furthermore, the proposed HCFNN model is compared against two recently published signal identification models, namely ASI [5], which employs a traditional ASI method, and DNN [21], which presents a model based on DNN architecture. Both models are comparable to our work because they use over-the-air signals, rather than synthetically generated signals. All models are compared in terms of complexity and identification accuracy. The calculation of the complexity of the two DCNN structures and the proposed HCFNN model is based on Section 6.4, and that of the complexity DNN and ASI methods is based on [21] and [5], respectively. The result of the complexity analysis is shown in Fig. 6.15. The identification accuracy for the IB-PSD and MB-PSD acquisition modes are shown in Fig. 6.16 and 6.17, respectively.

As depicted in Fig. 6.15, the most complex models are ASI and DNN. The proposed HCFNN model has at least 25% improvement in complexity compared to these models per complexity factor. The HCFNN model has a slight increase in complexity compared to the DCNN model, and the DCNNR

model has the lowest level of complexity among all models. However, the difference in the overall complexity between HCFNN, DCNN and DCNNR is barely perceptible. It can be seen in Fig. 6.15 that the complexity factors C_M and C_A are nearly similar across the three algorithms. Only for the C_P does the proposed algorithm have a higher complexity than the other two scenarios. However, the C_P values (on the order of 10^3) are negligible when compared to the overall complexity (on the order of 10^6); therefore, the big discrepancy in C_P is similarly inconsequential.

For the identification accuracy, the proposed model exhibits an outstanding improvement in accuracy of up to 26% when compared to the traditional ASI model [5], as shown in Figs. 6.15 and 6.16. In both IB-PSD and MB-PSD acquisition modes, the proposed HCFNN model yields impressive improvements in identification accuracy. These are 7%, 26%, and 10% for identifying GSM, UMTS, and LTE signals in the former and 8%, 3%, and 11% in the latter, respectively.

When comparing the proposed HCFNN model to the DNN [21] model in terms of identification accuracy in the IB-PSD acquisition mode, the proposed HCFNN model achieves a 2% improvement for UMTS and a 3% enhancement for LTE. Additionally, for the MB-PSD acquisition mode, the proposed HCFNN model has an enhanced identification accuracy of 3% for GSM and LTE, and 7% for UMTS.

This comparison unequivocally establishes the superiority of the proposed HCFNN model over literature models in terms of identification accuracy and complexity for various signal types in both IB-PSD and MB-PSD acquisition modes.

Following the comparison with literature models, the identification accuracy of the proposed model is compared with other DCNN models, specifically DCNN and DCNNR. As shown in Fig. 6.16, the average identification accuracy for HCFNN is better than that of the other models for all cellular signal types in the IB-PSD acquisition mode with an improvement of up to 6%. For the MB-PSD, the improvement is minimal for GSM, which is accurately identified for all models. The identification accuracy of the UMTS improves by 2% and 1% for the HCFNN model when compared with DCNNR and DCNN, respectively. The variation between the identification accuracy of the LTE and the GSM for the three models is negligible.

Consequently, the proposed HCFNN model substantiates its superiority across all alternative models, irrespective of the acquisition mode or the signal types under consideration.
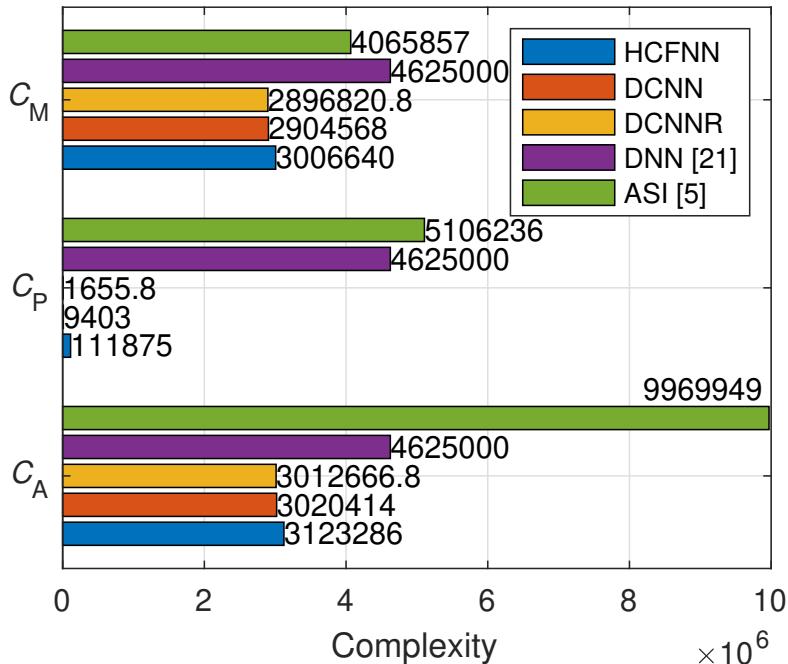
Fig. 6.15: Complexity comparison of different models.

6.6 Conclusion

In this chapter, I proposed an HCFNN model to identify the cellular signals of LTE, GSM, and UMTS. The proposed model consists of an input layer, four convolutional hidden layers, a regularization layer, a 400-neuron dense layer, and an output layer that classifies the input PSD signals into one of the three cellular signal types. Two PSD acquisition modes were investigated: MB-PSD and IB-PSD models. The training and testing datasets are collected from multiple frequency bands in the MB-PSD acquisition mode. For IB-PSD, the proposed HCFNN model for each frequency band was trained based only on its data. Different numbers of random TF seeds, performance metrics, and the complexity cost were considered to assess the proposed HCFNN model. For the IB-PSD acquisition mode, the
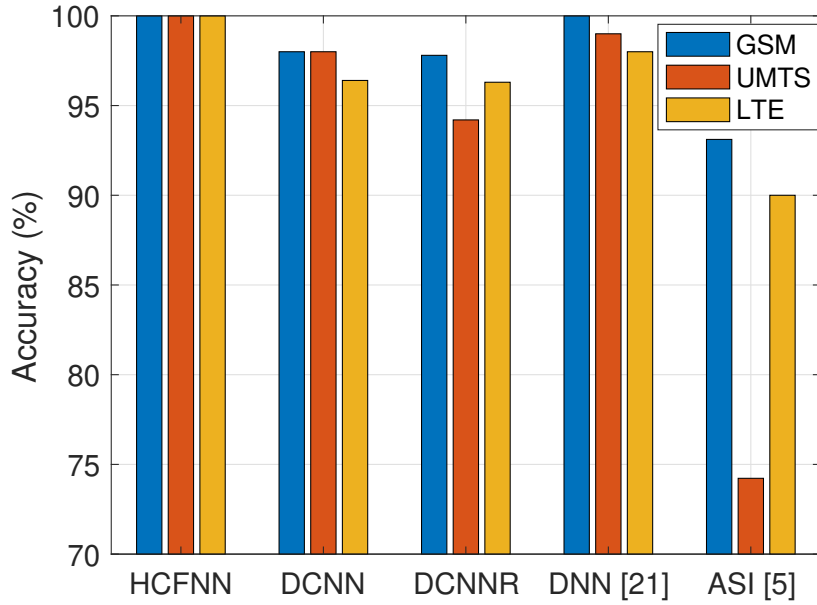
Fig. 6.16: Average identification accuracy of different models for the IB-PSD acquisition mode.
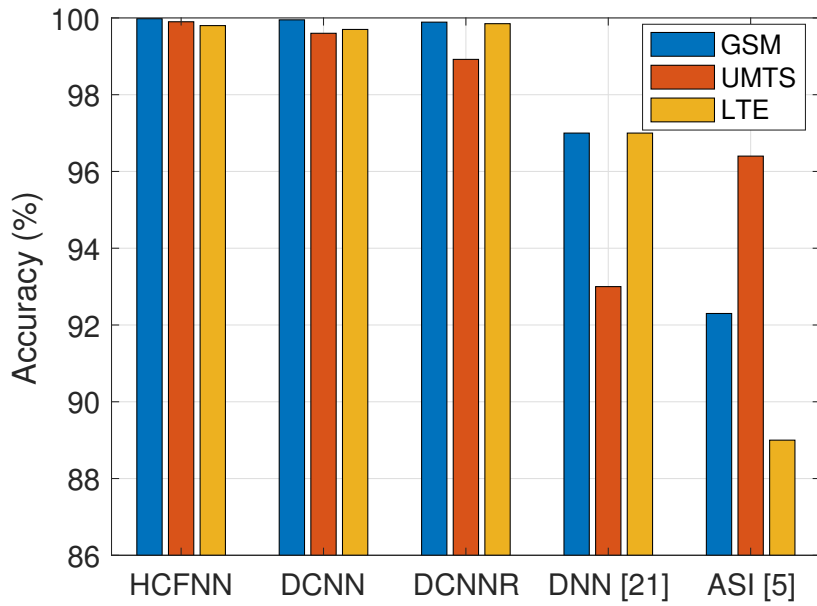
Fig. 6.17: Average identification accuracy of different models for the MB-PSD acquisition mode.

identification accuracy varied from 94.33% to 100%, from 92.17% to 100%, and from 97.34% to 100% for GSM, UMTS, and LTE, respectively, for all frequency bands. For the MB-PSD acquisition mode,

the identification accuracy varied from 99.99% to 100%, from 99.88% to 100%, and from 99.58% to 100% for GSM, UMTS, and LTE, respectively. Furthermore, the PR of the proposed HCFNN model varied from near-ideal performance to ideal performance for both IB-PSD and MB-PSD acquisitions. Finally, the proposed HCFNN model was compared to different DCNN structures, and earlier DNN model and ASI models from the literature in terms of identification accuracy and complexity. The proposed model provided the highest identification accuracy across all the studied scenarios, with lower complexity compared to ASI and DNN structures and with comparable complexity compared to DCNN structures.

References

[1] Y. A. Eldemerdash, O. A. Dobre, O. Üreten, and T. Yensen, "Identification of cellular networks for intelligent radio measurements," *IEEE Trans. Instrum. Meas.*, vol. 66, no. 8, pp. 2204–2211, Aug. 2017.

[2] ——, "Fast and robust identification of GSM and LTE signals," in *Proc. IEEE Int. Instrum. Meas. Technol. Conf. (I2MTC)*, 2017, pp. 1–6.

[3] E. Karami, O. A. Dobre, and N. Adnani, "Identification of GSM and LTE signals using their second-order cyclostationarity," in *Proc. IEEE Int. Instrum. Meas. Technol. Conf. (I2MTC)*, 2015, pp. 1108–1112.

[4] O. A. Dobre, "Signal identification for emerging intelligent radios: classical problems and new challenges," *IEEE Instrum. Meas. Mag.*, vol. 18, no. 2, pp. 11–18, Apr. 2015.

[5] E. A. Makled, A. A. Al-Habob, O. A. Dobre, and O. Üreten, "Detection and identification of mobile network signals," *IEEE Trans. Instrum. Meas.*, vol. 70, pp. 1–4, Sep. 2021.

[6] F. Hameed, O. A. Dobre, and D. C. Popescu, "On the likelihood-based approach to modulation classification," *IEEE Trans. Wireless Commun.*, vol. 8, no. 12, pp. 5884–5892, Dec. 2009.

[7] E. E. Azzouz and A. K. Nandi, "Modulation recognition using artificial neural networks," in *Automatic Modulation Recognition of Communication Signals*. Springer, 1996, pp. 132–176.

[8] M. D. Wong and A. K. Nandi, "Automatic digital modulation recognition using spectral and statistical features with multi-layer perceptrons," in *Proc. 6th Int. Symposium on Signal Processing and its Applications*, 2001, pp. 390–393.

[9] A. K. Nandi and E. E. Azzouz, "Algorithms for automatic modulation recognition of communication signals," *IEEE Trans. Commun.*, vol. 46, no. 4, pp. 431–436, Apr. 1998.

[10] H. Agirman-Tosun, Y. Liu, A. Haimovich, O. Simeone, W. Su, J. Dabin, and E. Kanterakis, "Modulation classification of mimo-ofdm signals by independent component analysis and support vector machines," in *Proc. Conf. Record of the 45th Asilomar Conf. on Signals, Systems and Computers (ASILOMAR)*, 2011, pp. 1903–1907.

[11] J. Lv, L. Zhang, and X. Teng, "A modulation classification based on svm," in *Proc. IEEE 15th Int. Conf. on Optical Communs. and Networks (ICOCN)*, 2016, pp. 1–3.

[12] C.-S. Park, J.-H. Choi, S.-P. Nah, W. Jang, and D. Y. Kim, "Automatic modulation recognition of digital signals using wavelet features and svm," in *Proc. 10th Int. Conf. on Advanced Commun. Technology*, 2008, pp. 387–390.

[13] X. Gong, L. Bian, and Q. Zhu, "Collaborative modulation recognition based on SVM," in *Proc. 6th Int. Conf. on Natural Computation*, 2010, pp. 871–874.

[14] A. Nandi and E. Azzouz, "Algorithms for automatic modulation recognition of communication signals," *IEEE Trans. Commun.*, vol. 46, no. 4, pp. 431–436, Apr. 1998.

[15] M. D. Wong, S. K. Ting, and A. K. Nandi, "Naive bayes classification of adaptive broadband wireless modulation schemes with higher order cumulants," in *Proc. 2nd Int. Conf. on Signal Process. and Commun. Syst.*, 2008, pp. 1–5.

[16] X. Li, F. Dong, S. Zhang, and W. Guo, "A survey on deep learning techniques in wireless signal recognition," *Wireless Communs. and Mobile Computing*, vol. 2019, pp. 1–12, 2019.

[17] H. Xia, K. Alshathri, V. B. Lawrence, Y.-D. Yao, A. Montalvo, M. Rauchwerk, and R. Cupo, "Cellular signal identification using convolutional neural networks: AWGN and rayleigh fading channels," in *Proc. IEEE Int. Symposium on Dynamic Spectrum Access Networks*, 2019, pp. 1–5.

[18] K. Ahmad, U. Meier, and H. Kwasnicka, "Fuzzy logic based signal classification with cognitive radios for standard wireless technologies," in *Proc. IEEE 5th International Conf. on Cognitive Radio Oriented Wireless Networks and Communs.*, 2010, pp. 1–5.

[19] K. Ahmad, G. Shresta, U. Meier, and H. Kwasnicka, "Neuro-fuzzy signal classifier (NFSC) for standard wireless technologies," in *Proc. IEEE 7th International Symposium on Wireless Commun. Systems*, 2010, pp. 616–620.

[20] M. Schmidt, D. Block, and U. Meier, "Wireless interference identification with convolutional neural networks," in *Proc. IEEE 15th International Conf. on Industrial Informatics (INDIN)*, 2017, pp. 180–185.

[21] E. A. Makled, I. Al-Nahhal, O. A. Dobre, and O. Üreten, "Identification of cellular signal measurements using machine learning," *IEEE Transactions on Instrumentation and Measurement*, vol. 72, pp. 1–4, Jan. 2023.

[22] K. Alshathri, H. Xia, V. Lawrence, and Y.-D. Yao, "Cellular system identification using deep learning: GSM, UMTS and LTE," in *Proc. 28th Wireless and Optical Communs. Conference (WOCC)*, 2019, pp. 1–4.

[23] H. Xia, K. Alshathri, V. B. Lawrence, Y.-D. Yao, A. Montalvo, M. Rauchwerk, and R. Cupo, "Cellular signal identification using convolutional neural networks: AWGN and rayleigh fading channels," in *Proc. IEEE Int. Symposium on Dynamic Spectrum Access Networks*, 2019, pp. 1–5.

[24] M. Mohammadkarimi, M. Mehrabi, M. Ardakani, and Y. Jing, "Deep learning-based sphere decoding," *IEEE Trans. Wireless Commun.*, vol. 18, no. 9, pp. 4368–4378, Jun. 2019.

[25] L. Alzubaidi, J. Zhang, A. J. Humaidi, A. Al-Dujaili, Y. Duan, O. Al-Shamma, J. Santamaría, M. A. Fadhel, M. Al-Amidie, and L. Farhan, "Review of deep learning: Concepts, CNN architectures, challenges, applications, future directions," *J. Big Data*, vol. 8, no. 1, pp. 1–74, Mar. 2021.

[26] M. M. Najafabadi, F. Villanustre, T. M. Khoshgoftaar, N. Seliya, R. Wald, and E. Muharemagic, "Deep learning applications and challenges in big data analytics," *J. Big Data*, vol. 2, no. 1, pp. 1–21, Feb. 2015.

[27] Z. Li, F. Liu, W. Yang, S. Peng, and J. Zhou, "A survey of convolutional neural networks: Analysis, applications, and prospects," *IEEE Trans. Neural Netw. Learn. Syst.*, vol. 33, no. 12, pp. 1–21, Jun. 2021.

Chapter 7

Identification of Cellular Signal Measurements Using Extreme Learning Machine

7.1 Abstract

Intelligent radios play a pivotal role in optimizing communication resources for both commercial and military applications. Automatic signal identification (ASI) serves as a crucial component for intelligent radios, with likelihood-based and feature-based ASI algorithms being conventional approaches. Recent studies have explored the integration of machine learning (ML) algorithms for ASI, revealing their enhanced resilience to channel distortions compared to traditional methods. This chapter proposes the application of an extreme learning machine (ELM), a type of ML algorithm, for the identification of cellular signals based on over-the-air measurements of power spectral density (PSD). The proposed ELM structure is comprehensively discussed, and its complexity cost is derived in terms of real multiplications, real additions, and stored parameters. The proposed ELM undergoes evaluation using two distinct datasets of PSDs to assess identification accuracy, with the first dataset utilized for hyperpa-

rameter optimization and the second unseen dataset employed to evaluate robustness and generality. The experimental results showcase improved performance in both accuracy and training complexity compared to recent work in the literature.

7.2   Introduction

The rise in the number of wireless devices has elevated the demand on the scarce radio spectrum. This has motivated the need to utilize the spectrum efficiently. Intelligent radios efficiently use communication resources for commercial and military purposes [1]. Automatic signal identification (ASI) plays a pivotal role in intelligent radios [2], [3]. The principle ASI algorithms are likelihood-based and feature-based, as extensively discussed in literature such as [1], [4]–[7]. The former are characterized by their higher complexity, whereas the latter perform poorly in comparison [3] [2]. Recent research has focused on using machine learning (ML) algorithms in ASI [8]–[14]. ML classification models demonstrated a more robust response to various channel variations than likelihood-based and feature-based classification strategies when trained with representative and diverse data. In earlier works [15] [16], ML techniques, including convolutional and feedforward neural networks (NNs), were used to classify real power spectral density (PSD) measurements into their corresponding cellular signals type. Despite the fact that ML is more computationally efficient than classic ASI techniques, ML algorithms continue to be regarded as resource-intensive [11]. In their training methodology, ML algorithms heavily rely on numerical optimization and backpropagation [17]. In order to compute the error gradient for each NN parameter, these methods necessitate lengthy training periods and costly hardware [17].

Random vector functional link (RVFL) networks were introduced and explained in [18], [19]. In earlier times, RVFL was ambitious with regard to hardware capability. Recently, with the advancement of hardware, it has been further developed and evaluated in [20], [21]. Using a single hidden layer and direct connections between the input and output layers, the feedforward network RVFL bypasses the hidden layer. The differentiating feature of the RVFL is that the hidden layer's weights are set randomly

147

and not optimized. Hence, the weights of the output layer are the sole trainable parameters. As a special instance of the RVFL NN, the authors of [22] proposed an extreme learning machine (ELM). ELM is an ML algorithm that belongs to the family of single-hidden layer feedforward NNs. It was introduced as a fast and efficient learning algorithm. In ELM, the direct input-output link is disabled [23]. ELM shares the same architecture as conventional feedforward NNs with a single hidden layer. The distinction between them is their respective training methods. Unlike traditional NNs that require iterative training, the ELM adopts a random initialization of the input-to-hidden layer weights and analytically determines the output weights. This approach allows the ELM to achieve fast training speed while maintaining good generalization performance. The ELM can be considered a linear algorithm, gaining nonlinearity from the activation function. ELM has gained popularity in various applications due to its simplicity, computational efficiency, excellent generalization performance at an incredibly rapid learning rate, and ability to handle large-scale datasets [22], [24].

Cellular drive test scanners automatically identify network signals by demodulating/decoding radio frequency (RF) signals. The need for detection across multiple channels in a broad spectrum results in a high latency. In this chapter, the use of ELM shape-based networks is proposed to identify the PSD measurements of cellular signals belonging to various cellular technologies, namely the universal mobile telecommunications service (UMTS), global system for mobile communications (GSM), and long-term evolution (LTE) system. According to the knowledge of the authors, this is the first proposal of an ELM framework to identify real cellular signal PSD measurements that can be readily applied to real systems. The following contributions are presented in this chapter:

- An ELM model to identify over-the-air PSD measurements automatically in real systems, specifically the GSM, UMTS, and LTE cellular signal types.

- Derivation and analysis of the training and computational complexities associated with the proposed ELM model that include training time, number of real multiplications, additions, and parameters necessary for the identification of cellular signals.

- Robustness assessment of the proposed ELM model against the change in datasets by utilizing two different datasets collected under different conditions.

- Comparison of the proposed ELM model against other existing in the literature in terms of its complexity and identification accuracy.

The chapter is divided as follows: Section 7.3 explains the proposed ELM and system model, Section 7.4 shows the computational complexity analysis, Section 7.5 discusses the experimental setup and numerical results, and Section 7.6 concludes the chapter.

7.3 Proposed Signal Identification Model
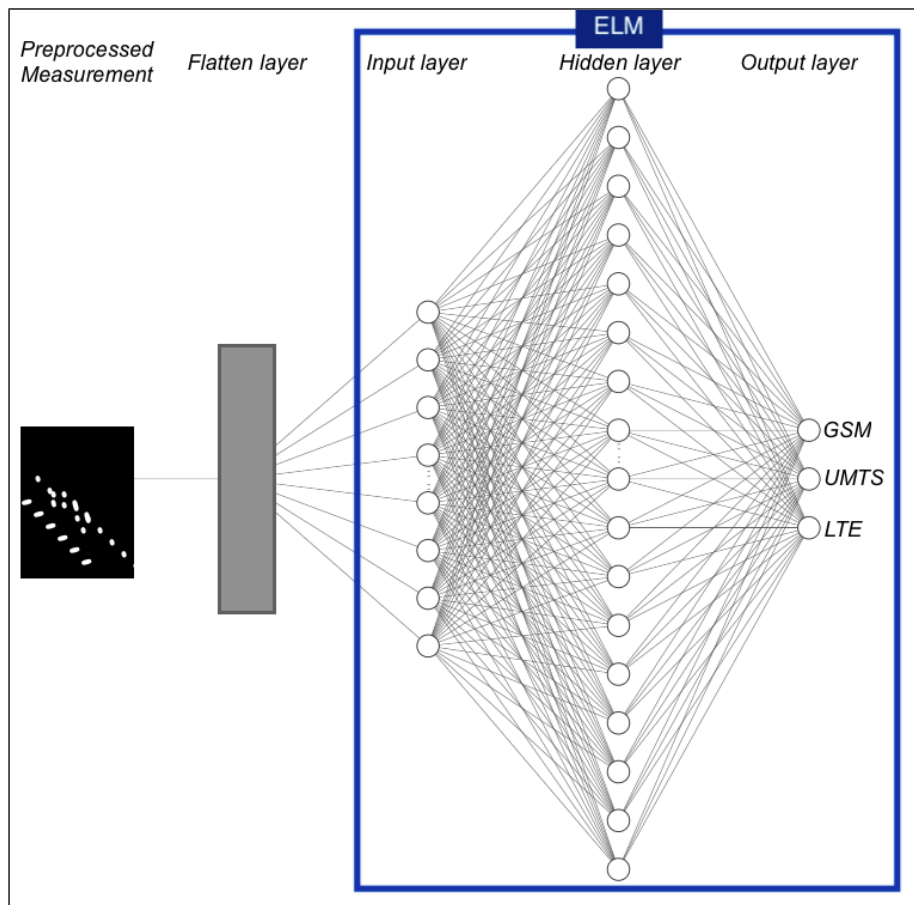
Fig. 7.1: Proposed ELM identification model.

7.3.1 Description of the ELM Model

The proposed ELM identification model is depicted in Fig. 7.1 and consists of three major stages: measurement acquisition, pre-processing, and ELM network processing. In the subsections that follow, I provide a detailed explanation of each stage.

7.3.2 Measurement Acquisition

Over-the-air PSD measurements are gathered from various frequency bands. Specifically, the PSD value in decibels (dB) at a given frequency bin f is denoted as m_f, where $m_f \in \mathbf{M}$. The vector $\mathbf{M}$ encompasses a single PSD measurement and is expressed as $\mathbf{M} = \{m_1, m_2, \ldots, m_F\}$, where F signifies the total count of frequency bins within a single measurement. The dataset is collected separately from each frequency band to train and test the NN identification model tailored to that band. The construction of each model relies on PSD measurements from the respective frequency band. This approach develops a unique ELM network for each frequency band, with distinct weights and biases.

Fig. 7.2 provides an illustrative excerpt from the 2100 MHz frequency band dataset. This graphical representation showcases distinct measurements acquired in the 2100 MHz band, which are samples from the larger collection of PSD measurements used to train and test the proposed ELM model tailored for that band.

7.3.3 PSD/2D Image Mapper

In this stage, an image is generated from each measured PSD using the following formula

$$\mathcal{I} = [p_{ab}]_{I_H \times I_W} , \tag{7.1}$$

where I_H represents the image height, I_W denotes the image width, and p_{ab} signifies the value assigned to the pixel located at coordinates (a, b) within the image $\mathcal{I}$. Since $\mathcal{I}$ is a 2D binary image, each p_{ab} assumes a binary state, either 1 or 0, based on the following criterion
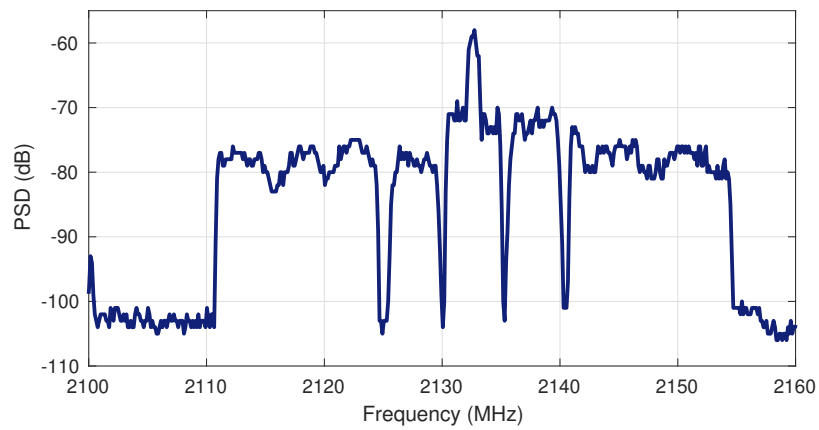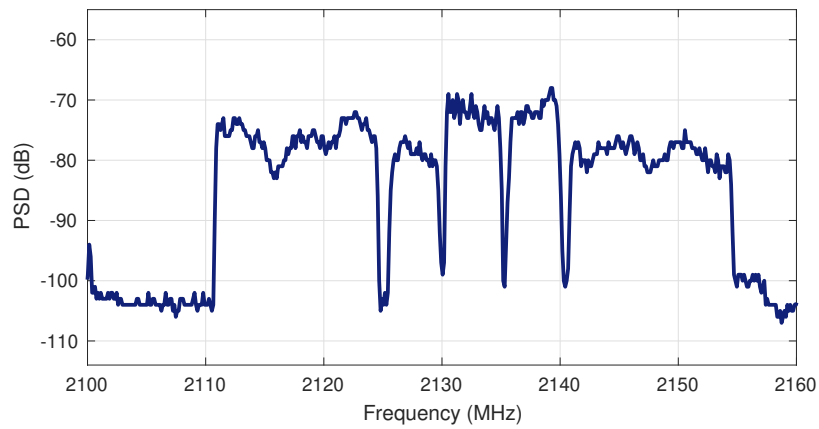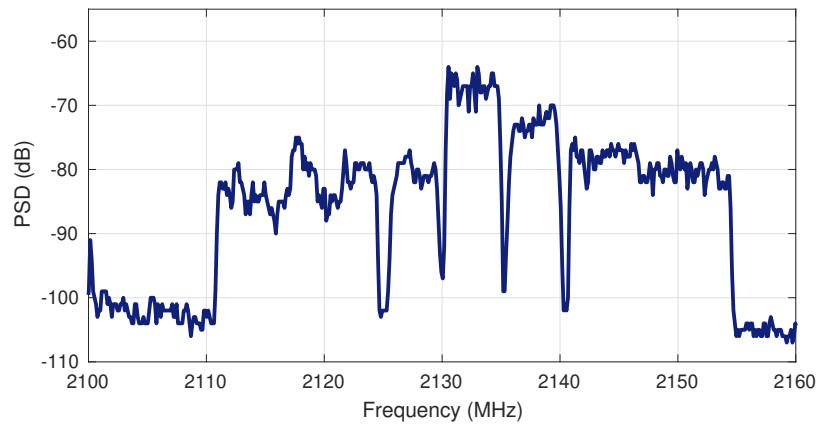
Fig. 7.2: PSD samples collected from 2100 MHz band.
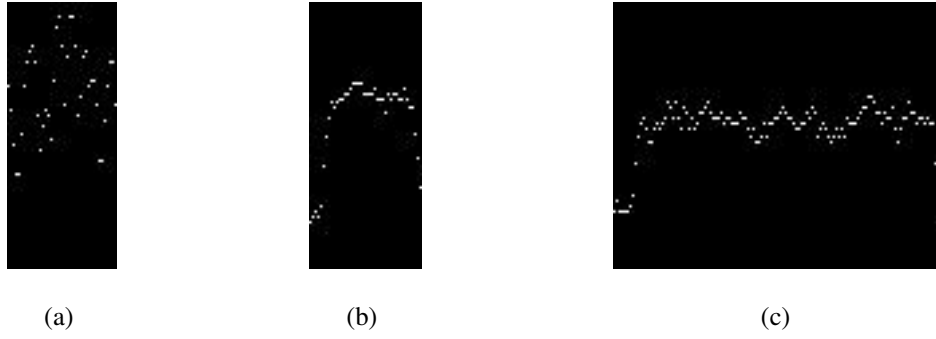
Fig. 7.3: Samples of $\mathcal{I}_s$ (a) GSM (b) UMTS (c) LTE.

$$p_{ab} = \begin{cases} 1, & \text{if } b = \left\lfloor \frac{I_H(m_a - \phi)}{\Phi - \phi} \right\rceil, & 1 \le a \le I_W. \\ \\ 0, & \text{otherwise} \end{cases} \tag{7.2}$$

In this context, m_a represents the PSD value at bin a, while Φ and ϕ denote the maximum and minimum measurements of the PSD, respectively. These are mathematically expressed as $\Phi = \max\limits_{1 \le a \le I_W} \{m_a\}$ and $\phi = \min\limits_{1 \le a \le I_W} \{m_a\}$. I_H is set to 100, and I_W is assigned the value F for all PSDs. All fractional numbers are rounded to the nearest integer value using the $\lfloor \cdot \rceil$ function. By applying this process to each PSD measurement within the acquired dataset, an image is systematically derived to represent each individual PSD measurement comprehensively.

7.3.4 Data Preprocessing

This subsection explains the process of extracting signal images from PSD measurement images. Let S denote the number of signals occupying a single PSD measurement. Consequently, from each PSD measurement, S distinct images are extracted, each representing one of the S signals. Each signal image, denoted by $\mathcal{I}_s$, is defined as follows:

$$\mathcal{I}_s = [p_{ac}]_{I_{sH} \times I_{sW}}, \forall s = 1, .., S. \tag{7.3}$$

Here, I_{sH} is selected to be equal to I_H, implying that the full image height is extracted from image

$\mathcal{I}$, and I_{sW} represents the horizontal span of the desired signal. In this chapter, the horizontal span is determined based on automatic channel detection decisions provided by the R&S® ROMES software [25].

Each PSD measurement is transformed into S labeled 2D binary (black and white) images, depicting discrete PSD measurements of individual cellular signals and corresponding labels. A sample of these input 2D binary images is depicted in Fig. 7.3. All these images from all PSDs are then gathered for input to the proposed ELM network. All the input 2D images need to have a standard height and width; this resizing process involves upscaling or downscaling the dimensions of I_{sW} and I_{sH} using bicubic interpolation. Since the dimensions of the input images substantially affect the computational complexity and classification accuracy of the proposed ELM model, they are amongst the finely tuned hyperparameters. It is essential to emphasize that because it is implausible to assume prior knowledge of spectrum allocation for ad-hoc deployments, the proposed ELM model does not use the occupied frequency bins and bandwidths as input data.

7.3.5 Proposed Extreme Learning Machine (ELM) Model

ELMs are a novel type of NN with distinct characteristics compared to conventional NNs. ELMs are single-hidden layer feedforward NN algorithms for supervised learning proposed in [24]. ELM is adequate for various tasks, including regression, classification, and clustering [26]. In this section, the ELM methodology is elucidated.

7.3.6 Architecture of ELM

ELMs have gained prominence in machine learning due to their distinctive architecture and efficient learning capabilities. This section shows the structural elements that differentiate them from conventional NNs. Central to the design of ELMs is a three-tiered architectural framework comprising the input layer, fully connected hidden layer, and output layer [20], [21]. Each layer serves a pivotal role

in facilitating the network's operations, that is detailed as follows:

7.3.6.1 Input Layer

The input layer is the point of ingress for data. The network receives data as a feature vector conventionally denoted as $\mathbf{x}$. This vector embodies the attributes or features characterizing the input data, and its dimensionality symbolized as k, corresponds to the number of these distinctive features. The primary responsibility of the input layer resides in preprocessing and normalizing the incoming data, ensuring it is optimally conditioned for subsequent processing stages.

7.3.6.2 Hidden Layer

The hidden layer serves as the central component in the ELM architecture, acting as the focal point of computational operations. An array of hidden neurons populates this tier, each endowed with independently and randomly initialized weights and biases [20], [21]. The weight matrix, $\mathbf{W}$, is the intermediary, establishing connections between the input layer and these hidden neurons; $\mathbf{W} \in \mathbb{R}$ $\{k \times j\}$, wherein j represents the number of hidden neurons. The output of the hidden layer, $\mathbf{H}$, is expressed as

$$\mathbf{H} = \sigma(\mathbf{x}\mathbf{W} + \zeta), \tag{7.4}$$

where ζ represents the biases intrinsic to each hidden neuron, while σ delineates an activation function applied element-wise to the input. The hidden layer is highly regarded for its capability to capture intricate data patterns and representations with enhanced computational efficiency.

7.3.6.3 Output Layer

The final layer in the ELM architectural framework is the output layer, where predictions are generated based on the information assimilated and processed within the hidden layer. In contrast to the hidden layer, wherein weights are randomly initialized, the output layer features weights calibrated during the

training regimen. For regression tasks, wherein the primary objective is the estimation of continuous values, the target outputs are denoted as $\mathbf{Y}$. In scenarios demanding classification, entailing the categorization of input data into discrete classes, $\mathbf{Y} \in \mathbb{R} \{j \times d\}$, where d conveys the number of output neurons. The derivation of output predictions, denoted as $\mathbf{O}$, is expressed as

$$\mathbf{O} = \mathbf{H}\gamma. \tag{7.5}$$

Herein, γ embodies the weight coefficients connecting the hidden and output layers. These weights undergo dynamic adjustments during the training stage, wherein the cardinal aspiration minimizes prediction errors, enhancing the model's predictive accuracy.

7.3.6.4 Training and Weight Calculation

In machine learning, ELMs stand out as a unique and efficient paradigm, notably for their unconventional approach to weight assignment and training. This subsection delves into the intricate details of the ELMs' training process and weight calculation, elucidating the reasons behind their distinctive characteristics.

- Distinctive Weight Initialization

  ELMs fundamentally differ from traditional NNs in their weight initialization strategy. Rather than iteratively fine-tuning weights and biases between the input and hidden layers, ELMs opt for a radically different approach: random weight assignment. This departure from convention is a hallmark of ELMs and underpins their efficiency.

  The motivation behind random weight assignment is to expedite the learning process and enhance convergence. In contrast to traditional NNs, where weights are meticulously adjusted during training, ELMs delegate the initial weight assignment to randomness. This strategy dramatically reduces the computational burden typically associated with weight fine-tuning, enabling ELMs to process data swiftly.

- Learning the output layer weights

  While ELMs embrace randomization in the input-to-hidden layer connections, they are not entirely devoid of learning. The essence of learning in the ELMs lies in determining the optimal output layer weights, γ. These weights are the key to translating the representations learned in the hidden layer into meaningful predictions.

  To find the optimal γ, ELMs employ a linear regression technique. The objective is to minimize the disparity between the predicted outputs $\mathbf{O}$ and desired outputs $\mathbf{Y}$. This process is akin to fitting a linear model that best captures the relationship between the hidden layer's activation and the target outputs. The linear regression problem can be formulated as

  $$\gamma = \mathbf{H}^\dagger \mathbf{Y}, \tag{7.6}$$

  where $\mathbf{H}^\dagger$ represents the pseudoinverse of the hidden layer matrix $\mathbf{H}$. The pseudoinverse is a mathematical construct that provides a least-squares solution to the linear regression problem. It enables the efficient calculation of γ without the need for backpropagation optimization algorithms, even for high-dimensional datasets.

The architectural design of ELMs embodies simplicity, rapid convergence, and an effective learning process. This unconventional NN framework, marked by the utilization of randomly assigned weights in the hidden layer and a linear regression-based approach for output layer training, has positioned ELMs as powerful tools across various domains within the field of machine learning. ELM's distinctive approach to machine learning comes with its own set of advantages, including:

1. **Rapid Training Process:** One of the primary advantages of the ELMs is their speed in the training phase. The random weight initialization and the use of linear regression for output layer weight calculation allow ELMs to train significantly faster than traditional NNs. This speed is particularly advantageous when dealing with real-time large datasets applications.

2. **Efficiency:** ELMs are highly efficient regarding computational resources. The utilization of the Moore-Penrose pseudoinverse for calculating output layer weights eliminates the need for iterative optimization algorithms, making ELMs well-suited for high-dimensional datasets.

3. **Simplicity:** ELMs have a simple architecture since they contain a single feedforward hidden layer. Thus, they are easy to implement and require minimal hyperparameter tuning, making them accessible to both researchers and practitioners in the field of machine learning.

4. **Generalization:** ELMs often exhibit good generalization performance, which means they can perform well on unseen datasets. This is especially valuable in scenarios where the availability of labelled datasets is limited.

5. **Robustness:** ELMs are robust to noisy datasets and can handle situations where the hidden layer may not be full rank. This robustness is a result of the pseudoinverse-based approach of the weight calculation.

7.4 Computational Complexity Analysis of the Proposed ELM

In the realm of ML, a fundamental aspect of assessing the suitability of a model for practical applications is understanding its computational complexity. This evaluation provides insights into the computational demands, resource requirements, and efficiency of the model. In the case of the proposed ELM, the computational complexity is assessed by examining parameters such as the number of weights and biases C_P, the total number of real multiplications C_M, and the overall number of real additions C_A.

7.4.1 Parameter Complexity (C_P)

The parameter complexity, denoted as C_P, considers the total number of weights and biases involved in the ELM network. These weights and biases are crucial elements of the NN complexity as they

determine the ability of the model to capture and represent complex relationships within the dataset. In the proposed ELM, C_P can be given as

$$C_P = \sum_{i=1}^{N} (\eta_i + 1)\eta_{i+1}, \tag{7.7}$$

where η_i represents the number of neurons in the i-th layer of the ELM network. The term $(\eta_i + 1)\eta_{i+1}$ signifies the product of the number of neurons in layers i and $i + 1$. The summation extends over all layers of the ELM, including the input and output layers. In the context of an ELM model, the value of N is equal to 3.

7.4.2 Real Multiplication Complexity (C_M)

The multiplication count, represented as C_M, quantifies the total number of real multiplications carried out during the execution of the ELM network. Multiplications are computationally expensive operations, and their count is an essential factor in assessing the computing time complexity of the model. To compute C_M, a similar principle is applied as in C_P as

$$C_M = \sum_{i=1}^{N} \eta_i \eta_{i+1}. \tag{7.8}$$

7.4.3 Real Addition Complexity (C_A)

The addition complexity, denoted as C_A, provides insights into the total number of real additions performed in the ELM network. While additions are generally less computationally intensive than multiplications, they still contribute to the overall time complexity of the proposed ELM model. The formula for C_A encompasses two components: First, it includes the sum of products of the number of neurons in each layer i and the number of neurons in the subsequent layer $i + 1$. Second, it accounts for the sum of neurons in the subsequent layer $i + 1$. Thus, C_A can be given as

$$C_A = \sum_{i=1}^{N} \eta_i \eta_{i+1} + \sum_{i=1}^{N} \eta_{i+1}. \tag{7.9}$$

The complexity metrics (i.e., C_P, C_M, and C_A) offer a comprehensive evaluation of the computational demands and efficiency of the proposed ELM model. C_P provides insights into the memory requirements, while C_M and C_A reflect the computational time and hardware cost for the NN operations.

7.5 Experimental Setup and Numerical Results

In this section, the designated hyperparameters of the proposed ELM model are presented, accompanied by an examination of the impact of varying the neurons within the proposed ELM model on identification accuracy. The evaluation of the proposed ELM model is conducted with respect to the identification accuracy on two datasets, referred to as DS1 and DS2. Additionally, the efficacy of the ELM model is substantiated through a comparative analysis with the most accurate findings in the existing literature.

7.5.1 Experimental Setup

A proprietary software-defined radio receiver is employed to collect over-the-air PSD measurements. This receiver operates in the 20–6000 MHz region and can pick up RF signals with a spur-free dynamic range of 70 dB and a noise figure of 10 dB. 100 MHz is the instantaneous capture bandwidth. Prior to being filtered to a 100 MHz bandwidth, the gathered frequency bands undergo band-pass filtering, followed by down-conversion to an intermediate frequency (IF). Each band has its own unique centre frequency.

Two independent datasets, DS1 and DS2, are collected. The two datasets were obtained under disparate conditions due to being collected several years apart. Consequently, they represent two entirely distinct datasets, albeit encompassing the same frequency bands. For DS1, the data collection is com-

piled from four separate bands of frequencies that are used in various regions; these bands are numbered 1 through 4, and their corresponding frequencies are 900 MHz, 2100 MHz, 1900 MHz, and 850 MHz. Band 1 includes 104 PSD signal measurements of GSM and 78 PSD signal measurements of UMTS. Band 2 comprises 1662 PSD signal measurements of UMTS and 2493 PSD signal measurements of LTE. Band 3 encompasses 1652 LTE PSD signal measurements, 1652 PSD signal measurements of UMTS, and 825 PSD signal measurements of GSM. Band 4 includes 2793 PSD signal measurements of UMTS and 2793 PSD signal measurements of GSM. DS2 is available for bands 2-4, with band 2 containing 5696 UMTS PSD signal measurements and 8544 LTE PSD signal measurements, band 3 having 3454 LTE PSD signal measurements, 3454 UMTS PSD signal measurements, and 1727 GSM PSD signal measurements, and band 4 consisting of 2688 UMTS PSD signal measurements and 2688 GSM signal measurements. The acquired PSD signal measurements are utilized to build balanced training and testing datasets with 70% used for training and 30% assigned for testing. Subsequently, collected datasets are exported to ASCII (American standard code for information interchange) files for processing in MATLAB software. The processed PSD measurements are broken down into their individual cellular signals using MATLAB, in accordance with the procedure described in Section 7.3. After that, the images of the signal measurements are sent into a Python code that builds and evaluates the proposed ELM model.

By utilizing the R&S® TSME drive test scanner tool and ROMES software with its automated channel detection feature, accurate labels of PSD measurements of cellular signals across various cellular bands can be acquired for further applications in both training and testing scenarios of the proposed ELM model.

7.5.2   Proposed ELM Model Hyperparameters

The rectified linear unit (ReLU) activation function, denoted as σ, introduces non-linearity into the model, thereby enhancing its expressive capabilities. The selection of the input random distribution contributes to the model's ability to capture intricate data patterns and relationships effectively. In the
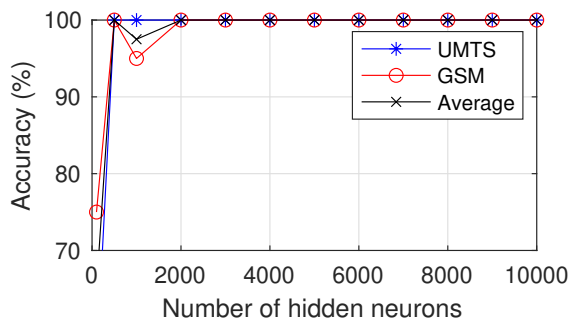
(a) Band 1
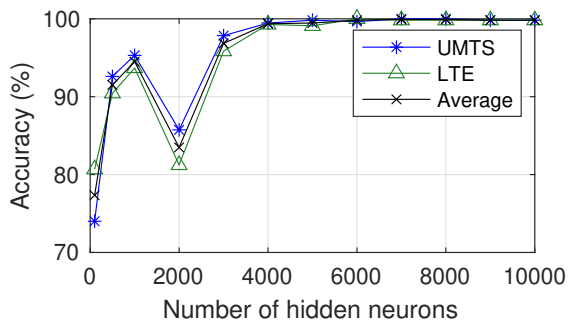
(b) Band 2
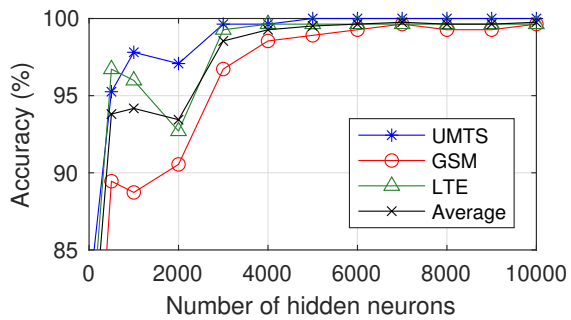
(c) Band 3
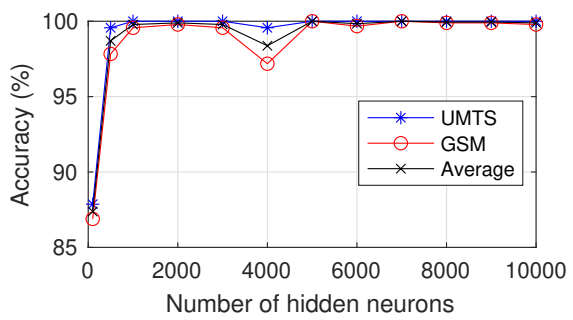
(d) Band 4

Fig. 7.4: The effect of varying the number of hidden neurons in DS1 on: (a) Band 1 (b) Band 2 (c) Band 3 (4) Band 4.

proposed ELM model, a Beta distribution with $\alpha = 1$ and $\beta = 3$ is chosen to initialize the weights and biases within the network. The dimensions of the input images are adjusted to be 100 by 30 pixels. It is noteworthy that the hyperparameters of the proposed ELM are exclusively optimized using the DS1 dataset. Subsequently, the DS2 dataset is employed to assess the generalization and robustness of the proposed ELM model under the conditions where the hyperparameters have been optimized using DS1.

The determination of the number of hidden neurons holds a pivotal role in shaping the capacity and learning capability of the ELM model. Treated as a hyperparameter, the number of hidden nodes undergoes meticulous tuning, allowing for the optimization of the overall performance of the ELM network. This tuning process aims to strike a balance between model complexity and the acquisition of generalization abilities. A detailed discussion on tuning the number of hidden neurons is presented in the following subsection.

7.5.3   Optimizing Hidden Neurons of the Proposed ELM Model

In this subsection, a systematic variation of the number of hidden neurons was executed to optimize the performance (i.e., the identification accuracy and computational complexity) of the proposed ELM model across different frequency bands within DS1.

Fig. 7.4 depicts the relation between the number of hidden neurons and the identification accuracy for each frequency band. Notably, for band 1, the identification accuracy reached 100% across all cellular signal types with the utilization of 500 hidden neurons. Regarding bands 2 and 3, the accuracy approached 100% when the number of hidden neurons reached approximately 4000, although satisfactory accuracy levels were maintained at around 1000 hidden neurons for both bands. Band 4 demonstrated stability at 1000 hidden neurons. In the proposed ELM model, a nuanced selection of 1130 hidden neurons was made through meticulous fine-tuning, aiming to achieve optimal accuracy with minimal complexity, considering the increment in the number of neurons.

7.5.4 Assessing the Proposed ELM Model using DS1: Hyperparameters' Selection Assessment

TABLE 7.1: Identification accuracy of the proposed ELM model DS1.

Band	Accuracy UMTS	Accuracy GSM	Accuracy LTE	Avg. accuracy
1	100%	100%	-	100%
2	99.7%	-	99.4%	99.6%
3	99.2%	99.6%	99.8%	99.6%
4	100%	100%	-	100%

Table 7.1 presents a comprehensive overview of the experimental findings derived from DS1 dataset using the proposed ELM model with hyperparameters optimized based on DS1. The table offers detailed insights into the average identification accuracy percentages for UMTS, GSM, and LTE cellular signals. The proposed ELM model attains an identification accuracy of 100% for bands 1 and 4. Bands 2 and 3 consistently exhibit near-perfect identification accuracy percentages, consistently surpassing 99.2%. The proposed ELM model demonstrates exceptional accuracy, achieving 99.9%, 99.7%, and 99.6% identification accuracy for GSM, UMTS, and LTE, respectively. The outcomes obtained from the proposed ELM model underscore its efficacy in discerning various cellular communication technologies.

To visualize the proposed ELM model's performance, Fig. 7.5 presents the confusion matrices across all frequency bands. A confusion matrix succinctly evaluates the accuracy and error characteristics of a classification model by quantifying true positives, true negatives, false positives, and false negatives. It serves as a pivotal tool for assessing the proficiency of the proposed model in distinguishing distinct classes within a dataset. The results indicate that the proposed ELM model achieves a perfect confusion matrix with negligible occurrences of false negatives and false positives, accurately

(a) Band 1

(b) Band 2

(c) Band 3

(d) Band 4
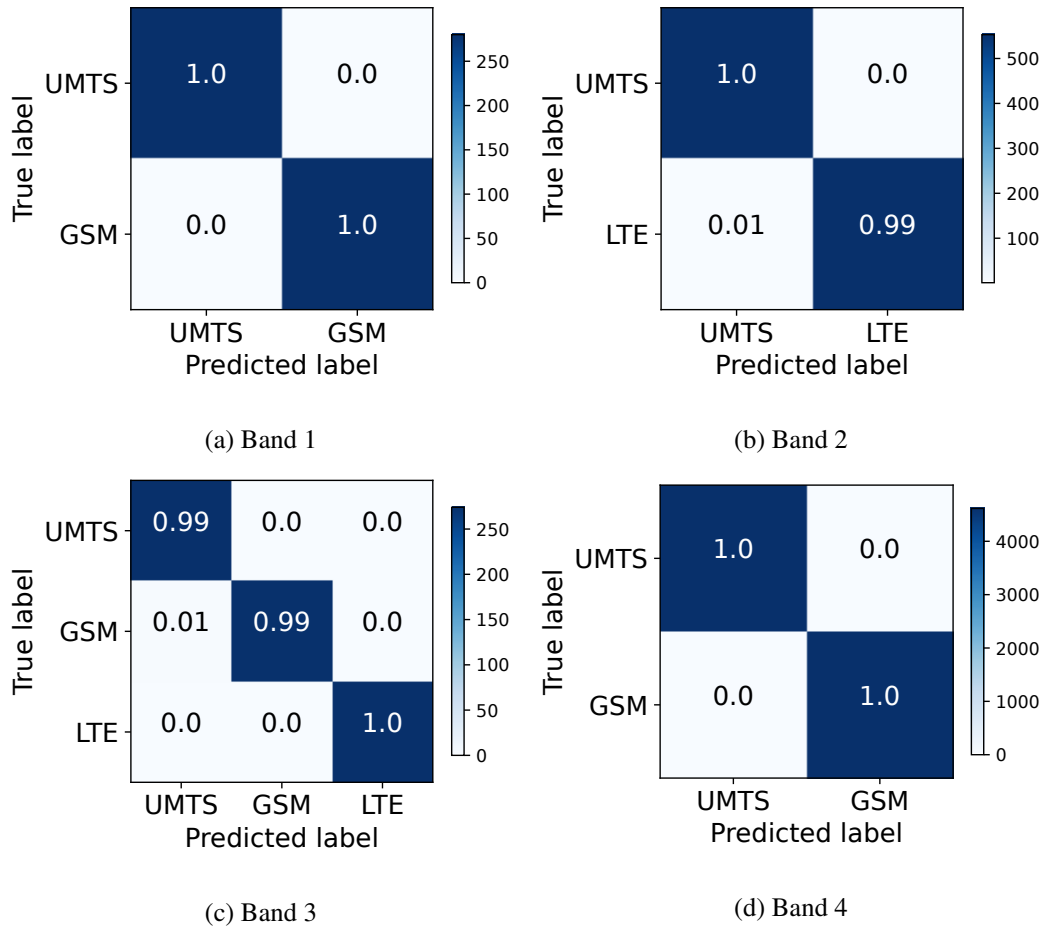
Fig. 7.5: Normalized confusion matrices for different bands in DS1.

identifying all true positives and true negatives.

7.5.5 Assessing the Proposed ELM Model using DS2: Generalization and Robustness Assessment

To further assess the generality and robustness of the proposed ELM model, the same model is applied, without re-tuning, to an unseen DS2 dataset. It is crucial to emphasize that the DS1 and DS2 datasets were obtained under distinct conditions, as mentioned previously. The identification accuracy results are summarized in Table 7.2. Remarkably, when the dataset was utilized in conjunction with the generalized ELM model structure, all cellular technologies achieved an average identification accuracy exceeding of 92%. The minimum identification accuracy achieved is 90.1% for UMTS in band 3.

Fig. 7.6 displays the confusion matrix of the proposed ELM model for DS2. The confusion matrix reveals that GSM is never confused with LTE, and vice versa. Furthermore, it indicates that any confusion that occurs is minimal despite the proposed ELM model not being trained on this dataset at all. This outcome underscores the model's capability to maintain high identification accuracy even in situations where stationary data collection is not feasible, and fine-tuning the proposed ELM model for specific scenarios is not a possibility. These results demonstrate the robustness and practical applicability of the proposed ELM algorithm in real-world wireless communication systems.

TABLE 7.2: Identification accuracy ELM for DS2.

Band	Accuracy UMTS	Accuracy GSM	Accuracy LTE	Avg. accuracy
2	96.6%	-	96.3%	96.5%
3	90.1%	90.9%	97.4%	92.8%
4	98.8%	91.1%	-	94.9%

7.5.6   Assessing the Proposed ELM Model Compared to Literature

In the existing literature, a hybrid convolutional feedforward neural network (HCFNN) model was introduced in [16] as a solution for identifying GSM, UMTS, and LTE cellular signals from images. The HCFNN model represents a hybrid architecture incorporating multiple convolutional layers and a feedforward neural network. Maxpooling and dropout techniques are also applied within the network. The identification accuracy of the HCFNN model was benchmarked against several earlier works in the literature, including [6] and [15]. The HCFNN model demonstrated its superiority over other proposed models in the literature. A comparative analysis of the performance of the proposed ELM model with the HCFNN model [16], reported as one of the most efficient and accurate models in the literature, is conducted in this section.

Fig. 7.7(a) visually illustrates the comparison of identification accuracy between the proposed ELM
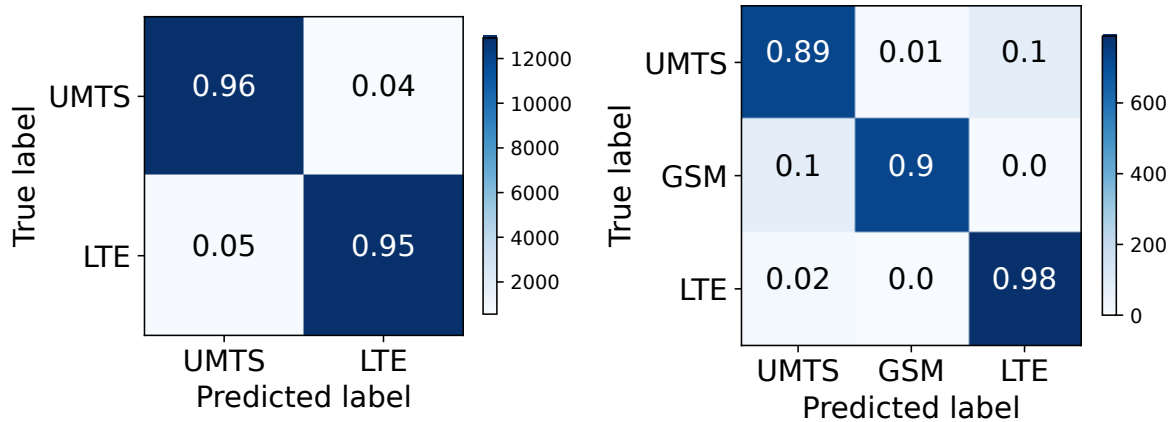
(a) Band 2

(b) Band 3
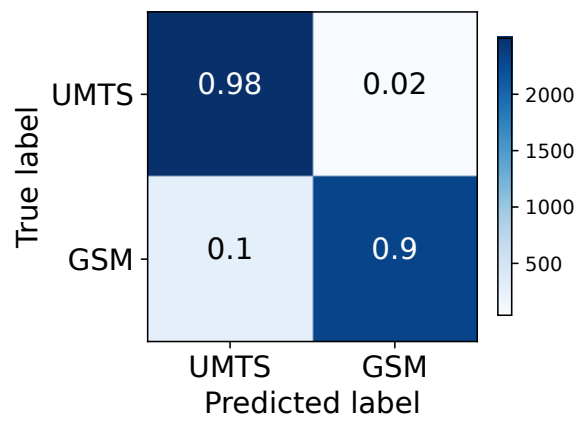
(c) Band 4

Fig. 7.6: Normalized confusion matrices for different bands in DS2.
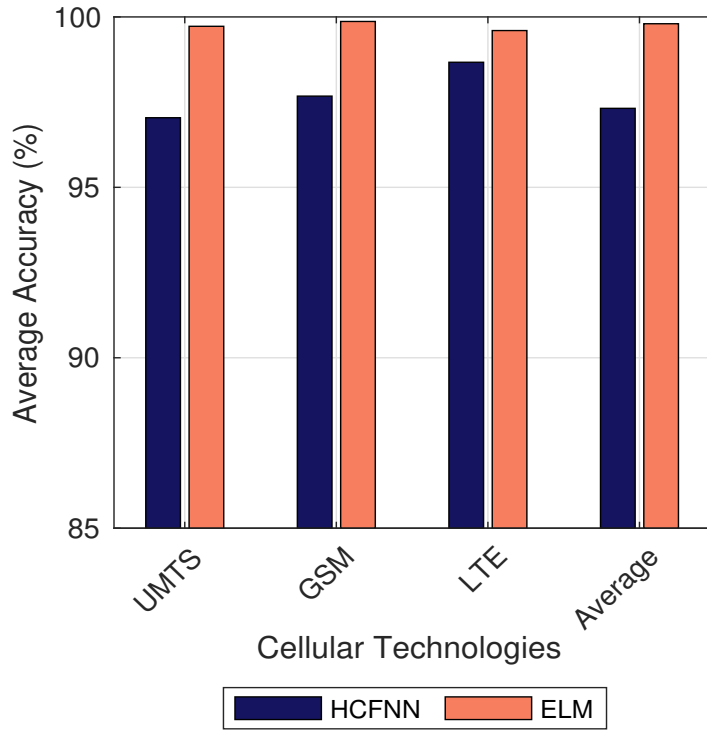
(a) DS1
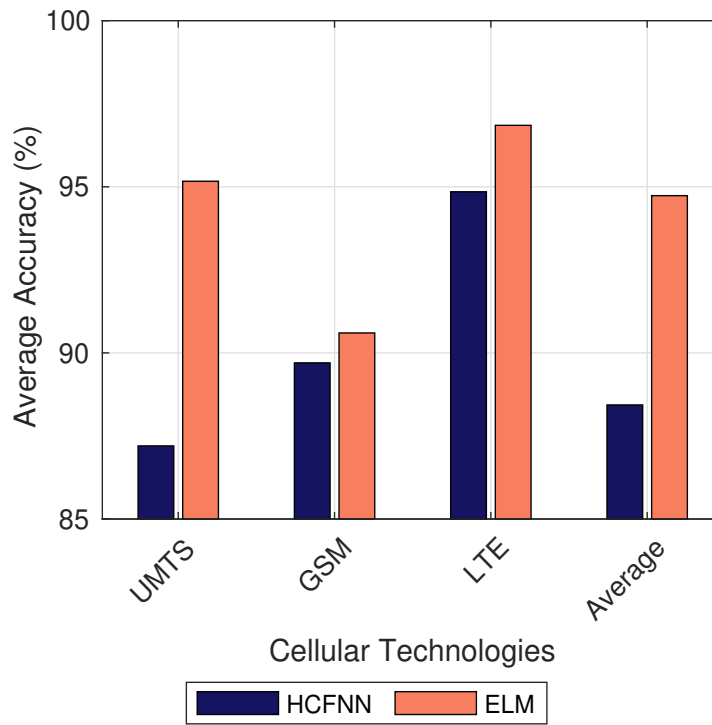
(b) DS2

Fig. 7.7: Comparison between identification accuracy of the proposed ELM model and HCFNN [16].

model and the HCFNN model in [16], focusing on the accuracy of identifying cellular PSD measurements in the DS1 dataset. This figure demonstrates that the proposed ELM model consistently achieves superior identification accuracy across different cellular technologies. Specifically, the proposed ELM outperforms HCFNN with an improvement in the identification accuracy of 3%, 2%, and 1% for UMTS, GSM, and LTE, respectively, resulting in an average accuracy improvement of 2%. Fig. 7.7(b) further reveals that the HCFNN model encounters challenges when identifying cellular technologies with the unseen dataset of DS2. In this context, the proposed ELM model's accuracy improvement over the HCFNN model increases to 8%, 1%, and 3% for UMTS, GSM, and LTE, respectively, providing an average accuracy improvement of 4%. In conclusion, Fig. 7.7 highlights that the proposed ELM model not only exhibits better identification accuracy compared to the most efficient model in the literature but also demonstrates enhanced robustness and generalization capabilities for unseen datasets.

The comparison of the complexity between the proposed ELM model and the HCFNN model in [16] is presented in Fig. 7.8. The complexity assessment is divided into two components: the time complexity consumed in the training phase (i.e., the time to learn the neural network model), and the complexity cost for the testing phase (i.e., C_P, C_M, and C_A as in (7.7)-(7.9)). As depicted in Fig. 7.8(a), the training time complexity of the proposed ELM is 7.5 times less than the training complexity of the HCFNN. For the testing complexity cost, the proposed ELM model exhibits similar values to HCFNN for C_M and C_A, but it shows a higher number of required parameters, C_P, as shown in Fig. 7.8(b).

In light of this comparative analysis, it becomes evident that the proposed ELM model consistently outperforms the HCFNN model across different situations, offering superior identification accuracy and significantly reduced training time, albeit with a slight increase in the number of stored parameters required for testing.
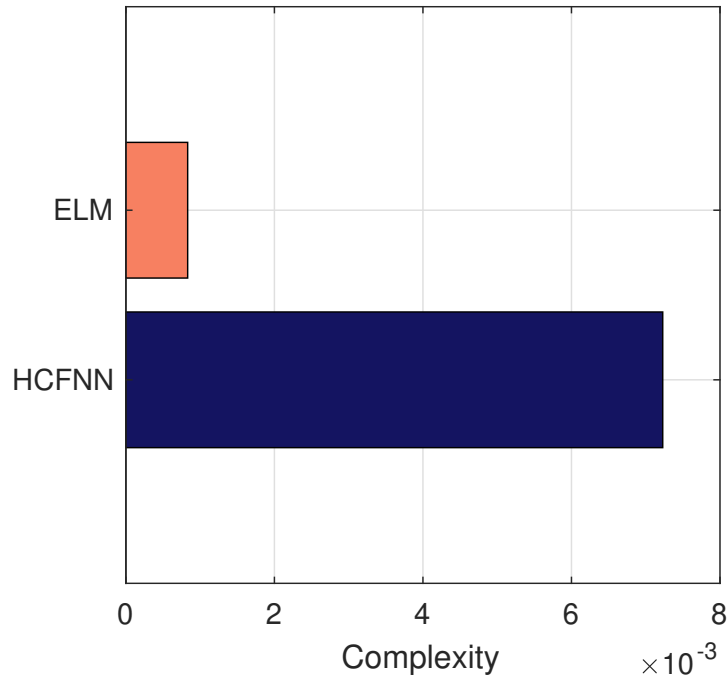
(a) Training time complexity
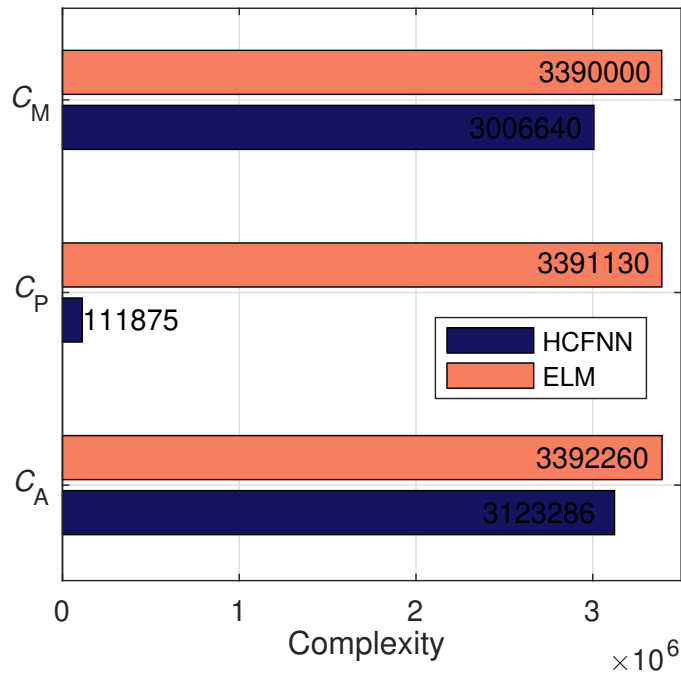
(b) Testing complexity cost

Fig. 7.8: Complexity comparison between the proposed ELM model and HCFNN [16].

7.6 Conclusion

In response to the escalating demand for efficient spectrum utilization due to the proliferation of wireless devices, this study proposes an ELM model for the identification of real PSD measurements in cellular systems, including LTE, UMTS, and GSM. The hyperparameters of the ELM model are rigorously optimized using the DS1 dataset, while the unexplored DS2 dataset is employed to assess the model's robustness and generality. An evaluation based on the derived complexity cost and experimental results demonstrates the proposed ELM model's remarkable performance, achieving nearly 100% identification accuracy for all cellular signal types. Additionally, the proposed ELM model undergoes a comparative analysis with the most efficient model in the literature, namely the HCFNN model. This comparison encompasses both DS1 and DS2 datasets, with DS1 contributing to the model's development and DS2 representing an unseen dataset. Remarkably, the proposed ELM model, with a training time complexity 7.5 times less than the HCFNN model, exhibits notable superiority across all cellular technologies, yielding an improvement in the identification accuracy ranging from 1% to 8%.

References

[1] Y. A. Eldemerdash, O. A. Dobre, O. Üreten, and T. Yensen, "Identification of cellular networks for intelligent radio measurements," *IEEE Trans. Instrum. Meas.*, vol. 66, no. 8, pp. 2204–2211, Aug. 2017.

[2] ——, "Fast and robust identification of GSM and LTE signals," in *Proc. IEEE Int. Instrum. Meas. Technol. Conf.*, 2017, pp. 1–6.

[3] F. Hameed, O. A. Dobre, and D. C. Popescu, "On the likelihood-based approach to modulation classification," *IEEE Trans. Wireless Commun.*, vol. 8, no. 12, pp. 5884–5892, Dec. 2009.

[4] E. Karami, O. A. Dobre, and N. Adnani, "Identification of GSM and LTE signals using their second-order cyclostationarity," in *Proc. IEEE Int. Instrum. Meas. Technol. Conf.*, 2015, pp. 1108–1112.

[5] O. A. Dobre, "Signal identification for emerging intelligent radios: classical problems and new challenges," *IEEE Instrum. Meas. Mag.*, vol. 18, no. 2, pp. 11–18, Apr. 2015.

[6] E. A. Makled, A. A. Al-Habob, O. A. Dobre, and O. Üreten, "Detection and identification of mobile network signals," *IEEE Trans. Instrum. Meas.*, vol. 70, pp. 1–4, Sept. 2021.

[7] D. Grimaldi, S. Rapuano, and L. De Vito, "An automatic digital modulation classifier for measurement on telecommunication networks," *IEEE Trans. Instrum. Meas.*, vol. 56, no. 5, pp. 1711–1720, Oct 2007.

[8] H. Agirman-Tosun, Y. Liu, A. Haimovich, O. Simeone, W. Su, J. Dabin, and E. Kanterakis, "Modulation classification of mimo-ofdm signals by independent component analysis and support vector machines," in *Proc. Conf. Record of the Forty Fifth Asilomar Conf. on Signals, Systems and Computers*, 2011, pp. 1903–1907.

[9] F. Xing, D. Xu, W. Xu, and H. Wang, "A modulation recognition algorithm of communication signals and implementation based on digital signal processor," in *Proc. IEEE MTT-S Int. Wireless Symposium*, 2021, pp. 1–3.

[10] M. D. Wong, S. K. Ting, and A. K. Nandi, "Naive bayes classification of adaptive broadband wireless modulation schemes with higher order cumulants," in *Proc. 2nd Int. Conf. on Signal Process. and Commun. Syst.*, 2008, pp. 1–5.

[11] X. Li, F. Dong, S. Zhang, and W. Guo, "A survey on deep learning techniques in wireless signal recognition," *Wireless Communications and Mobile Computing*, vol. 2019, pp. 1–12, Feb. 2019.

[12] H. Xia, K. Alshathri, V. B. Lawrence, Y.-D. Yao, A. Montalvo, M. Rauchwerk, and R. Cupo, "Cellular signal identification using convolutional neural networks: AWGN and rayleigh fading channels," in *Proc. IEEE Int. Symposium on Dynamic Spectrum Access Networks*, 2019, pp. 1–5.

[13] M. D. Wong and A. K. Nandi, "Automatic digital modulation recognition using spectral and statistical features with multi-layer perceptrons," in *Proc. Sixth Int. Symposium on Signal Processing and its Applications*, vol. 2, 2001, pp. 390–393.

[14] A. K. Nandi and E. E. Azzouz, "Algorithms for automatic modulation recognition of communication signals," *IEEE Trans. Commun.*, vol. 46, no. 4, pp. 431–436, Apr. 1998.

[15] E. A. Makled, I. Al-Nahhal, O. A. Dobre, and O. Üreten, "Identification of cellular signal measurements using machine learning," *IEEE Trans. Instrum. Measur.*, vol. 72, pp. 1–4, Jan. 2023.

[16] E. A. Makled, I. Al-Nahhal, O. A. Dobre, O. Üreten, and H. Shin, "Identification of cellular measurements: A neural network approach," *IEEE Trans. Instrum. Measur.*, vol. 73, pp. 1–12, Oct. 2023.

[17] U. Markowska-Kaczmar and M. Kosturek, "Extreme learning machine versus classical feedforward network," *Neural Computing and Applications*, vol. 33, no. 22, pp. 15 121–15 144, Aug. 2021.

[18] Y.-H. Pao, S. M. Phillips, and D. J. Sobajic, "Neural-net computing and the intelligent control of systems," *International Journal of Control*, vol. 56, no. 2, pp. 263–289, Mar. 1992.

[19] Y.-H. Pao, G.-H. Park, and D. J. Sobajic, "Learning and generalization characteristics of the random vector functional-link net," *Neurocomputing*, vol. 6, no. 2, pp. 163–180, Apr. 1994.

[20] M. Ganaie, M. Tanveer, and P. N. Suganthan, "Minimum variance embedded random vector functional link network," in *Proc. International Conference on Neural Information Processing*. Springer, Nov. 2020, pp. 412–419.

[21] L. Zhang and P. N. Suganthan, "A comprehensive evaluation of random vector functional link networks," *Information Sciences*, vol. 367, pp. 1094–1105, Nov. 2016.

[22] G.-B. Huang, Q.-Y. Zhu, and C.-K. Siew, "Extreme learning machine: a new learning scheme of feedforward neural networks," in *Proc. IEEE international joint conference on neural networks (IEEE Cat. No. 04CH37541)*, vol. 2, 2004, pp. 985–990.

[23] W. Cao, X. Wang, Z. Ming, and J. Gao, "A review on neural networks with random weights," *Neurocomputing*, vol. 275, pp. 278–287, Jan. 2018.

[24] G.-B. Huang, Q.-Y. Zhu, and C.-K. Siew, "Extreme learning machine: theory and applications," *Neurocomputing*, vol. 70, no. 1-3, pp. 489–501, Dec. 2006.

[25] Rohde & Schwartz, "R&S® ROMES4 drive test software," Apr. 2021.

[26] G.-B. Huang, H. Zhou, X. Ding, and R. Zhang, "Extreme learning machine for regression and multiclass classification," *IEEE Trans. Syst., Man, Cybern. B, Cybern)*, vol. 42, no. 2, pp. 513–529, Oct. 2011.

Chapter 8

Conclusion and Future Research

In this chapter, the contributions of this thesis are presented and several potential directions for future research are discussed.

8.1   Contributions

This work focused on improving the performance of UWA networks and terrestrial networks through using advanced techniques. In Chapters 2 and 3, the integration of FD and NOMA into a UWA network is studied. Specifically, in Chapter 2, FD and NOMA were applied on a UWA, and mathematical optimization was used to maximize the sum rate and energy efficiency. Specifically, in Chapter 3, the effect of a cyber attack by an Eve on an UWA system was explored when applying FD and NOMA. Two scenarios were analyzed: Eve's CI was known and unknown. A power allocation problem optimized the secrecy sum rate, highlighting the system resilience against Eve's attacks.

In Chapters 4-7, cellular network signal identification from over-the-air measurements is studied. The terrestrial communication technologies in the study were GSM, UMTS, and LTE. Specifically, in Chapter 4, two algorithms were proposed, namely a signal detection algorithm and a signal identification algorithm. The signal detection algorithm detects 100% of the signals in the data set, and the identification algorithm identifies more than 90% of the signals with their correct types. Chapters 5-7

174

focused on using different ML models to identify cellular signals. The acquisition models utilized for the data fall into two categories: in-band (IB) PSD and multi-band (MB) PSD. In the IB approach, the data employed for model training and testing originates from a single band. On the other hand, in the MB approach, the data used for training and testing was gathered from multiple bands. Chapter 5 used a feedforward neural network to identify whether a measured signal belongs to a specific cellular type. The identification accuracy was above 94% for all scenarios. In Chapter 6, the proposed hybrid convolutional feedforward neural network model was used to identify the measured signals with an accuracy above 92% for IB-PSD scenarios and above 99.5% for MB-PSD scenarios. In Chapter 7, ELM was applied to improve the average identification accuracy of IB-PSD to 99.9% 99.7% and 99.6% for GSM, UMTS, and LTE, respectively. Also, the ELM model proved to be more robust against measurement changes.

8.2   Potential Avenues for Future Research

In this thesis, enhancement of the spectral efficiency and security aspects across various strata of forthcoming 6G networks are examined. The research presented herein serves as a foundation for prospective investigations, pointing toward several promising directions:

- Enhanced Underwater Network Modeling: The current underwater network model can be further enriched by incorporating more sensors and robotic arms. This augmentation extends the model's reach and coverage, enhancing its effectiveness in capturing underwater data and facilitating a broader range of real-world applications.

  The current underwater network model can be further enriched by incorporating renewable energy sources to power sensor networks, enhancing their sustainability and autonomy. This addition expands the model's applicability to real-world scenarios by ensuring continuous power supply to underwater nodes, thereby increasing resilience and extending operational lifespan in remote or environmentally sensitive regions.

- Integration of Underwater Technologies: Explore the feasibility of integrating multiple underwater technologies. For instance, the potential synergy between acoustic links connecting relays and nodes and optical links between relays and buoys could be examined.

- Security Against Multi-Faceted Threats: Investigate the robustness of the underwater system against diverse security threats, such as multiple jammers and active eavesdroppers, to fortify its resilience in practical deployment.

- Integration with Unmanned Aerial Vehicles (UAVs): Assess the inclusion of UAVs in the network architecture, aiming to integrate underwater networks with terrestrial counterparts seamlessly.

- Power Optimization using Machine Learning: Optimize the sum rate and secrecy sum rate in relation to power consumption by leveraging advanced ML models, such as reinforcement learning tools.

- A more complicated model with code-domain NOMA and/or decode and forward relay can be studied.

- Expansion of Signal Identification: Broaden the scope of signal identification datasets by incorporating 5G signals, facilitating the adaptation of identification techniques for future network configurations.

- Different training and test data splits can be used to evaluate the algorithms in Chapters 5-7.

- The raw data from the PSD can be used without conversion to an image.

- Cross-Domain Signal Identification: Extend the signal identification methodologies developed for terrestrial communications to the domain of underwater signal processing, exploring their adaptability and effectiveness in diverse environments.

The directions mentioned above aim to build upon the foundations of this thesis, offering ample opportunities for further exploration and advancement in the realm of 6G network optimization and

security.

References

Chapter 1

[1] G. Wikström, J. Peisa, P. Rugeland, N. Johansson, S. Parkvall, M. Girnyk, G. Mildh, and I. L. Da Silva, "Challenges and technologies for 6G," *in Proc. 2nd 6G Wireless Summit (6G SUMMIT)*, 2020, pp. 1–5.

[2] M. Banafaa, I. Shayea, J. Din, M. H. Azmi, A. Alashbi, Y. I. Daradkeh, and A. Alhammadi, "6G mobile communication technology: Requirements, targets, applications, challenges, advantages, and opportunities," *Alexandria Engineering Journal*, vol. 64, pp. 245–274, Feb. 2023.

[3] K. David, J. Elmirghani, H. Haas, and X.-H. You, "Defining 6G: Challenges and opportunities [from the guest editors]," *IEEE Veh. Technol. Magazine*, vol. 14, no. 3, pp. 14–16, Aug. 2019.

[4] C. De Alwis, A. Kalla, Q.-V. Pham, P. Kumar, K. Dev, W.-J. Hwang, and M. Liyanage, "Survey on 6G frontiers: Trends, applications, requirements, technologies and future research," *IEEE Open J. of the Communs. Society*, vol. 2, pp. 836–886, Apr. 2021.

[5] Ericsson AB. Traffic exploration tool. Interactive online tool. Available at: http://www.ericsson.com/TET/trafficView/loadBasicEditor.ericsson.

[6] F. Tariq, M. R. Khandaker, K.-K. Wong, M. A. Imran, M. Bennis, and M. Debbah, "A speculative study on 6G," IEEE Wireless Communs., vol. 27, no. 4, pp. 118–125, Aug. 2020.

[7] M. Alsabah, M. A. Naser, B. M. Mahmmod, S. H. Abdulhussain, M. R. Eissa, A. Al-Baidhani, N. K. Noordin, S. M. Sait, K. A. Al-Utaibi, and F. Hashim, "6G wireless communications networks: A comprehensive survey," *IEEE Access*, vol. 9, pp. 148 191–148 243, Nov. 2021.

[8] W. Saad, M. Bennis, and M. Chen, "A vision of 6G wireless systems: Applications, trends, technologies, and open research problems," *IEEE Netw.*, vol. 34, no. 3, pp. 134–142, Oct. 2019.

[9] F. Fang, Y. Xu, Q.-V. Pham, and Z. Ding, "Energy-efficient design of irs-noma networks," *IEEE Trans. on Veh. Technol.*, vol. 69, no. 11, pp. 14 088–14 092, Sep. 2020.

[10] Y. Lu and X. Zheng, "6G: A survey on technologies, scenarios, challenges, and the related issues," *Journal of Industrial Information Integration*, vol. 19, p. 100158, Feb. 2020.

[11] Y. Liu, X. Yuan, Z. Xiong, J. Kang, X. Wang, and D. Niyato, "Federated learning for 6G communications: Challenges, methods, and future directions," *China Communications*, vol. 17, no. 9, pp. 105–118, Sep. 2020.

[12] P. Yang, Y. Xiao, M. Xiao, and S. Li, "6G wireless communications: Vision and potential techniques," *IEEE Netw.*, vol. 33, no. 4, pp. 70–75, Jul. 2019.

[13] Z. Zhang, Y. Xiao, Z. Ma, M. Xiao, Z. Ding, X. Lei, G. K. Karagiannidis, and P. Fan, "6G wireless networks: Vision, requirements, architecture, and key technologies," *IEEE Veh. Technol. magazine*, vol. 14, no. 3, pp. 28–41, Sep. 2019.

[14] J. Liu, Y. Shi, Z. M. Fadlullah, and N. Kato, "Space-air-ground integrated network: A survey," *IEEE Communs. Surveys Tuts.*, vol. 20, no. 4, pp. 2714–2741, May 2018.

[15] N.-N. Dao, N. H. Tu, T. T. Thanh, V. N. Q. Bao, W. Na, and S. Cho, "Neglected infrastructures for 6G—underwater communications: How mature are they?" *Journal of Network and Computer Applications*, vol. 213, p. 103595, Apr. 2023.

[16] A. Gkikopouli, G. Nikolakopoulos, and S. Manesis, "A survey on underwater wireless sensor networks and applications," in *in Proc. Mediterranean Conference on Control Automation, Barcelona, Spain*, 2012, pp. 1147–1154.

[17] C. Gussen, M. Campos, W. A. Martins, F. M. Costa, and J. N. Gois, "A survey of underwater wireless communication technologies," *J. Commun. Inf. Sys*, vol. 31, no. 1, pp. 242–255, Oct. 2016.

[18] M. Jouhari, K. Ibrahimi, H. Tembine, and J. Ben-Othman, "Underwater wireless sensor networks: A survey on enabling technologies, localization protocols, and internet of underwater things," *IEEE Access*, vol. 7, pp. 96 879–96 899, Jul. 2019.

[19] H. Luo, J. Wang, F. Bu, R. Ruby, K. Wu, and Z. Guo, "Recent progress of air/water cross-boundary communications for underwater sensor networks: A review," *IEEE Sensors J.*, vol. 22, no. 9, pp. 8360–8382, Mar. 2022.

[20] M. Series, "IMT vision–framework and overall objectives of the future development of IMT for 2020 and beyond," *Recommendation ITU*, vol. 2083, no. 0, 2015.

[21] A.-A. A. Boulogeorgos, A. Alexiou, T. Merkle, C. Schubert, R. Elschner, A. Katsiotis, P. Stavrianos, D. Kritharidis, P.-K. Chartsias, J. Kokkoniemi et al., "Terahertz technologies to deliver optical network quality of experience in wireless systems beyond 5g," *IEEE Communs. Magazine*, vol. 56, no. 6, pp. 144–151, Jun. 2018.

[22] S. Kisseleff, S. Chatzinotas, and B. Ottersten, "Reconfigurable intelligent surfaces in challenging environments: Underwater, underground, industrial and disaster," *IEEE Access*, vol. 9, pp. 150 214–150 233, Nov. 2021.

[23] E. A. Makled, A. Yadav, O. A. Dobre, and R. D. Haynes, "Hierarchical full-duplex underwater acoustic network: A NOMA approach," in *Proc. IEEE OCEANS, Charleston, SC, USA*, 2018, pp. 1–6.

[24] E. A. Makled and O. A. Dobre, "On the security of full-duplex relay-assisted underwater acoustic network with NOMA," *IEEE Trans. on Veh. Technol.*, vol. 71, no. 6, pp. 6255–6265, Mar. 2022.

[25] E. A. Makled, A. A. Al-Habob, O. A. Dobre, and O. Üreten, "Detection and identification of mobile network signals," *IEEE Trans. Instrum. Meas.*, vol. 70, pp. 1–4, Sep. 2021.

[26] E. A. Makled, I. Al-Nahhal, O. A. Dobre, and O. Üreten, "Identification of cellular signal measurements using machine learning," *IEEE Trans. Inst. and Meas.*, vol. 72, pp. 1–4, Jan. 2023.

[27] E. A. Makled, I. Al-Nahhal, O. A. Dobre, O. Üreten, and H. Shin, "Identification of cellular measurements: A neural network approach," *IEEE Trans. Instrum. Meas.*, vol. 73, pp. 1–12, Oct. 2023.

[28] E. A. Makled, I. Al-Nahhal, O. A. Dobre, O. Üreten, and H. Shin, "Identification of cellular signal measurements using extreme learning machine," *under review, IEEE Trans. Instrum. Meas.*, vol. 73, pp. 1–12, Oct. 2023.

Chapter 2

[1] S. Jiang, "On reliable data transfer in underwater acoustic networks: A survey from networking perspective," *IEEE Commun. Surveys Tuts.*, vol. 20, no. 2, pp. 1036–1055, Jan. 2018.

[2] C. Gussen, M. Campos, W. A. Martins, F. M. Costa, and J. N. Gois, "A survey of underwater wireless communication technologies," *J. Commun. Inf. Sys*, vol. 31, no. 1, pp. 242–255, Oct. 2016.

[3] A. Gkikopouli, G. Nikolakopoulos, and S. Manesis, "A survey on underwater wireless sensor networks and applications," in *Proc. Mediterranean Conference on Control Automation, Barcelona, Spain*, 2012, pp. 1147–1154.

[4] Y. Li, Y. Zhang, H. Zhou, and T. Jiang, "To relay or not to relay: Open distance and optimal deployment for linear underwater acoustic networks," *IEEE Trans. Commun.*, vol. 66, no. 9, pp. 3797–3808, Sep. 2018.

[5] A. Yadav and O. A. Dobre, "All technologies work together for good: A glance at future mobile networks," *IEEE Trans. Wireless Commun.*, vol. 25, no. 4, pp. 10–16, Aug. 2018.

[6] S. M. R. Islam, N. Avazov, O. A. Dobre, and K. Kwak, "Power-domain non-orthogonal multiple access (NOMA) in 5G systems: Potentials and challenges," *IEEE Commun. Surveys Tuts.*, vol. 19, no. 2, pp. 721–742, Oct. 2017.

[7] M. Duarte, C. Dick, and A. Sabharwal, "Experiment-driven characterization of full-duplex wireless systems," *IEEE Trans. Wireless Commun.*, vol. 11, no. 12, pp. 4296–4307, Dec. 2012.

[8] M. F. Kader, S. Y. Shin, and V. C. Leung, "Full-duplex non-orthogonal multiple access in cooperative relay sharing for 5G systems," *IEEE Transactions on Vehicular Technology*, vol. 67, no. 7, pp. 5831–5840, Jul. 2018.

[9] F. Qu, H. Yang, G. Yu, and L. Yang, "In-band full-duplex communications for underwater acoustic networks," *IEEE Netw.*, vol. 31, no. 5, pp. 59–65, Sept. 2017.

[10] J. Cheon and H. Cho, "Power allocation scheme for non-orthogonal multiple access in underwater acoustic communications," *Sensors*, vol. 17, no. 11, p. 2465, Oct. 2017.

[11] N. Shende, O. Gurbuz, and E. Erkip, "Half-duplex or full-duplex relaying: A capacity analysis under self-interference," in *Proc. Annual Conference on Information Sciences and Systems, Baltimore, MD, USA*, 2013, pp. 1–6.

[12] P. Qarabaqi and M. Stojanovic, "Statistical characterization and computationally efficient modeling of a class of underwater acoustic communication channels," *IEEE J. Ocean. Eng.*, vol. 38, no. 4, pp. 701–717, Oct. 2013.

[13] R. F. Coates, *Underwater Acoustic System*. MacMillan International Higher Education, 1990, ch. 6, pp. 90–100.

[14] A. Yadav, O. A. Dobre, and N. Ansari, "Energy and traffic aware full-duplex communications for 5G systems," *IEEE Access*, vol. 5, pp. 11 278–11 290, Jul. 2017.

[15] C. Canuto and A. Tabacco, *Taylor Expansions and Application*. Milano: Springer Milan, 2008, ch. 7, pp. 223–255.

[16] Evologics, "Underwater acoustic communication system s2cr 7/17d product information," Sep. 2016. [Online]. Available: https://goo.gl/2SW6Qn

[17] ——, "Usbl positioning and communication system s2cr 7/17 usbl product information," Jun. 2012. [Online]. Available: https://goo.gl/SMLFGE

[18] M. Stojanovic, "On the relationship between capacity and distance in an underwater acoustic communication channel," *ACM SIGMOBILE Mobile Computing and Communications Review*, vol. 11, no. 4, pp. 34–43, Oct. 2007.

[19] M. Grant and S. Boyd, "CVX: Matlab software for disciplined convex programming, version 2.1," http://cvxr.com/cvx, mar 2014.

[20] ——, "Graph implementations for nonsmooth convex programs," in *Recent Advances in Learning and Control, ser. Lecture Notes in Control and Information Sciences*, V. Blondel, S. Boyd, and H. Kimura, Eds. Springer-Verlag Limited, 2008, pp. 95–110.

Chapter 3

[1] S. Jiang, "On reliable data transfer in underwater acoustic networks: A survey from networking perspective," *IEEE Commun. Surveys Tuts.*, vol. 20, no. 2, pp. 1036–1055, Jan. 2018.

[2] C. M. Gussen et al., "A survey of underwater wireless communication technologies," *J. Commun. Inf. Sys*, vol. 31, no. 1, pp. 242–255, Oct. 2016.

[3] A. Gkikopouli, G. Nikolakopoulos, and S. Manesis, "A survey on underwater wireless sensor networks and applications," in *Proc. Mediterranean Conference on Control Automation, Barcelona, Spain*, 2012, pp. 1147–1154.

[4] E. Felemban, F. K. Shaikh, U. M. Qureshi, A. A. Sheikh, and S. B. Qaisar, "Underwater sensor network applications: A comprehensive survey," *Int. J. of Distr. Sensor Netw.*, vol. 11, no. 11, pp. 1–14, Nov. 2015.

[5] D. C. Nguyen, M. Ding, P. N. Pathirana, A. Seneviratne, J. Li, D. Niyato, O. A. Dobre, and H. V. Poor, "6G internet of things: A comprehensive survey," *IEEE Internet Things J.*, pp. 1–1, Aug. 2021.

[6] Y. Wang, W. Feng, J. Wang, and T. Q. S. Quek, "Hybrid satellite-UAV-terrestrial networks for 6G ubiquitous coverage: A maritime communications perspective," *IEEE J. Sel. Areas Commun.*, vol. 39, no. 11, pp. 3475–3490, Jun. 2021.

[7] C. D. Alwis, A. Kalla, Q.-V. Pham, P. Kumar, K. Dev, W.-J. Hwang, and M. Liyanage, "Survey on 6G frontiers: Trends, applications, requirements, technologies and future research," *IEEE Open Journal of the Communications Society*, vol. 2, pp. 836–886, Apr. 2021.

[8] M. Jahanbakht, W. Xiang, L. Hanzo, and M. R. Azghadi, "Internet of underwater things and big marine data analytics a comprehensive survey," *IEEE Commun. Surveys Tuts.*, vol. 23, no. 2, pp. 904–956, Jan. 2021.

[9] Y. Li, Y. Zhang, H. Zhou, and T. Jiang, "To relay or not to relay: Open distance and optimal deployment for linear underwater acoustic networks," *IEEE Trans. Commun.*, vol. 66, no. 9, pp. 3797–3808, Sep. 2018.

[10] R. Wang, A. Yadav, E. A. Makled, O. A. Dobre, R. Zhao, and P. K. Varshney, "Optimal power allocation for full-duplex underwater relay networks with energy harvesting: A reinforcement learning approach," *IEEE Commun. Lett.*, vol. 9, no. 2, pp. 223–227, Oct. 2019.

[11] S. M. R. Islam, N. Avazov, O. A. Dobre, and K. Kwak, "Power-domain non-orthogonal multiple access (NOMA) in 5G systems: Potentials and challenges," *IEEE Commun. Surveys Tuts.*, vol. 19, no. 2, pp. 721–742, Oct. 2017.

[12] A. Yadav and O. A. Dobre, "All technologies work together for good: A glance at future mobile networks," *IEEE Trans. Wireless Commun.*, vol. 25, no. 4, pp. 10–16, Aug. 2018.

[13] H. V. Nguyen, V.-D. Nguyen, O. A. Dobre, D. N. Nguyen, E. Dutkiewicz, and O.-S. Shin, "Joint power control and user association for NOMA-based full-duplex systems," *IEEE Trans. Commun.*, vol. 67, no. 11, pp. 8037–8055, Aug. 2019.

[14] Z. Shi, W. Gao, S. Zhang, J. Liu, and N. Kato, "Machine learning-enabled cooperative spectrum sensing for non-orthogonal multiple access," *IEEE Trans. Wireless Commun.*, vol. 19, no. 9, pp. 5692–5702, May 2020.

[15] J. Liu, Z. Shi, S. Zhang, and N. Kato, "Distributed Q-learning aided uplink grant-free NOMA for massive machine-type communications," *IEEE J. Sel. Areas Commun.*, vol. 39, no. 7, pp. 2029–2041, Jul. 2021.

[16] M. Duarte, C. Dick, and A. Sabharwal, "Experiment-driven characterization of full-duplex wireless systems," *IEEE Trans. Wireless Commun.*, vol. 11, no. 12, pp. 4296–4307, Dec. 2012.

[17] N. Shende, O. Gurbuz, and E. Erkip, "Half-duplex or full-duplex relaying: A capacity analysis under self-interference," in *Proc. Annual Conference on Information Sciences and Systems, Baltimore, MD, USA*, 2013, pp. 1–6.

[18] M. F. Kader, S. Y. Shin, and V. C. M. Leung, "Full-duplex non-orthogonal multiple access in cooperative relay sharing for 5G systems," *IEEE Trans. Veh. Technol.*, vol. 67, no. 7, pp. 5831–5840, Jul. 2018.

[19] M. Zeng, N.-P. Nguyen, O. A. Dobre, Z. Ding, and H. V. Poor, "Spectral- and energy-efficient resource allocation for multi-carrier uplink NOMA systems," *IEEE Trans. Veh. Technol.*, vol. 68, no. 9, pp. 9293–9296, Jul. 2019.

[20] J. Cheon and H. Cho, "Power allocation scheme for non-orthogonal multiple access in underwater acoustic communications," *Sensors*, vol. 17, no. 11, p. 2465, Oct. 2017.

[21] F. Qu, H. Yang, G. Yu, and L. Yang, "In-band full-duplex communications for underwater acoustic networks," *IEEE Netw.*, vol. 31, no. 5, pp. 59–65, Sept. 2017.

[22] E. A. Makled, A. Yadav, O. A. Dobre, and R. D. Haynes, "Hierarchical full-duplex underwater acoustic network: A NOMA approach," in *Proc. IEEE OCEANS, Charleston, SC, USA*, 2018, pp. 1–6.

[23] A. Yener and S. Ulukus, "Wireless physical-layer security: Lessons learned from information theory," *Proc. IEEE*, vol. 103, no. 10, pp. 1814–1825, Sept. 2015.

[24] F. Jameel, W. U. Khan, Z. Chang, T. Ristaniemi, and J. Liu, "Secrecy analysis and learning-based optimization of cooperative NOMA SWIPT systems," in *Proc. IEEE International Conference on Communications Workshops, Shanghai, China*, 2019, pp. 1–6.

[25] A. Mukherjee, S. A. A. Fakoorian, J. Huang, and A. L. Swindlehurst, "Principles of physical layer security in multiuser wireless networks: A survey," IEEE Commun. Surveys Tuts., vol. 16,

no. 3, pp. 1550–1573, Feb. 2014.

[26] P. Qarabaqi and M. Stojanovic, "Statistical characterization and computationally efficient modeling of a class of underwater acoustic communication channels," IEEE J. Ocean. Eng., vol. 38, no. 4, pp. 701–717, Oct. 2013.

[27] M. Stojanovic, "On the relationship between capacity and distance in an underwater acoustic communication channel," ACM SIGMOBILE Mobile Computing and Communications Review, vol. 11, no. 4, pp. 34–43, Oct. 2007.

[28] R. Wang, E. A. Makled, A. Yadav, O. A. Dobre, and R. Zhao, "Reinforcement learning-based energy-efficient power allocation for underwater full-duplex relay network with energy harvesting," in Proc. IEEE Veh. Technol. Conference, Victoria, BC, Canada, 2020, pp. 1–5.

[29] R. F. Coates, Underwater Acoustic System. MacMillan International Higher Education, 1990, ch. 6, pp. 90–100.

[30] A. Yadav, O. A. Dobre, and N. Ansari, "Energy and traffic aware full-duplex communications for 5G systems," IEEE Access, vol. 5, pp. 11 278–11 290, Jul. 2017.

[31] C. Canuto and A. Tabacco, Taylor Expansions and Application. Milano: Springer Milan, 2008, ch. 7, pp. 223–255.

[32] N. Zaghdoud, A. B. Mnaouer, W. H. Alouane, H. Boujemaa, and F. Touati, "Secure performance analysis for full-duplex cooperative NOMA system in the presence of multiple eavesdroppers," in Proc. International Wireless Communications and Mobile Computing, Limassol, Cyprus, 2020, pp. 1719–1725.

[33] Y. Zhang, H.-M.Wang, Q. Yang, and Z. Ding, "Secrecy sum rate maximization in non-orthogonal multiple access," IEEE Commun. Lett., vol. 20, no. 5, pp. 930–933, Mar. 2016.

[34] Evologics. (2012, Jun.) Usbl positioning and communication system s2cr 7/17 usbl product information. Evologics. [Online]. Available: https://goo.gl/SMLFGE

[35] ——. (2016, Sep.) Underwater acoustic communication system s2cr 7/17d product information. datasheet. [Online]. Available: https://goo.gl/2SW6Qn

[36] M. Grant and S. Boyd, "CVX: Matlab software for disciplined convex programming, version 2.1," http://cvxr.com/cvx, mar 2014.

[37] ——, "Graph implementations for nonsmooth convex programs," in Recent Advances in Learning and Control, ser. Lecture Notes in Control and Information Sciences, V. Blondel, S. Boyd, and H. Kimura, Eds. Springer-Verlag Limited, 2008, pp. 95–110.

[38] R. Yao, L. Yao, X. Zuo, N. Qi, Y. Liu, and J. Xu, "Secrecy energy efficiency maximization in a NOMA system," in *Proc. International Conference on Communication Software and Networks*, Chongqing, China, 2019, pp. 106–110.

[39] L. White and J. Hanson, "An automatic sea state calculator," in *Proc. IEEE Oceans*, vol. 3, Providence, RI, USA, 2000, pp. 1727–1734.

Chapter 4

[1] Y. A. Eldemerdash, O. A. Dobre, O. Üreten, and T. Yensen, "Identification of cellular networks for intelligent radio measurements," *IEEE Trans. Instrum. Meas.*, vol. 66, no. 8, pp. 2204–2211, Aug. 2017.

[2] L. De Vito, D. D. Napolitano, S. Rapuano, and M. Villanacci, "Eigenvalue-based signal detector for an automatic modulation classifier," in *Proc. IEEE Int. Instrum. Meas. Technol. Conf. (I2MTC)*, 2010, pp. 1131–1136.

[3] Y. A. Eldemerdash, O. A. Dobre, O. Üreten, and T. Yensen, "Fast and robust identification of GSM and LTE signals," in *Proc. IEEE Int. Instrum. Meas. Technol. Conf. (I2MTC)*, 2017, pp. 1–6.

[4] E. Karami, O. A. Dobre, and N. Adnani, "Identification of GSM and LTE signals using their second-order cyclostationarity," in *Proc. IEEE Int. Instrum. Meas. Technol. Conf. (I2MTC)*, 2015, pp. 1108–1112.

[5] D. Bao, P. Daponte, L. De Vito, and S. Rapuano, "Classification of future aeronautical communication signals," in *Proc. IEEE MetroAeroSpace*, 2014, pp. 570–575.

[6] O. A. Dobre, "Signal identification for emerging intelligent radios: classical problems and new challenges," *IEEE Instrum. Meas. Mag.*, vol. 18, no. 2, pp. 11–18, Apr. 2015.

[7] F. Hameed, O. A. Dobre, and D. C. Popescu, "On the likelihood-based approach to modulation classification," *IEEE Trans. Wireless Commun.*, vol. 8, no. 12, pp. 5884–5892, Dec. 2009.

[8] L. D. Vito, "A review of wideband spectrum sensing methods for cognitive radios," in *Proc. IEEE Int. Instrum. Meas. Technol. Conf.*, 2012, pp. 2257–2262.

[9] L. Angrisani, D. Capriglione, G. Cerro, L. Ferrigno, and G. Miele, "Analysis of different wavelet segmentation methods for frequency-domain energy detection based spectrum sensing," in *Proc.*

IEEE Int. Instrum. Meas. Technol. Conf. (I2MTC), 2017, pp. 1–6.

[10] D. Bao, L. De Vito, and S. Rapuano, "A histogram-based segmentation method for wideband spectrum sensing in cognitive radios," *IEEE Trans. Instrum. Meas.*, vol. 62, no. 7, pp. 1900–1908, July 2013.

[11] F. Patenaud and M. Dufour, "Method and apparatus for noise floor estimation," *U.S. Patent 7,340,375*, Mar. 4, 2008.

[12] A. A. Al-Habob, E. A. Makled, O. A. Dobre, and O. Ü reten, "Blind signal detection in cellular bands," *IEEE Trans. Instrum. Meas.*, vol. 69, no. 3, pp. 657–659, Jan. 2020.

[13] M. J. Ready, M. L. Downey, and L. J. Corbalis, "Automatic noise floor spectrum estimation in the presence of signals," in *Proc. IEEE Asilomar*, vol. 1, 1997, pp. 877–881.

[14] L. Gonzales-Fuentes, K. Barb´e, W. Van Moer, and N. Bj¨orsell, "Cognitive radios: Discriminant analysis for automatic signal detection in measured power spectra," *IEEE Trans. Instrum. Meas.*, vol. 62, no. 12, pp. 3351–3360, Dec. 2013.

[15] H. Xia, K. Alshathri, V. B. Lawrence, Y.-D. Yao, A. Montalvo, M. Rauchwerk, and R. Cupo, "Cellular signal identification using convolutional neural networks: AWGN and Rayleigh fading channels," in *Proc. IEEE Int. Symposium on Dynamic Spectrum Access Networks*, 2019, pp. 1–5.

[16] ROHDE & SCHWARTZ, "R&S® ROMES4 drive test software," Apr. 2021.

[17] T. Ojanpera and R. Prasad, "An overview of air interface multiple access for IMT-2000/UMTS," *IEEE Commun. Mag.*, vol. 36, no. 9, pp. 82–86, April 1998.

[18] "The LTE standard," Signals Research Group-Project commissioned by Ericsson and Qualcomm, Tech. Rep., Apr. 2014. [Online]. Available: https://www.qualcomm.com/media/documents/files/the-lte-standard.pdf

[19] M. Rahnema, "Overview of the GSM system and protocol architecture," *IEEE Commun. Mag.*, vol. 31, no. 4, pp. 92–100, Apr. 1993.

Chapter 5

[1] Y. A. Eldemerdash, O. A. Dobre, O. Ü reten, and T. Yensen, "Identification of cellular networks for intelligent radio measurements," *IEEE Trans. Instrum. Meas.*, vol. 66, no. 8, pp. 2204–2211, Aug. 2017.

[2] ——, "Fast and robust identification of GSM and LTE signals," in *Proc. IEEE Int. Instrum. Meas. Technol. Conf.*, 2017, pp. 1–6.

[3] F. Hameed, O. A. Dobre, and D. C. Popescu, "On the likelihood-based approach to modulation classification," *IEEE Trans. Wireless Commun.*, vol. 8, no. 12, pp. 5884–5892, Dec. 2009.

[4] E. Karami, O. A. Dobre, and N. Adnani, "Identification of GSM and LTE signals using their second-order cyclostationarity," in *Proc. IEEE Int. Instrum. Meas. Technol. Conf.*, 2015, pp. 1108– 1112.

[5] O. A. Dobre, "Signal identification for emerging intelligent radios: classical problems and new challenges," *IEEE Instrum. Meas. Mag.*, vol. 18, no. 2, pp. 11–18, Apr. 2015.

[6] E. A. Makled, A. A. Al-Habob, O. A. Dobre, and O. Ü reten, "Detection and identification of mobile network signals," *IEEE Trans. Instrum. Meas.*, vol. 70, pp. 1–4, Sep. 2021.

[7] D. Grimaldi, S. Rapuano, and L. De Vito, "An automatic digital modulation classifier for measurement on telecommunication networks," *IEEE Trans. Instrum. Meas.*, vol. 56, no. 5, pp. 1711– 1720, Oct. 2007.

[8] H. Agirman-Tosun, Y. Liu, A. Haimovich, O. Simeone, W. Su, J. Dabin, and E. Kanterakis, "Modulation classification of MIMO-OFDM signals by independent component analysis and support vector machines," in *Proc. Conf. Record of the Forty Fifth Asilomar Conf. on Signals, Systems and Computers*, 2011, pp. 1903–1907.

[9] F. Xing, D. Xu, W. Xu, and H. Wang, "A modulation recognition algorithm of communication signals and implementation based on digital signal processor," in *Proc. IEEE MTT-S Int. Wireless Symp.*, 2021, pp. 1–3.

[10] M. D. Wong, S. K. Ting, and A. K. Nandi, "Naive Bayes classification of adaptive broadband wireless modulation schemes with higher order cumulants," in *Proc. 2nd Int. Conf. on Signal Process. and Commun. Syst.*, 2008, pp. 1–5.

[11] X. Li, F. Dong, S. Zhang, and W. Guo, "A survey on deep learning techniques in wireless signal recognition," *Wireless Communications and Mobile Computing*, vol. 2019, pp. 1–12, Feb. 2019.

[12] H. X. et. al, "Cellular signal identification using convolutional neural networks: AWGN and Rayleigh fading channels," in *Proc. IEEE Int. Symp. on Dynamic Spectrum Access Networks*, 2019, pp. 1–5.

[13] M. Kulin, T. Kazaz, I. Moerman, and E. De Poorter, "End-to-end learning from spectrum data: A deep learning approach for wireless signal identification in spectrum monitoring applications," *IEEE Access*, vol. 6, pp. 18 484–18 501, Mar. 2018.

[14] K. Ahmad, U. Meier, and H. Kwasnicka, "Fuzzy logic based signal classification with cognitive radios for standard wireless technologies," in *Proc. IEEE Int. Conf. on Cognitive Radio Oriented Wireless Networks and Commun.*, 2010, pp. 1–5.

[15] K. Ahmad, G. Shresta, U. Meier, and H. Kwasnicka, "Neuro-fuzzy signal classifier (NFSC) for standard wireless technologies," in *Proc. IEEE Int. Symp. on Wireless Commun. Syst.*, 2010, pp. 616–620.

[16] M. Schmidt, D. Block, and U. Meier, "Wireless interference identification with convolutional neural networks," in *Proc. IEEE Conf. on Industrial Informatics*, 2017, pp. 180–185.

[17] K. Alshathri, H. Xia, V. Lawrence, and Y.-D. Yao, "Cellular system identification using deep learning: GSM, UMTS and LTE," in *Proc. 28th Wireless and Optical Commun. Conf.*, 2019, pp. 1–4.

[18] Rohde & Schwartz, "R&S® ROMES4 drive test software," Apr. 2021.

Chapter 6

[1] Y. A. Eldemerdash, O. A. Dobre, O. Ü reten, and T. Yensen, "Identification of cellular networks for intelligent radio measurements," *IEEE Trans. Instrum. Meas.*, vol. 66, no. 8, pp. 2204–2211, Aug. 2017.

[2] —, "Fast and robust identification of GSM and LTE signals," in *Proc. IEEE Int. Instrum. Meas. Technol. Conf. (I2MTC)*, 2017, pp. 1–6.

[3] E. Karami, O. A. Dobre, and N. Adnani, "Identification of GSM and LTE signals using their second-order cyclostationarity," in *Proc. IEEE Int. Instrum. Meas. Technol. Conf. (I2MTC)*, 2015, pp. 1108–1112.

[4] O. A. Dobre, "Signal identification for emerging intelligent radios: classical problems and new challenges," *IEEE Instrum. Meas. Mag.*, vol. 18, no. 2, pp. 11–18, Apr. 2015.

[5] E. A. Makled, A. A. Al-Habob, O. A. Dobre, and O. Ü reten, "Detection and identification of mobile network signals," *IEEE Trans. Instrum. Meas.*, vol. 70, pp. 1–4, Sep. 2021.

[6] F. Hameed, O. A. Dobre, and D. C. Popescu, "On the likelihood-based approach to modulation classification," *IEEE Trans. Wireless Commun.*, vol. 8, no. 12, pp. 5884–5892, Dec. 2009.

[7] E. E. Azzouz and A. K. Nandi, "Modulation recognition using artificial neural networks," in *Automatic Modulation Recognition of Communication Signals*. Springer, 1996, pp. 132–176.

[8] M. D. Wong and A. K. Nandi, "Automatic digital modulation recognition using spectral and statistical features with multi-layer perceptrons," in *Proc. 6th Int. Symposium on Signal Processing and its Applications*, 2001, pp. 390–393.

[9] A. K. Nandi and E. E. Azzouz, "Algorithms for automatic modulation recognition of communication signals," *IEEE Trans. Commun.*, vol. 46, no. 4, pp. 431–436, Apr. 1998.

[10] H. Agirman-Tosun, Y. Liu, A. Haimovich, O. Simeone, W. Su, J. Dabin, and E. Kanterakis, "Modulation classification of mimo-ofdm signals by independent component analysis and support vector machines," in *Proc. Conf. Record of the 45th Asilomar Conf. on Signals, Systems and Computers (ASILOMAR)*, 2011, pp. 1903–1907.

[11] J. Lv, L. Zhang, and X. Teng, "A modulation classification based on svm," in *Proc. IEEE 15th Int. Conf. on Optical Communs. and Networks (ICOCN)*, 2016, pp. 1–3.

[12] C.-S. Park, J.-H. Choi, S.-P. Nah, W. Jang, and D. Y. Kim, "Automatic modulation recognition of digital signals using wavelet features and svm," in *Proc. 10th Int. Conf. on Advanced Commun. Technology*, 2008, pp. 387–390.

[13] X. Gong, L. Bian, and Q. Zhu, "Collaborative modulation recognition based on SVM," in *Proc. 6th Int. Conf. on Natural Computation*, 2010, pp. 871–874.

[14] A. Nandi and E. Azzouz, "Algorithms for automatic modulation recognition of communication signals," *IEEE Trans. Commun.*, vol. 46, no. 4, pp. 431–436, Apr. 1998.

[15] M. D. Wong, S. K. Ting, and A. K. Nandi, "Naive bayes classification of adaptive broadband wireless modulation schemes with higher order cumulants," in *Proc. 2nd Int. Conf. on Signal Process. and Commun. Syst.*, 2008, pp. 1–5.

[16] X. Li, F. Dong, S. Zhang, and W. Guo, "A survey on deep learning techniques in wireless signal recognition," *Wireless Communs. and Mobile Computing*, vol. 2019, pp. 1–12, 2019.

[17] H. Xia, K. Alshathri, V. B. Lawrence, Y.-D. Yao, A. Montalvo, M. Rauchwerk, and R. Cupo, "Cellular signal identification using convolutional neural networks: AWGN and rayleigh fading channels," in *Proc. IEEE Int. Symposium on Dynamic Spectrum Access Networks*, 2019, pp. 1–5.

[18] K. Ahmad, U. Meier, and H. Kwasnicka, "Fuzzy logic based signal classification with cognitive radios for standard wireless technologies," in *Proc. IEEE 5th International Conf. on Cognitive Radio Oriented Wireless Networks and Communs.*, 2010, pp. 1–5.

[19] K. Ahmad, G. Shresta, U. Meier, and H. Kwasnicka, "Neuro-fuzzy signal classifier (NFSC) for standard wireless technologies," in *Proc. IEEE 7th International Symposium on Wireless Commun. Systems*, 2010, pp. 616–620.

[20] M. Schmidt, D. Block, and U. Meier, "Wireless interference identification with convolutional neural networks," in *Proc. IEEE 15th International Conf. on Industrial Informatics (INDIN)*, 2017, pp. 180–185.

[21] E. A. Makled, I. Al-Nahhal, O. A. Dobre, and O. Ü reten, "Identification of cellular signal measurements using machine learning," *IEEE Transactions on Instrumentation and Measurement*, vol. 72, pp. 1–4, Jan. 2023.

[22] K. Alshathri, H. Xia, V. Lawrence, and Y.-D. Yao, "Cellular system identification using deep learning: GSM, UMTS and LTE," in *Proc. 28th Wireless and Optical Communs. Conference (WOCC)*, 2019, pp. 1–4.

[23] H. Xia, K. Alshathri, V. B. Lawrence, Y.-D. Yao, A. Montalvo, M. Rauchwerk, and R. Cupo, "Cellular signal identification using convolutional neural networks: AWGN and rayleigh fading channels," in *Proc. IEEE Int. Symposium on Dynamic Spectrum Access Networks*, 2019, pp. 1–5.

[24] M. Mohammadkarimi, M. Mehrabi, M. Ardakani, and Y. Jing, "Deep learning-based sphere decoding," *IEEE Trans. Wireless Commun.*, vol. 18, no. 9, pp. 4368–4378, Jun. 2019.

[25] L. Alzubaidi, J. Zhang, A. J. Humaidi, A. Al-Dujaili, Y. Duan, O. Al-Shamma, J. Santamar´ıa, M. A. Fadhel, M. Al-Amidie, and L. Farhan, "Review of deep learning: Concepts, CNN archi-

tectures, challenges, applications, future directions," *J. Big Data*, vol. 8, no. 1, pp. 1–74, Mar. 2021.

[26] M. M. Najafabadi, F. Villanustre, T. M. Khoshgoftaar, N. Seliya, R. Wald, and E. Muharemagic, "Deep learning applications and challenges in big data analytics," *J. Big Data*, vol. 2, no. 1, pp. 1–21, Feb. 2015.

[27] Z. Li, F. Liu, W. Yang, S. Peng, and J. Zhou, "A survey of convolutional neural networks: Analysis, applications, and prospects," *IEEE Trans. Neural Netw. Learn. Syst.*, vol. 33, no. 12, pp. 1–21, Jun. 2021.

Chapter7

[1] Y. A. Eldemerdash, O. A. Dobre, O. Ureten, and T. Yensen, "Identification of cellular networks for intelligent radio measurements," *IEEE Trans. Instrum. Meas.*, vol. 66, no. 8, pp. 2204–2211, Aug. 2017.

[2] —, "Fast and robust identification of GSM and LTE signals," in *Proc. IEEE Int. Instrum. Meas. Technol. Conf.*, 2017, pp. 1–6.

[3] F. Hameed, O. A. Dobre, and D. C. Popescu, "On the likelihood-based approach to modulation classification," *IEEE Trans. Wireless Commun.*, vol. 8, no. 12, pp. 5884–5892, Dec. 2009.

[4] E. Karami, O. A. Dobre, and N. Adnani, "Identification of GSM and LTE signals using their second-order cyclostationarity," in *Proc. IEEE Int. Instrum. Meas. Technol. Conf.*, 2015, pp. 1108–1112.

[5] O. A. Dobre, "Signal identification for emerging intelligent radios: classical problems and new challenges," *IEEE Instrum. Meas. Mag.*, vol. 18, no. 2, pp. 11–18, Apr. 2015.

[6] E. A. Makled, A. A. Al-Habob, O. A. Dobre, and O. Ureten, "Detection and identification of mobile network signals," *IEEE Trans. Instrum. Meas.*, vol. 70, pp. 1–4, Sept. 2021.

[7] D. Grimaldi, S. Rapuano, and L. De Vito, "An automatic digital modulation classifier for measurement on telecommunication networks," *IEEE Trans. Instrum. Meas.*, vol. 56, no. 5, pp. 1711–1720, Oct 2007.

[8] H. Agirman-Tosun, Y. Liu, A. Haimovich, O. Simeone, W. Su, J. Dabin, and E. Kanterakis, "Modulation classification of MIMO-OFDM signals by independent component analysis and support vector machines," in *Proc. Conf. Record of the Forty Fifth Asilomar Conf. on Signals, Systems and Computers*, 2011, pp. 1903–1907.

[9] F. Xing, D. Xu, W. Xu, and H. Wang, "A modulation recognition algorithm of communication signals and implementation based on digital signal processor," in *Proc. IEEE MTT-S Int. Wireless Symposium*, 2021, pp. 1–3.

[10] M. D. Wong, S. K. Ting, and A. K. Nandi, "Naive Bayes classification of adaptive broadband wireless modulation schemes with higher order cumulants," in *Proc. 2nd Int. Conf. on Signal Process. and Commun. Syst.*, 2008, pp. 1–5.

[11] X. Li, F. Dong, S. Zhang, and W. Guo, "A survey on deep learning techniques in wireless signal recognition," *Wireless Communications and Mobile Computing*, vol. 2019, pp. 1–12, Feb. 2019.

[12] H. Xia, K. Alshathri, V. B. Lawrence, Y.-D. Yao, A. Montalvo, M. Rauchwerk, and R. Cupo, "Cellular signal identification using convolutional neural networks: AWGN and Rayleigh fading channels," in *Proc. IEEE Int. Symposium on Dynamic Spectrum Access Networks*, 2019, pp. 1–5.

[13] M. D. Wong and A. K. Nandi, "Automatic digital modulation recognition using spectral and statistical features with multi-layer perceptrons," in *Proc. Sixth Int. Symposium on Signal Processing and its Applications*, vol. 2, 2001, pp. 390–393.

[14] A. K. Nandi and E. E. Azzouz, "Algorithms for automatic modulation recognition of communication signals," *IEEE Trans. Commun.*, vol. 46, no. 4, pp. 431–436, Apr. 1998.

[15] E. A. Makled, I. Al-Nahhal, O. A. Dobre, and O. Ureten, "Identification of cellular signal measurements using machine learning," *IEEE Trans. Instrum. Meas.*, vol. 72, pp. 1–4, Jan. 2023.

[16] E. A. Makled, I. Al-Nahhal, O. A. Dobre, O. Ureten, and H. Shin, "Identification of cellular measurements: A neural network approach," *IEEE Trans. Instrum. Meas.*, vol. 73, pp. 1–12, Oct. 2023.

[17] U. Markowska-Kaczmar and M. Kosturek, "Extreme learning machine versus classical feedforward network," *Neural Computing and Applications*, vol. 33, no. 22, pp. 15,121–15,144, Aug. 2021.

[18] Y.-H. Pao, S. M. Phillips, and D. J. Sobajic, "Neural-net computing and the intelligent control of systems," *International Journal of Control*, vol. 56, no. 2, pp. 263–289, Mar. 1992.

[19] Y.-H. Pao, G.-H. Park, and D. J. Sobajic, "Learning and generalization characteristics of the random vector functional-link net," *Neurocomputing*, vol. 6, no. 2, pp. 163–180, Apr. 1994.

[20] M. Ganaie, M. Tanveer, and P. N. Suganthan, "Minimum variance embedded random vector functional link network," in *Proc. International Conference on Neural Information Processing*, Springer, Nov. 2020, pp. 412–419.

[21] L. Zhang and P. N. Suganthan, "A comprehensive evaluation of random vector functional link networks," *Information Sciences*, vol. 367, pp. 1094–1105, Nov. 2016.

[22] G.-B. Huang, Q.-Y. Zhu, and C.-K. Siew, "Extreme learning machine: a new learning scheme of feedforward neural networks," in *Proc. IEEE International Joint Conference on Neural Networks (IEEE Cat. No. 04CH37541)*, vol. 2, 2004, pp. 985–990.

[23] W. Cao, X. Wang, Z. Ming, and J. Gao, "A review on neural networks with random weights," *Neurocomputing*, vol. 275, pp. 278–287, Jan. 2018.

[24] G.-B. Huang, Q.-Y. Zhu, and C.-K. Siew, "Extreme learning machine: theory and applications," *Neurocomputing*, vol. 70, no. 1-3, pp. 489–501, Dec. 2006.

[25] Rohde & Schwarz, "R&S® ROMES4 drive test software," Apr. 2021.

[26] G.-B. Huang, H. Zhou, X. Ding, and R. Zhang, "Extreme learning machine for regression and multiclass classification," *IEEE Trans. Syst., Man, Cybern. B, Cybern.*, vol. 42, no. 2, pp. 513–529, Oct. 2011.